

# ESA Support To Science Element (STSE) SMOS+Sea Ice Final Report

EUROPEAN SPACE AGENCY STUDY CONTRACT REPORT  
UNDER ESTEC CONTRACT No. 4000112022/14/I-AM  
TECHNICAL OFFICER: M. DRUSCH (EOP-SME)

Lars Kaleschke and Xiangshan Tian-Kunze  
Institute of Oceanography, University of Hamburg

Georg Heygster and Catalin Patilea  
Institute of Environmental Physics, University of Bremen

Stefan Hendricks and Robert Ricker  
Alfred-Wegener-Institute, Bremerhaven

Rasmus Tonboe  
Danish Meteorological Institute

Marko Mäkynen  
Finnish Meteorological Institute

Laurent Bertino and Jiping Xie  
Nansen Environmental and Remote Sensing Center

---

**Date:** 28 Aug 2017



EUROPEAN SPACE AGENCY CONTRACT REPORT

*The work described in this report was done under ESA contract. Responsibility for the contents resides in the author or organisation that prepared it.*

## ESA STUDY CONTRACT REPORT

ESA Contract No: 4000112022/14/I-AM	SUBJECT: STSE-SMOS + Sea Ice	CONTRACTOR: Univ. Hamburg
ESA CR( )No:	No. of Volumes: 1 This is Volume No: 1	CONTRACTOR'S REFERENCE: Final Report
<p><b>ABSTRACT:</b></p> <p>Sea-ice thickness measurements from satellite are of great importance given the vast area of the Arctic and Antarctic sea-ice cover. ESA's CryoSat altimeter mission measures the sea ice elevation (freeboard) above the sealevel to estimate its thickness. This method works well for thick ice but bears large relative uncertainties for thin sea-ice because of the small freeboard. The spatial coverage of the altimeter measurements is confined along a narrow sub-satellite track and considerable averaging is required to reduce the inherent radar noise. On the other hand, ESA's SMOS radiometer provides a complementary sensitivity for thin ice and complete daily coverage of the marginal ice zone (MIZ) thus enabling a beneficial synergy of both missions. One main objective of the STSE SMOS+ Sea Ice study was therefore to develop a data fusion product from CryoSat and SMOS data. Based on an optimal interpolation (OI) scheme, a weekly Arctic-wide sea-ice thickness data set was generated, which is now termed as the CS2SMOS product. The benefit of the data merging is shown by a comparison with airborne thickness data in the Barents Sea. The synergy reveals a reduced root mean square deviation of about 0.7 m compared to the CryoSat retrieval and therefore demonstrate the great improvement in thin ice regimes. An improved SMOS sea ice thickness product (v3) which was generated from homogeneously reprocessed SMOS L1C brightness temperatures (TB) version v620, has been used for the synergy product. The v3 SMOS data applied new flags introduced with the version v620 to detect large parts of RFI contaminations and reduce data loss compared to previous versions. Potential areas for improvement of the SMOS ice thickness retrieval algorithm and associated parameterizations have been investigated. We could not confirm significant advantages either for a method using a multi-layer radiation model with vertical ice temperature profile or for a method using an effective ice temperature instead of bulk ice temperature. An evaluation of external noise sources (Faraday rotation, ascending/descending node inhomogeneities, galactic noise, sun glint) indicates no need for further TB corrections. A dedicated validation campaign was conducted in the Barents Sea in March 2014. Thickness measurements from the ice strengthened research vessel Lance, a helicopter based on Lance, and the research aircraft Polar 5 operated from Svalbard airport formed an extensive and unique validation data set including measurements with the EMIRAD-2 L-band radiometer. The validation of two different SMOS sea ice thickness products confirm that the overall main pattern of the spatial thickness distribution is well captured. An impact study of assimilating SMOS thin ice thickness data (thinner than 0.4m) into the coupled ocean-sea ice data assimilation system TOPAZ has shown that compared against independent observations of ice thickness from buoys and ice draft from moorings, there are no degradations in the pack ice but some improvements near the ice edge. The study suggests that the SMOS sea ice thickness is a good complementary data set that can be safely included in the TOPAZ system.</p>		
<p>The work described in this report was done under ESA Contract. Responsibility for the contents resides in the author or organisation that prepared it.</p>		
<p>Names of authors:</p> <p>Lars Kaleschke, Xiangshan Tian-Kunze, Stefan Hendricks, Robert Ricker, Georg Heygster, Catalin Patilea, Rasmus Tonboe, Marko Mäkynen, Laurent Bertino, and Jiping Xie</p>		
NAME OF ESA STUDY MANAGER: Matthias Drusch  DIV: DIRECTORATE:	ESA BUDGET HEADING:	

## Revision history

Date	Author	Comments
Nov. 15, 2016	X. Tian-Kunze	initial outline
Dec. 02, 2016	X. Tian-Kunze	added the contributions from DMI, FMI, UB, AWI, and NERSC
Apr. 26, 2017	L. Kaleschke	added executive summary
Jul. 20, 2017	L. Kaleschke	added scientific roadmap
Aug. 28, 2017		reviewed by Matthias Drusch

## Acronyms

**Table .1.:** List of acronyms and abbreviations used in this document

Acronym	Meaning
AMSR2	Advanced Microwave Scanning Radiometer
DMI	Danish Meteorological Institute
ESA	European Space Agency
FMI	Finnish Meteorological Institute
NERSC	Nansen Environmental and Remote Sensing Center
NSIDC	National Snow and Ice Data Center
SMOS	Soil Moisture and Ocean Salinity mission
UB	University of Bremen
UHH	University of Hamburg

## Reference documents

**Table .2.:** List of reference documents

RD.1	D2 - Scientific Analysis Plan
RD.2	D4 - Database User Manual
RD.3	D5 - ATBD UHH
RD.4	D7 - TR1 UHH and TR1 UB
RD.5	D8 - ATBD AWI
RD.6	Kaleschke et al. (2012)
RD.7	Tian-Kunze et al. (2014)
RD.8	Kaleschke et al. (2016)
RD.9	Xie et al. (2016b)
RD.10	Mecklenburg et al. (2016)
RD.11	Ricker et al. (2017b)
RD.12	Ricker et al. (2017a)

## CONTENTS

<b>I. SMOS+Sea Ice Executive Summary</b>	<b>9</b>
<b>II. Refinement of SMOS sea ice thickness retrieval algorithm</b>	
<i>Xiangshan Tian-Kunze, Lars Kaleschke, Rasmus Tonboe, and Marko Mäkynen</i>	13
II.1. Introduction	13
II.2. Improvement of sea ice retrieval algorithm	
<i>Xiangshan Tian-Kunze and Lars Kaleschke, UHH</i>	14
II.2.1. Brightness temperature	15
II.2.1.1. L1C data	15
II.2.1.2. RFI and geophysical noise <i>contribution from Amelie Schmitt, UHH</i>	15
II.2.2. The impact of vertical ice temperature and salinity profiles on the L-band brightness temperature <i>contribution from Nina Maaß, Sophie Rüd, and Louise Tiemann, UHH</i>	17
II.2.3. Ice concentration	25
II.2.3.1. Problem by combining sea ice concentration in the retrieval	25
II.2.3.2. MODIS-derived ice thickness in the Kara Sea <i>Marko Mäkynen, FMI</i>	28
II.2.3.3. Case study in the Kara Sea	31
II.2.3.4. Conclusion	34
II.2.4. Refinement of the look-up table for the correction from plane layer ice thick- ness to mean ice thickness	36
II.2.5. Sea ice thickness uncertainty estimation in Algorithm III	39
II.2.6. Operational processing	39
II.3. The thermal microwave effective temperature of sea ice-temperature and salinity pro- file parameterization schemes <i>Rasmus Tonboe, DMI</i>	42
II.3.1. The temperature profile	42
II.3.2. The salinity profile	42
II.3.3. The effective temperature estimation	45
II.3.3.1. The extinction and emission	45
II.3.3.2. Comparison to detailed simulations	45
II.3.4. Conclusion and Discussion	46
<b>III. Validation Campaign in the Barents Sea, March 2014</b>	
<i>extracted from (Kaleschke et al., 2016)</i>	51
III.1. Introduction	51
III.2. Physical conditions and experimental set-up	51
III.3. Sea ice thickness from electromagnetic induction	53
III.4. Sea ice thickness from airborne laser scanner and L-band radiometer	54

III.5. SMOS ice thickness retrievals . . . . .	57
III.6. Conclusion . . . . .	60
<b>IV. CS2SMOS: A weekly Arctic sea-ice thickness data</b>	
<i>extracted from (Ricker et al., 2017b)</i>	63
IV.1. Introduction . . . . .	63
IV.2. Data . . . . .	67
IV.3. Methods . . . . .	68
IV.3.1. The Background Field . . . . .	70
IV.3.2. Correlation Length Scale Estimation . . . . .	72
IV.3.3. The Optimal Interpolation Algorithm . . . . .	72
IV.4. Evaluation of the CS2SMOS Fusion Product . . . . .	76
IV.4.1. Comparison with individual Products . . . . .	76
IV.4.2. Cross Validation . . . . .	77
IV.4.3. Validation with Airborne EM . . . . .	80
IV.5. Conclusions . . . . .	80
IV.6. Data availability . . . . .	81
<b>V. Assimilation of SMOS data in the TOPAZ system</b>	
<i>extracted from (Xie et al., 2016b)</i>	83
V.1. Introduction . . . . .	83
V.2. Data and Method . . . . .	84
V.3. Results . . . . .	86
V.4. Conclusions . . . . .	93
<b>VI. Geophysical Noise</b>	
<i>Georg Heygster and Catalin Patilea</i>	95
VI.1. Introduction . . . . .	95
VI.2. Faraday Rotation . . . . .	96
VI.2.1. Problem Background . . . . .	96
VI.2.1.1. Ionosphere . . . . .	96
VI.2.1.2. Faraday Rotation . . . . .	96
VI.2.2. Data sources and error estimates . . . . .	97
VI.2.2.1. Total Electron Content / VTEC Data . . . . .	97
VI.2.2.2. Geomagnetic Field/IGRF data . . . . .	99
VI.2.3. Faraday rotation error . . . . .	100
VI.2.4. Brightness Temperature error . . . . .	104
VI.2.5. Sea Ice Thickness error . . . . .	105
VI.3. Ascending/Descending Node Inhomogeneities . . . . .	107
VI.3.1. Problem Background . . . . .	107
VI.3.2. Results . . . . .	109
VI.3.2.1. Cross comparison between timeseries . . . . .	110
VI.3.2.2. Data Analysis . . . . .	110
VI.3.2.3. L1C data version 620 comparison . . . . .	114
VI.3.2.4. Sea Ice Thickness . . . . .	116
VI.3.2.5. Discussion and Conclusions . . . . .	116
VI.3.3. Recommendations . . . . .	118
VI.4. Galactic noise . . . . .	119
VI.4.1. Problem Background . . . . .	119
VI.4.1.1. Sources of radiation . . . . .	119

VI.4.2. Construction of map . . . . .	119
VI.4.3. Locating the extraterrestrial radiation source . . . . .	122
VI.4.4. Results . . . . .	123
VI.4.5. Conclusions . . . . .	125
VI.5. Sun glint . . . . .	127
VI.5.1. Problem background . . . . .	127
VI.5.1.1. Sun Emission . . . . .	127
VI.5.2. Analysis . . . . .	127
VI.5.3. Results . . . . .	128
VI.5.4. Conclusion . . . . .	131
<b>VII. Scientific roadmap</b>	<b>133</b>



## I SMOS+SEA ICE EXECUTIVE SUMMARY

Sea-ice thickness is a key quantity for many applications including climate research, weather forecasting, shipping and offshore. The capability to measure the thickness from satellite is of great importance given the vast area of the Arctic and Antarctic sea-ice cover. ESA's CryoSat altimeter mission allows to measure the sea ice elevation (freeboard) above the sea level and in turn to estimate its thickness. This method works well for thick ice but bears large relative uncertainties for thin sea-ice because of the small freeboard. The spatial coverage of the altimeter measurements is confined along a narrow sub-satellite track and considerable averaging is required to reduce the inherent radar noise. For this reasons CryoSat provides only limited information about the highly dynamic marginal ice zones (MIZ). On the other hand, ESA's SMOS radiometer provides a complementary sensitivity for thin ice and complete daily coverage of the MIZ thus enabling a beneficial synergy of both missions. One main objective of the STSE SMOS+ Sea Ice study was therefore to develop a data fusion product based on CryoSat and SMOS data, now termed the CS2SMOS product. As a prerequisite, SMOS sea ice thickness retrieval methods had to be improved and validated with new field campaign data. Finally, an evaluation of the impact of the new SMOS observations on ocean-ice forecasts was performed. A brief summary of main findings and results is given in the following:

- The improved SMOS sea ice thickness product, specified as version 3, is based on homogeneously reprocessed SMOS L1C brightness temperatures (TB) version v620. The new flags introduced with the version v620 of SMOS L1C TBs detect large parts of RFI contaminations and reduce data loss compared to previous versions. An evaluation of external noise sources (Faraday rotation, ascending/descending node inhomogeneities, galactic noise, sun glint) indicates no need for further TB corrections.
- Potential areas for improvement of the SMOS ice thickness retrieval algorithm and associated parameterizations have been investigated. We could not confirm significant advantages either for a method using a multi-layer radiation model with vertical ice temperature profile or for a method using an effective ice temperature instead of bulk ice temperature. A considerable uncertainty remains with respect to vertical salinity profile parameterizations. An evaluation of the effect of ice concentration on the thickness retrieval revealed only a weak dependency in the MIZ. The statistical correction for the thickness distribution was improved using a polynomial fit instead of a look-up table thereby eliminating discretization artefacts in the resulting thickness histogram.
- A dedicated validation campaign was conducted in the Barents Sea in March 2014. Thickness measurements from the ice strengthened research vessel Lance, a helicopter based on Lance, and the research aircraft Polar 5 operated from Svalbard airport formed an extensive and unique validation data set including measurements with the EMIRAD-2 L-band radiometer. The validation of two different SMOS sea ice thickness products

confirm that the overall main pattern of the spatial thickness distribution is well captured. The thickness of deformed ice was considerably underestimated but the extensive areas of newly grown young sea ice were found in good agreement with the shipborne measurements.

- A merged synergy product of complementary weekly Arctic sea-ice thickness data records from the CryoSat altimeter and SMOS radiometer was developed. Based on an optimal interpolation (OI) scheme a weekly Arctic-wide sea-ice thickness data set was generated. The benefit of the data merging is shown by a comparison with airborne thickness data in the Barents Sea. The synergy reveal a reduced root mean square deviation of about 0.7 m compared to the CryoSat retrieval and therefore demonstrate the great improvement in thin ice regimes.
- The impact of assimilating SMOS thin ice thickness data into the coupled ocean-sea ice data assimilation system TOPAZ was evaluated. TOPAZ is the operational Arctic forecast system which assimilates sea surface temperature (SST), altimetry data, temperature and salinity profiles, ice concentration, and ice drift with the ensemble Kalman filter (EnKF). Two parallel Observing System Experiments have been performed in March and November 2014, in which the SMOS sea ice thickness (thinner than 0.4 m) are assimilated in addition to the standard observational data sets. Validation against independent observations of ice thickness from buoys and ice draft from moorings indicates that there are no degradations in the pack ice but some improvements near the ice edge. The areas of largest impact are the Kara Sea, Canadian Archipelago, Baffin Bay, Beaufort Sea and Greenland Sea. The study suggests that the SMOS sea ice thickness is a good complementary data set that can be safely included in the TOPAZ system.

Major knowledge gaps and recommendations for future work:

- Uncertainty is introduced by the insufficient knowledge about the snow thickness. A new snow radar system aboard the Polar 5 did not perform as expected during the SMOSIce campaign and the data could not be used for the analysis. We recommend further validation campaigns with an improved snow radar in combination with a L-band radiometer to close this gap of knowledge.
- Difficulties in estimating uncertainty are caused by the lack of in-situ validation data, i.e. vertical salinity, temperature and density profiles. A strong limitation for the development and improvement of sea ice radiative transfer and retrieval models stems from the lack of coincident measurements of low-frequency microwave emission and in-situ sea ice profiles. The availability of such validation data is a prerequisite for the better understanding of the emissivity for improved satellite retrieval of sea ice parameters or assimilation of brightness temperatures in ocean-ice forecast models.

List of publications produced within the framework of SMOS + Sea ice project:

- Kaleschke, L., Tian-Kunze, X., Maaß, N., Beitsch, A., Wernecke, A., Miernecki, M., Müller, G., Fock, B., Gierisch, A., Schlünzen, K., and others (2016). SMOS sea ice product: Operational application and validation in the Barents Sea marginal ice zone. *Remote Sensing of Environment*, 180, 264-273.

- Xie, J., Counillon, F., Bertino, L., Tian-Kunze, X., and Kaleschke, L.: Benefits of assimilating thin sea ice thickness from SMOS into the TOPAZ system, *The Cryosphere*, 10, 2745-2761, <https://doi.org/10.5194/tc-10-2745-2016>, 2016.
- Ricker, R., Hendricks, S., Kaleschke, L., Tian-Kunze, X., King, J., and Haas, C.: A weekly Arctic sea-ice thickness data record from merged CryoSat-2 and SMOS satellite data, *The Cryosphere*, 11, 1607-1623, <https://doi.org/10.5194/tc-11-1607-2017>, 2017.
- Ricker, R., S. Hendricks, F. Girard-Ardhuin, L. Kaleschke, C. Lique, X. Tian-Kunze, M. Nicolaus, and T. Krumpfen (2017), Satellite-observed drop of Arctic sea ice growth in winter 2015-2016, *Geophys. Res. Lett.*, 44, 3236-3245, doi:10.1002/2016GL072244.



## II REFINEMENT OF SMOS SEA ICE THICKNESS RETRIEVAL ALGORITHM

*Xiangshan Tian-Kunze, Lars Kaleschke, Rasmus Tonboe, and Marko Mäkynen*

### II.1. Introduction

Thin sea ice thickness has been derived from the brightness temperatures measured at 1.4 GHz (L-band) by the European Space Agency's (ESA) Soil Moisture and Ocean Salinity (SMOS) mission (Kaleschke et al., 2012; Tian-Kunze et al., 2014) at the University of Hamburg (UHH). The retrieval algorithm, which is based on a thermodynamic sea ice model and a one-ice-layer radiative transfer model, takes the variations of sea ice temperature and salinity into account. Moreover, corrections have been done converting homogeneous plane layer ice thickness into heterogeneous layer mean ice thickness using a parameterized lognormal distribution function. The algorithm has been used for the continuous operational production of a SMOS-based sea ice thickness data set from 2010 on (Tian-Kunze et al., 2014).

In the previous project-SMOSIce, various comparisons and validations of SMOS sea ice thickness data have been carried out with MODIS-derived ice thickness in the Kara Sea, helicopter-based EM Measurements in the Laptev Sea, and model outputs from TOPAZ and PIOMAS assimilation systems. Good agreement has been found between SMOS- and MODIS-derived ice thicknesses in the Kara Sea with a correlation coefficient of more than 0.6 for the two winter seasons (2009-2010, 2010-2011). The ice thickness measured by the helicopter EM agreed well with that from SMOS. During the first three months of freeze-up periods, the modelled ice thickness growth from TOPAZ and PIOMAS matched well with that observed by SMOS, whereas during March and April, large discrepancies have been observed between model outputs and SMOS data. The data has been widely used and tested by users from the fields of sea ice modelling, sea ice forecasting, weather forecasting, field observations. Yang et al. (2014) has assimilated the SMOS sea ice thickness data from UHH into a coupled ice-ocean model and found out that the SMOS ice thickness assimilation leads to improved thickness forecasts. However, the current sea ice thickness retrieval algorithm still has large uncertainties and bias regarding to the aspects summarized in the following:

- Vertical ice temperature and salinity profile: Simulations have shown that not only bulk ice temperature and bulk ice salinity have considerable impacts on the brightness temperature (TB), but also the vertical profiles of both parameters could influence the radiation. This effect is not yet considered in the current retrieval.
- Ice concentration: The previous study has also shown that 100 % ice coverage assumption, which is one of the main assumptions made in the operational retrieval, leads to an underestimation of ice thickness if open water is present within the SMOS footprint (Tian-Kunze et al., 2014).
- Ice thickness distribution function: Applying an ice thickness distribution function within a SMOS footprint has brought considerable improvement in the estimation of

mean ice thickness, which is significantly underestimated under the plane ice layer assumption. However, the distribution function is derived from ice thickness data measured mainly in multi-year ice regions, and therefore needs more thoroughful validation.

- **Snow layer:** The thermodynamical and radiational effects of a snow layer on the sea ice brightness temperature has been studied by (Maaß et al., 2013) over thick multi-year ice. Although we included the thermodynamical effect of a snow layer in our sea ice retrieval, the radiational effect is neglected. This can cause uncertainties in the retrieval.
- **Ice type and surface roughness:** Ice type and surface roughness have influences especially on the horizontally polarized brightness temperatures. This effect is investigated in a parallel project. Preliminary findings suggest that the effect of surface roughness can be neglected at nadir view.

In this project we investigate the possibilities and methods to refine the current operational SMOS sea ice thickness retrieval algorithm and try to give a better estimation of retrieval uncertainties.

## II.2. Improvement of sea ice retrieval algorithm

*Xiangshan Tian-Kunze and Lars Kaleschke, UHH*

The various versions of previous and present algorithms are listed in the Table II.1.

**Table II.1.:** Overview of the different versions of SMOS sea ice thickness retrieval algorithms

Algorithm	L3C data	L1C TB	Characteristics
I	v1.0	v346, v505	plane layer ice thickness, semi-empirical method with constant TB tie points for sea water and sea ice as well as a constant attenuation factor (Kaleschke et al., 2012)
II	v2.0	v505	plane layer ice thickness, variable ice temperature and ice salinity
II*	v2.1	v505, v620	operational since October 2014, the same as Algorithm II, but with a correction of ice thickness with a lognormal ice thickness distribution function, a look-up table is created for the correction factor (Tian-Kunze et al., 2014)
III	v3.0, v3.1	v620	operational since October 2016, the same as Algorithm II*, but with improved RFI filtering, parameterized correction function instead of the look-up table for the transformation of plane layer ice thickness to heterogeneous layer ice thickness, extended thickness uncertainty estimation. v3.0 data has been used to create preliminary CS2+SMOS synergy data, however, the uncertainty in this version is overestimated.

## II.2.1. Brightness temperature

### II.2.1.1. L1C data

SMOS measures in the L-band brightness temperatures in full polarization, with incidence angles ranging from  $0^\circ$  to  $65^\circ$ . It has global coverage every three days (Kerr et al., 2001), whereas daily coverage up to  $85^\circ$  latitude can be expected in the polar regions. The spatial resolution varies from about 35 km at nadir view to more than 50 km at higher incidence angles.

Brightness temperatures (TB) used in the Algorithm I, II, II\*, and III are the daily mean intensities averaged over incidence angles from  $0^\circ$  to  $40^\circ$ . The intensity is the average of horizontally and vertically polarized brightness temperatures, equal to  $0.5 (TB_h + TB_v)$ . Over sea ice, the intensity is almost independent of incidence angle. By using the whole incidence angle range of  $0-40^\circ$ , we can get more than 100 brightness temperature measurements per grid point per day for the main part of the Arctic. The radiometric accuracy of single brightness temperature measurement is larger than 3 K. By averaging over numerous measurements we can reduce the brightness temperature uncertainty to about 0.5 K. However, by averaging we partly reduce the geophysical and temporal variability. The daily averaged brightness temperature intensities in the Arctic and Antarctic are interpolated with a nearest-neighbor algorithm and gridded into the “National Snow and Ice Data Center (NSIDC)” polar stereographic projection with a grid resolution of 12.5 km. We call this gridded daily mean brightness temperature as L3B SMOS TB data.

The version number of L1C brightness temperature has changed several times. The version numbers and their periods are listed in the Table II.2. Sea ice thickness (with data version v3.1) retrieved with Algorithm III is based on the v620 L1C data.

**Table II.2.:** Overview of SMOS L1C data

Data version	Mode	Time period	Remarks
v330	Dual	Dec.12 and 13, 2009; Mar. 5 and 7, 2010	
v344	Full	Jul. 19, 2010- Dec. 26, 2011	
v346	Dual, Full	Jan. 12, 2010- May 23, 2011	
v346	Full	May 24, 2010- Oct. 23, 2011	
v503	Full	Oct. 23, 2011- Nov. 2011	
v504	Full	Nov. 2011-Mar.21, 2012	
v505	Dual, Full	Jan. 12, 2010-now	reprocessed for the whole period
v620	Dual, Full	Jan. 12, 2010-now	reprocessed for the whole period

### II.2.1.2. RFI and geophysical noise

*contribution from Amelie Schmitt, UHH*

SMOS measurements are strongly influenced by Radio Frequency Interference (RFI), especially in the first two years after launching SMOS satellite. The detection and mitigation of RFI contaminated measurements is a critical step for the further retrieval of geophysical parameters. In the Algorithm I, II and II\*, we implemented a simple threshold value of 300 K to either vertically or horizontally polarized TB to select out the snapshots with possible RFI contamination. To ensure the quality of the measurements, we discard a complete snapshot if any TB measurement within the snapshot exceed this threshold value. This leads to con-

siderable data loss, especially in the Barents Sea, Laptev Sea, East Siberian Sea, and north of Greenland. RFI flagging (Table II.3 and Table II.4) in the L1C data has been improved distinctly in the new reprocessed 620 version. A thorough analysis has been done within this study to compare the implementation of combined RFI flagging provided in the v620 L1C data with that of simple threshold method used until now (see more details in SMOS + Sea Ice TR1 UHH section 2.1).

**Table II.3.:** RFI flags in the SMOS v620 L1C product.

RFI flags	
TBH/TBX RFI flag	Snapshot is contaminated with RFI in H polarisation
TBV/TBY RFI flag	Snapshot is contaminated with RFI in V polarisation
Point source RFI flag	Pixel is affected by point source RFI
Tail RFI flag	Pixel is affected by the tails of a point source RFI

**Table II.4.:** Other flags in the SMOS v620 L1C product.

Other flags	
Sun point flag	Pixel is located in a zone where a sun alias was reconstructed
Sun tails flag	Pixel is located in the hexagonal alias directions centred on a sun alias
Sun glint area flag	Pixel is located in a zone where sun reflection has been detected
Moon point flag	Pixel is located in a zone where a moon alias was reconstructed
Border field of view flag	Pixel is close to the border delimiting the extended alias free zone or to the unit circle replicas borders

The analysis has shown that the new SMOS flags in v620 detect a large part of data that is contaminated by RFI or by sun or by geometric effects. Especially for point sources, these flags have an advantage over the threshold method, because they only flag the actual source and thus, the rest of the uncontaminated values in the snapshot do not have to be discarded. By using a combination of the SMOS flags for point and tail RFI, and sun point alias with a subsequent application of the old threshold method to remove all remaining values larger than 300 K, we can have more TB measurements to average, which will reduce the uncertainty of daily TB mean. In this new method it is possible that contaminated pixels with values smaller than 300 K might not be detected. This small disadvantage is, however, outweighed by the large number of advantages of the new method. With the new method the overall data loss is reduced, the occurrence of data holes in the Central Arctic is largely prevented (Fig. II.1), and geometric stripes caused by sun aliases are diminished. Therefore, this new flagging method is implemented in the Algorithm III.

15 April 2015

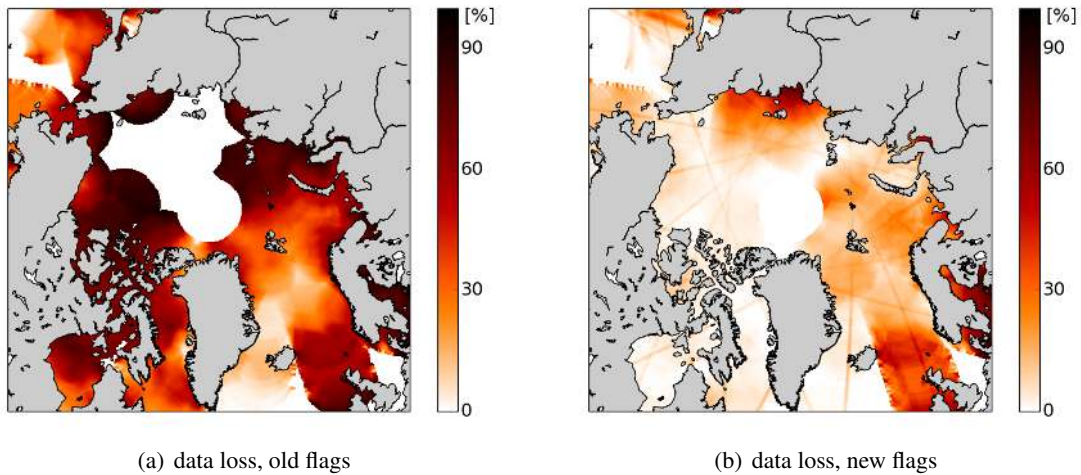


**Figure II.1.:** Data loss on 15 April 2015 using the old UHH flags (left) and the new combined method (right).

## II.2.2. The impact of vertical ice temperature and salinity profiles on the L-band brightness temperature

*contribution from Nina Maaß, Sophie Rüd, and Louise Tiemann, UHH*

Sea ice emissivity depends on the effective surface reflectance as well as the surface and volume scattering. The sea ice permittivity depends on the brine volume of an ice layer, which is a function of sea ice temperature and sea ice salinity (Ulaby et al., 1981). In the current SMOS ice thickness retrieval, we use bulk ice temperature and bulk ice salinity to calculate the ice permittivity, as well as the sea ice emissivity. However, the attenuation constant of ice permittivity does not increase linearly with ice temperature and ice salinity. Therefore, if we consider the vertical ice temperature and salinity profiles within an ice layer, the overall brightness temperature could be much different from that calculated using bulk values.

In this project, we investigate the vertical profiles of ice temperature and ice salinity from measurement data and model simulations. Idealized or averaged profiles are then implemented into a multi-layer radiation model (Maaß, 2013) to simulate brightness temperatures.

Vertical profiles of ice salinity and their impact on the TB have been studied in the framework of a master thesis (Rued (2015)). The following results are part of this master thesis. Figure II.2 shows the salinity and temperature profiles for ice growth simulated with a 1-d thermo-halo-dynamic sea ice model (SAMSIM) (Griewank and Notz, 2014) at (75°N, -180°W) and (80°N, 00°E). The salinity profiles from SAMSIM simulations shown in Rued (2015) vary strongly depending on the locations and growth stages. General increase of brightness temperatures can be expected due to the highly saline boundary layer. The study has also shown that there are still large discrepancies among bulk ice salinities from empirical formulas, in-situ measurements, and SAMSIM simulations. For the sensitivity studies with vertical profiles in the next sections we will use "L-shape" salinity profile for average (Rued, 2015; Griewank and Notz, 2014).

Vertical ice temperature profiles from buoy data have been analyzed in the framework of another master thesis (Tiemann, 2016). In order to determine realistic temperature profiles, we use measurements from 17 Ice Mass Balance (IMB) buoy time series suggested by (Tiemann, 2016). The profiles are slightly different from the linear temperature gradient

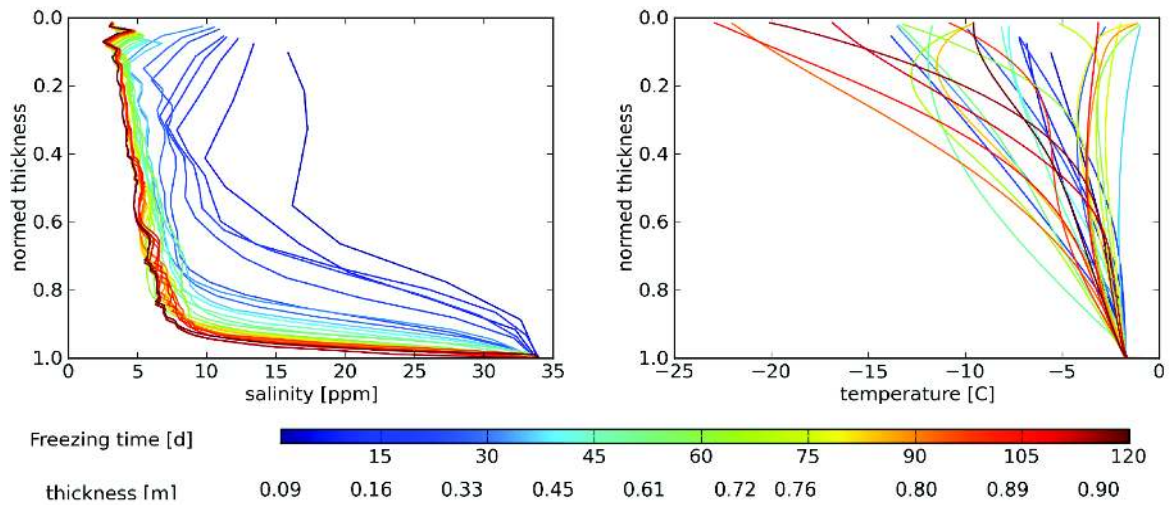


**Figure II.2.:** Salinity (left) and temperature (right) profiles over normed thickness at (75°N, -180°W). The common color coding indicates freezing time and ice thickness, from Rued (2015).

assumption used in (Maaß, 2013). In the following we first compare the simulated TBs using linear ice temperature and L-shape ice salinity profile with that simulated with bulk ice temperature and salinity. At the second step, we compare the TBs simulated using linear temperature profile to that calculated with the averaged vertical ice temperature profile from buoy data, both with a bulk ice salinity. The TB simulations are performed using the Burke model (Maaß, 2013) modified such that it accounts for higher order reflection terms. The model is applied to one snow and ten ice layers, which is a good compromise between continuous profiles and computational effort. For the given temperature profiles, the difference to simulations including much higher numbers of layers within the ice is less than about 0.1K. The ice is covered by one snow layer, which for the following sensitivity analyses has a thickness of 10 % of the ice thickness.

### 1. Using L-shape ice salinity profile and linear temperature profile

Following the suggestion by Rued (2015), we use the average L-shaped salinity profiles given in (Griewank and Notz, 2014), i.e. a salinity distribution in the ice that is characterised by a roughly constant ice salinity or a slowly increasing ice salinity with depth in the upper part of the ice and a steep increase of salinity in the lower part (roughly the lower quarter) of the ice thickness with a continuous salinity transition at the interface between ice and ocean.

For first-year ice though, we introduce a dependence on the ice thickness. We modify the salinity profiles such that their bulk salinities correspond to the empirical relationship between ice thickness and bulk salinity as given in (Cox and Weeks, 1983) (Figure II.3). Figure II.4 shows the impact on TB simulations of such a salinity profile in combination with a linear temperature gradient in the ice as compared to simulations for one ice layer and bulk values for the ice salinity and temperature. Under cold conditions, the TB simulated with salinity and temperature profiles is up to 20 K lower than that with bulk values.

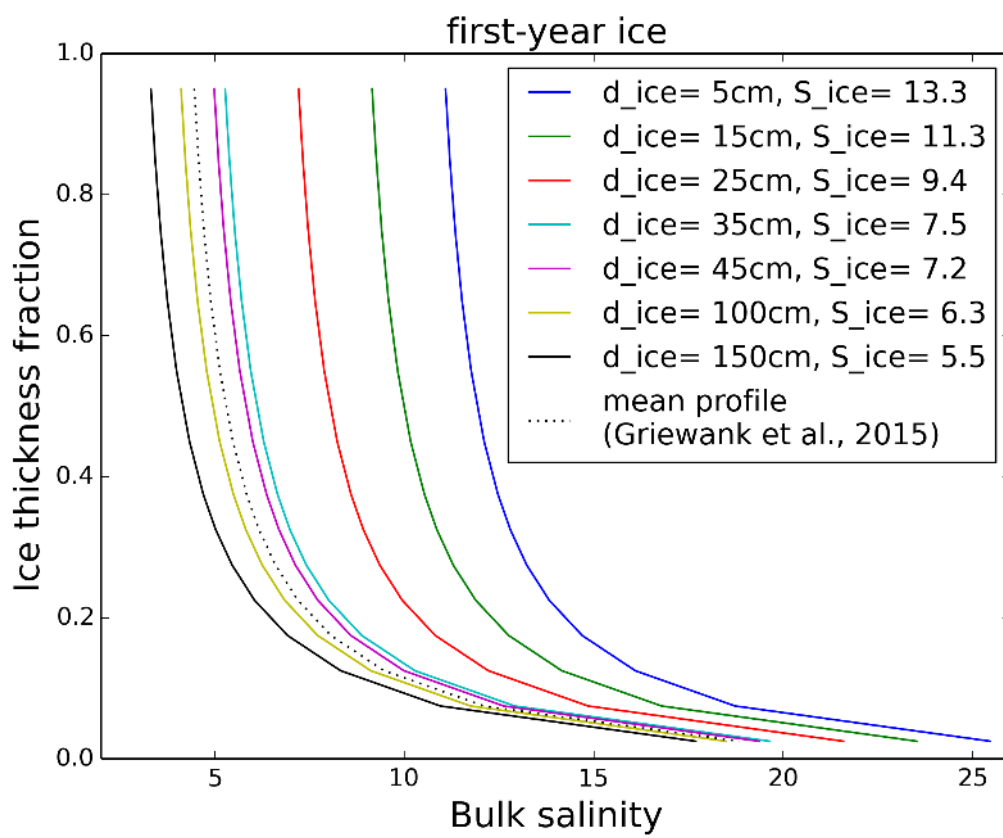


**Figure II.3.:** Suggested salinity profiles for first-year ice TB simulations. The black dotted line shows the mean salinity profile for first-year ice as obtained by (Griewank and Notz, 2014). The solid colored lines show our approximations of the mean profile for different ice thicknesses (given in legend), where the bulk salinity of each profile (given in legend) corresponds to the bulk salinity of the empirical ice thickness-to-bulk-salinity-relationship presented in (Cox and Weeks, 1983). Ice thickness fraction of 1.0 indicates the top of the ice layer, 0.0 indicates the bottom of the ice layer.

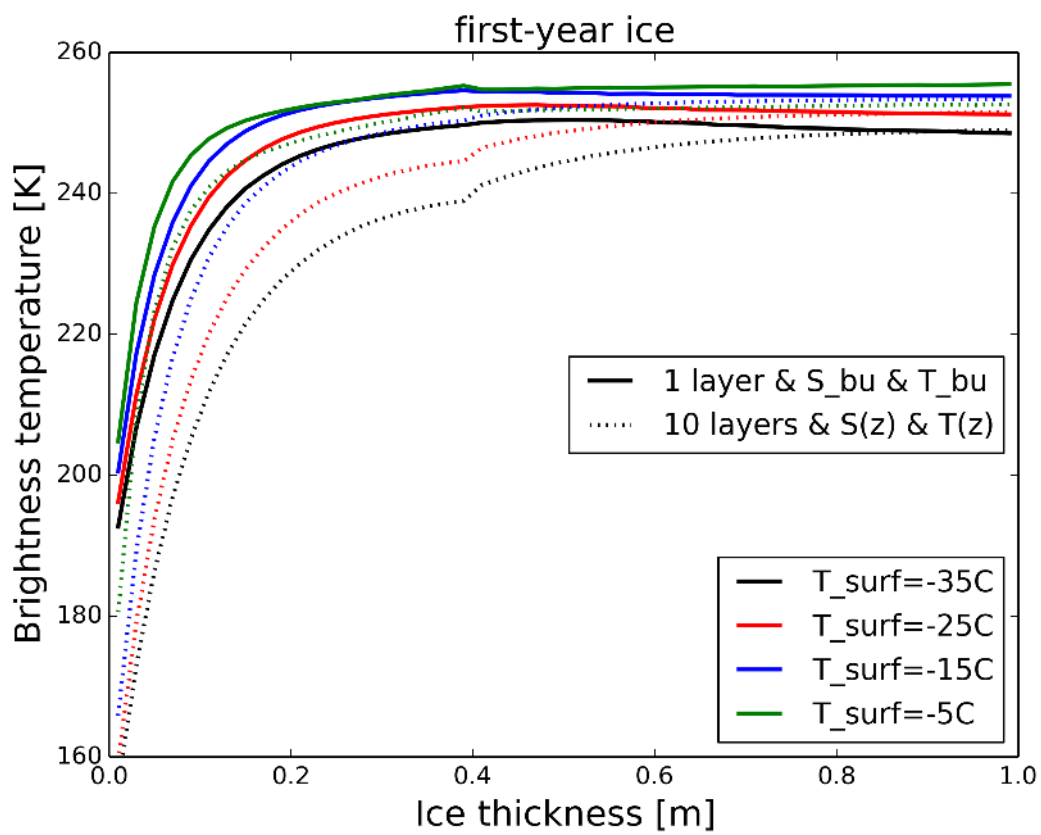


**Figure II.4.:** TB as simulated for first-year ice. Simulations are performed for different ice surface temperatures (different colors; see legend) for one ice layer and a bulk salinity and a bulk temperature (solid lines) and for ten ice layers and a salinity profile as given in Figure II.3 and a linear temperature gradient in the ice (dashed lines).

## 2. Using bulk ice salinity and vertical ice temperature profiles from buoy data

From 17 buoy time series, we select all measurements carried out between October to April to ensure winter/spring conditions. All individual measurements are then divided into three ice thickness classes with the median ice thicknesses 1.1m, 3.1m, and 5.1m. The three classes thus contain 1) ice thicknesses up to 2.1m, 2) ice thicknesses between 2.1 and 4.1m, and 3) ice thicknesses higher than 4.1m, respectively. Within these ice thickness classes, the measurements are then divided into three different ice surface temperature classes ( $T_{surf} = -35^{\circ}\text{C}$ ,  $-20^{\circ}\text{C}$ ,  $-5^{\circ}\text{C}$ ) and these in turn are divided into three different snow thickness classes ( $d_{snow} = 0\text{ cm}$ ,  $20\text{ cm}$ ,  $40\text{ cm}$ ).

From these classified buoy measurements, we determine the average temperature gradient in the snow layer for the different conditions (i.e. ice and snow thickness and ice surface temperature). To obtain continuous results for the snow temperature gradients, we linearly interpolate between the given ice conditions, i.e. for surface temperatures, ice and snow thicknesses in-between the above given median values. Together with the assumption of a linear temperature gradient in the snow, the average gradient obtained from (interpolating) the buoy measurements is used to calculate the mean snow temperature.

To determine ice temperature profiles, we first interpolate the buoy-measured temperature profiles to ten ice layers and then average all profiles found for each of classes defined by ice and snow thickness and ice surface temperature. Again, the resulting average ice temperature profiles are interpolated for all possible ice and snow thickness and ice surface temperature conditions.

Figure II.5 show the temperature profiles as obtained from the buoy measurements for the ice thickness classes 1.1m (as described above). In comparison, temperature profiles are shown that correspond to the so far used calculation of the snow and ice temperature. This approach assumes that the heat conduction at the snow-ice-interface is continuous (MAYKUT, 1978)) and that the temperature gradients in the ice and snow are linear. Using this approach as a reference, the impact of the buoy-based snow and ice temperature profiles on the TB simulations is also indicated. As can be seen from Figure II.5, the buoy-measured temperature profiles are mostly non-linear. Accordingly, there is difference in the simulated TBs between using buoy-based and linear temperature profiles. The TB difference varies from -2 K to 7 K, depending on the given surface temperature and snow thickness. Colder surface temperature results in greater TB difference.

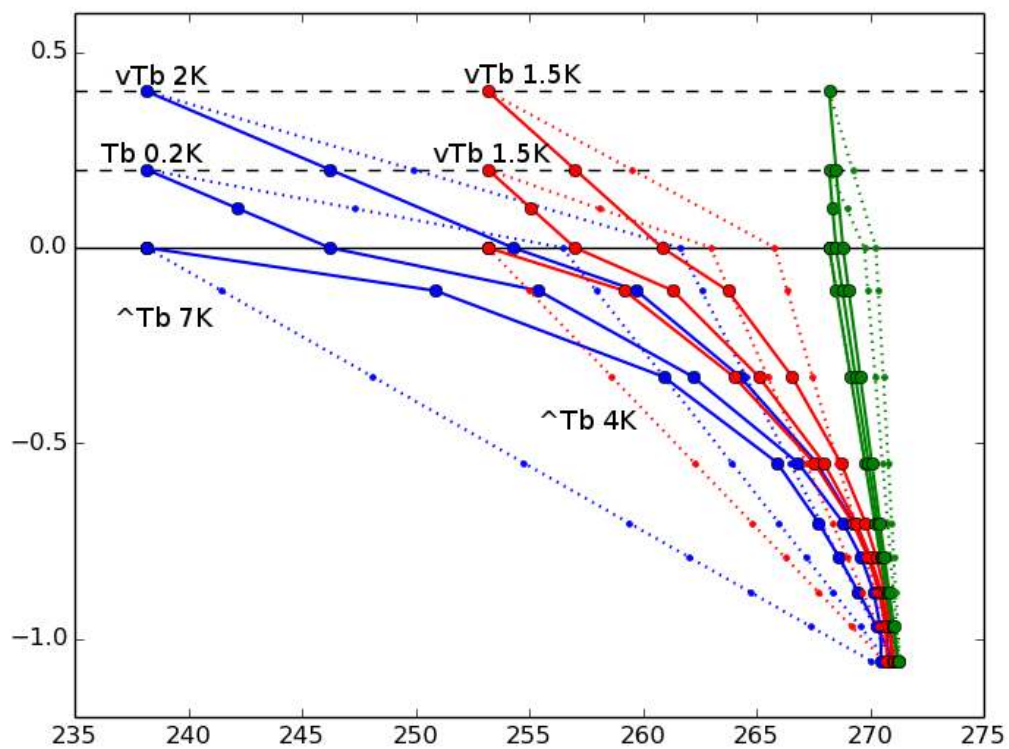


**Figure II.5.:** Ice temperature profiles for the 1.1m ice thickness class as obtained from averaging the IMB buoy measurements (solid line) and as used so far for TB simulations (dotted line; linear temperature gradients and assumption of continuous thermal conduction at snow-ice-interface (MAYKUT, 1978)). The zero line on the y-axis indicates the snow-ice-interface, positive values indicate snow, negative values ice. Profiles are given for different ice surface temperatures:  $-35^{\circ}\text{C}$  (blue),  $-20^{\circ}$  (red),  $-5^{\circ}$  (green) and for three different snow thicknesses (0, 20, and 40cm). Numbers at the profiles give the TB differences resulting if the linear temperature profiles and the buoy-based temperature profiles are used in the simulations. up sign indicates that TB increases for the buoy-based temperature profiles as compared to the linear temperature gradients, down sign indicates a decrease.

Rasmus Tonboe has shown in section 3 that the effective temperature ( $T_{eff}$ ) calculated with a simple linear combination model can be tuned to fit well the reference  $T_{eff}$  calculated with the Microwave Emission Model of Layered Snowpacks (MEMLS) model. The simple linear combination model has the advantage of only using the surface temperature as input. Moreover, it is shown that the dynamic range of the  $T_{eff}$  is about 7K. Following equation is used to describe the  $T_{eff}$ :

$$T_{eff} = a * T_s + (1 - a) * T_{water}, \quad (II.1)$$

where  $a$  has a value of 0.17,  $T_s$  is the snow-ice interface temperature, and  $T_{water}$  is the freezing temperature of sea water, which is  $-2^{\circ}\text{C}$ .  $a$  is tuned in comparison with the reference simulations with MEMLS in the Ross Sea.

In the following, we retrieved sea ice thickness from the brightness temperatures measured by the EMIRAD L-band radiometer during the SMOSIce campaign on March 24, 2014 in the Barents Sea (Kaleschke et al., 2016), using a one-layer (OP) (Kaleschke et al., 2012) radiation model, a multi-layer (10 layers) radiation model (Maaß, 2013) (ML), and using the effective temperature suggested by DMI (RAS). More details about the campaign can be found in the next chapter. The thermodynamic model and the iterative retrieval method are the same as in Algorithm II\* (Tian-Kunze et al., 2014). For all three cases we used the bulk ice salinity, which is determined empirically with the ice thickness. A linearly decreasing ice temperature profile was implemented in the multi-layer radiation model, with the same surface air temperature as boundary condition as for the one-layer model.

Here we only show the results from one flight track. Along this track, the gradient from thin ice to thick ice is obvious. In the beginning 15 min, mostly thin ice was measured. The results show that using effective ice temperature, we retrieve slightly thinner ice than using the bulk ice temperature (Figure II.6). This is because the effective temperature is warmer than the bulk ice temperature for thin ice. With the multi-layer radiation model, we also retrieve thinner ice than that with the one-layer model for the thin ice (Figure II.6). During the campaign, simultaneously to the EMIRAD brightness temperature measurement, sea ice thickness was derived from the surface elevation measured by an airborne laser scanner (ALS). From Figure II.6 we can see that the correlation coefficient between ALS-derived ice thickness and the three different retrievals are very similar. The ALS-derived ice thickness under the assumption of 10% snow on the top of the ice layer is much less than that derived from EMIRAD brightness temperature. However, if we vary the snow thickness (shown as grey area in Figure II.6), ALS-derived ice thickness is almost in the same order with the EMIRAD-derived ice thickness.

The sensitivity study carried out using a multi-layer radiation model with vertical ice temperature and salinity profiles have shown that the distribution of ice temperature and ice salinity within an ice layer have impact on the simulated TBs. The study carried out at DMI and at UHH suggest controversive shapes of salinity profiles. Whereas UHH suggests that an L-form profile (with highest salinity on the bottom) is best suitable as vertical ice salinity profile, the study of DMI suggests (see section 3) an upside-down L-form profile (with highest salinity on the top). We can not justify either of them due to the lack of validation data. More measurement data are needed to correctly parameterize the profiles of ice temperature and ice salinity. From the comparison with independent validation data (ALS-measured ice thickness), we could not identify significant advantage either for the method using multi-layer radiation model with vertical ice temperature profile or for the method using an effective ice temperature instead of bulk ice temperature.

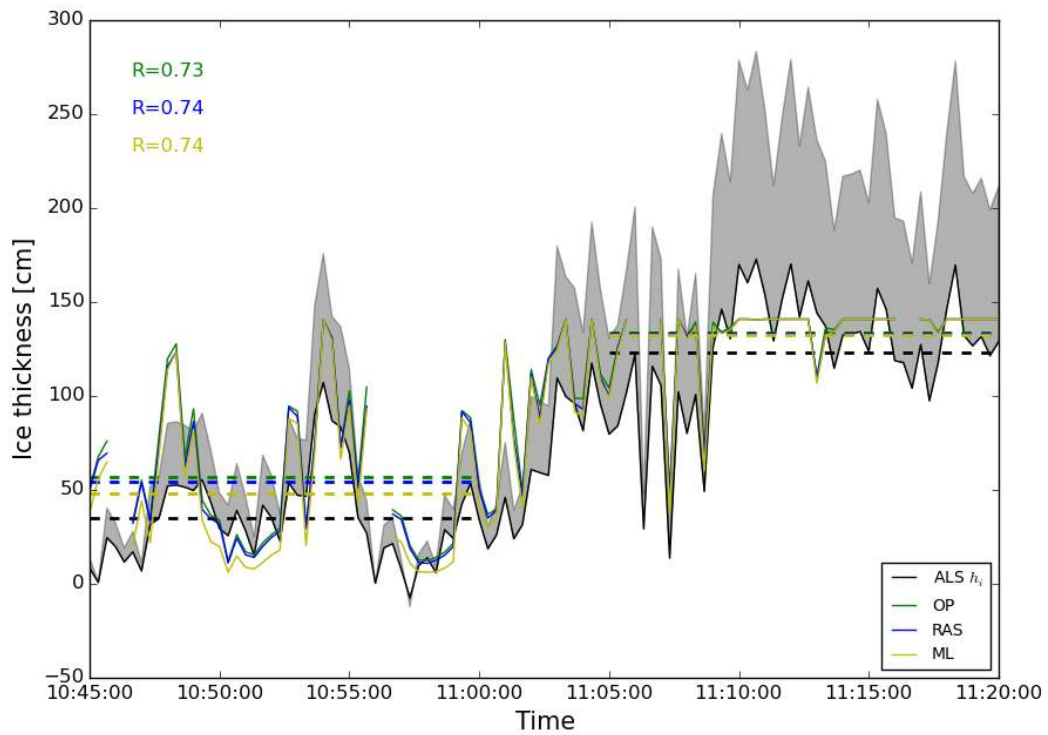


**Figure II.6.:** Comparison of sea ice thickness retrieved with current operational retrieval algorithm II\* (OP), with  $T_{eff}$  from Rasmus Tonboe's linear combination model (RAS), and with a multi-layer (10 layers) radiation model (ML) which includes a linear temperature profile in the Barents Sea along the Polar 5 flight track of 24th March, 2014. Brightness temperatures measured by EMIRAD were used for the retrieval. Along the track sea ice thickness was derived from ALS freeboard data.

## II.2.3. Ice concentration

### II.2.3.1. Problem by combining sea ice concentration in the retrieval

100% ice coverage is assumed in the current SMOS sea ice retrieval, which can cause significant underestimation of ice thickness if this condition is not met. In the SMOS+Sea Ice project, sea ice concentration with a resolution of 3.125 km derived from the Advanced Scanning Microwave Radiometer AMSR-2 on-board of JAXA's Global Change Observation Mission 1st-Waer satellite (GCOM-W1) will be used to estimate and eventually correct the bias caused by open water in the SMOS sea ice thickness product.

Due to the different resolutions, a first step for the correction is the disaggregation of low resolution SMOS data with the high resolution AMSR-2 data. Whereas the ice concentration and brightness temperature have linear dependence in the idealized case, the dependence between ice thickness and brightness temperature is not linear, which makes it a main challenge to combine AMSR-2 and SMOS data.

Therefore, we will first aggregate high resolution AMSR2 with a weighting function into 40 km SMOS resolution. SMOS observed TB is obtained from integrating radiance through the (directional) synthetic antenna pattern (CESBIO: SMOS level 2 Processor for Soil Moisture ATBD). Figure II.7 shows the one- and two-dimensional weighting functions with which we get new ice concentration map that corresponds to the receive behavior of SMOS antenna.

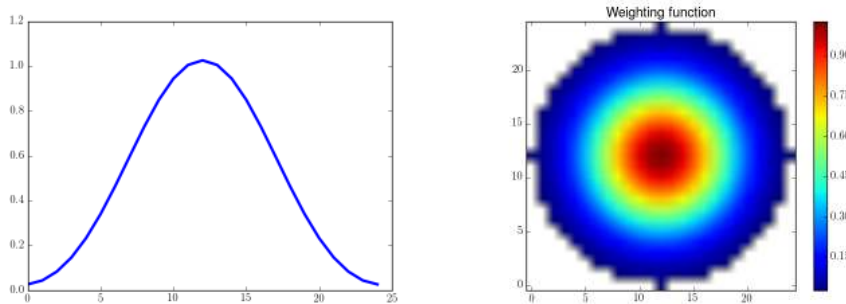


**Figure II.7.:** one-(left panel) and two-(right panel) dimensional weighting function that corresponds to the receive behavior of SMOS antenna

SMOS TB (intensity averaged over 0-40° incidence angle) can be seen as the sum of TB over sea ice ( $TB_{ice}$ ) multiplied with ice concentration  $C$  and TB over sea water ( $TB_{water}$ ) multiplied with  $1 - C$ . Thus, we can calculate  $TB_{ice}$  with following equation. We applied the antenna gain function (Figure II.7) of SMOS on  $C$ .

$$TB_{ice} = (TB - TB_{water})/C + TB_{water}, \quad (II.2)$$

SMOS TB and AMSR2 ice concentration in a region with lead opening in the Beaufort Sea (on Feb. 25, 2013) and in the marginal ice zone (MIZ) in the Barents Sea (on Mar. 24, 2014) are chosen to test eq.2 (Figure II.8). The calculated  $TB_{ice}$  shows unrealistically high values both in the MIZ and lead area (Figure II.9 and Figure II.10). The reason could be on one side that passive microwave sensors underestimate ice concentrations in thin ice areas, on the other side that due to the inverse relationship between  $TB_{ice}$  and  $C$  in eq. 2, small errors in  $C$  cause large errors in  $TB_{ice}$ .

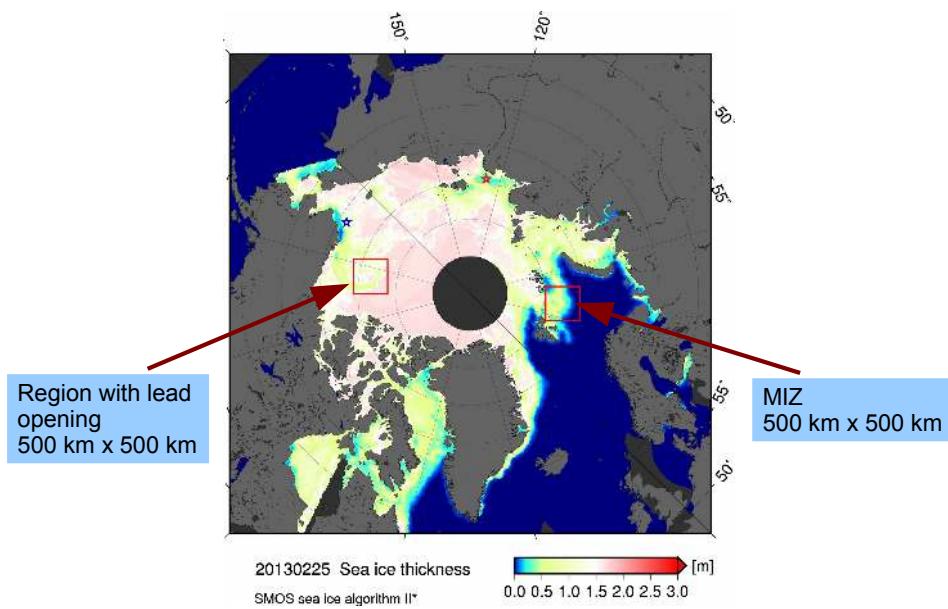


**Figure II.8.:** Test region

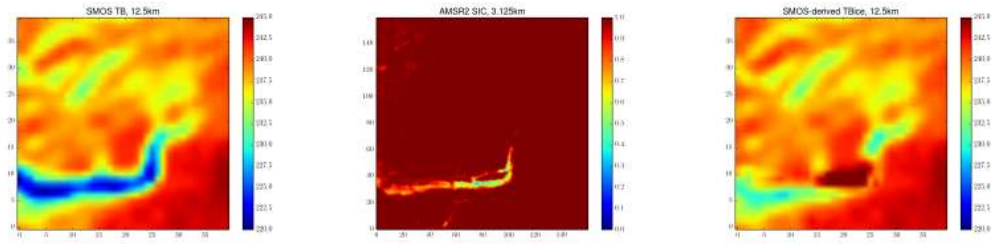


**Figure II.9.:** SMOS TB, AMSR2 sea ice concentration, and corrected  $TB_{ice}$  in the Beaufort Sea on Feb. 25, 2013.

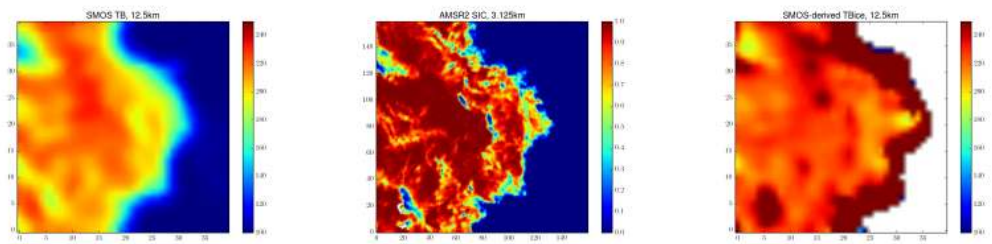


**Figure II.10.:** SMOS TB, AMSR2 sea ice concentration, and corrected  $TB_{ice}$  in the Barents Sea on Mar. 24, 2014.

### II.2.3.2. MODIS-derived ice thickness in the Kara Sea

*Marko Mäkynen, FMI*

We investigate the impact of sea ice concentration on SMOS TB and sea ice thickness retrieval, by simulating TBs with MODIS-based ice thickness in the Kara Sea. MODIS-based ice thickness charts with a resolution of 1 km have been provided by Finnish Meteorological Institute (FMI).

FMI has processed MODIS ice surface temperature (IST) and sea ice thickness (SIT) datasets over the Barents and Kara Seas for the development and validation of the SMOS sea ice algorithms. In general, the datasets were processed as in the previous SMOSIce project. The MODIS IST and SIT datasets cover the whole Kara Sea and large part of the Barents Sea including Svalbard area. The size of the target area is 1850 by 2200 km. The target area includes large thin ice areas even in the middle of the winter due to many re-occurring polynyas. Time periods for the MODIS data are Jan-Apr 2014 and Oct 2014-Apr 2015. These time periods included a lot of cloud-free cold weather periods suitable for the MODIS based SIT retrieval.

Only Terra night time MODIS data is used in the ice thickness retrieval so that the uncertainties related to the effect of the solar shortwave radiation and surface albedo are excluded. After mid-March only the afternoon MODIS data is utilized as the morning data starts to have too low sun zenith angles. Landmask for the MODIS data was derived from the NASA's MODIS 250 m land-water mask product (MOD44W). Coastline data was extracted from the landmask. Same method as previously was used in the cloud masking. Discriminating clear-sky from clouds is nowhere more difficult than in winter nighttime conditions (Frey et al., 2008), and there are cases of unmasked thin clouds and fog in the images.

The MODIS IST under clear sky condition is obtained with a split-window technique, where "split-window" refers to brightness temperature difference in the 11-12 micrometer atmospheric window (Hall et al., 2004). This technique allows for the correction of atmospheric effects primarily due to water vapor. The rms-accuracy of IST at the best 1.3 K (Hall et al., 2004).

Level ice thickness from the measured IST can be estimated on the basis of surface heat balance equation. Major assumptions here are that the heat flux through the ice and snow is equal to the atmospheric flux and temperature profiles are linear in ice and snow (Yu and Rothrock, 1996; Mäkynen et al., 2013). Atmospheric forcing data for solving the surface heat balance was again provided by the HIRLAM model data calculated at FMI. Only major difference to previous SIT calculation is modification of the snow ( $h_s$ ) vs. sea ice thickness ( $h_i$ ) relationship. This relationship is needed to convert so-called thermal ice thickness (no snow cover assumed) from the heat balance equation to ice thickness of snow covered ice. Previously, this relationship was slightly discontinued at  $h_i = 20\text{cm}$ :

$$\begin{aligned}
 h_s &= 0 \text{ m} && \text{for } h_i < 0.05 \text{ m} \\
 h_s &= 0.05 \times h_i && \text{for } 0.05 \text{ m} \leq h_i < 0.2 \text{ m} \\
 h_s &= 0.09 \times h_i && \text{for } h_i \geq 0.2 \text{ m}
 \end{aligned}$$

This discontinuation yielded equal  $h_i$  values for thermal ice thicknesses slightly below and

above 26 cm. New  $h_s$  vs.  $h_i$  relationship removed this error (Figure II.11):

$$\begin{aligned}
 h_s &= 0 \text{ m} && \text{for } h_i < 0.05 \text{ m} \\
 h_s &= 0.05 \times h_i && \text{for } 0.05 \text{ m} \leq h_i < 0.15 \text{ m} \\
 h_s &= 0.21 \times h_i - 2.4 && \text{for } 0.15 \text{ m} \leq h_i < 0.20 \text{ m} \\
 h_s &= 0.09 \times h_i && \text{for } h_i \geq 0.2 \text{ m}
 \end{aligned}$$

Examples of MODIS IST and SIT charts are shown in Figure II.12.

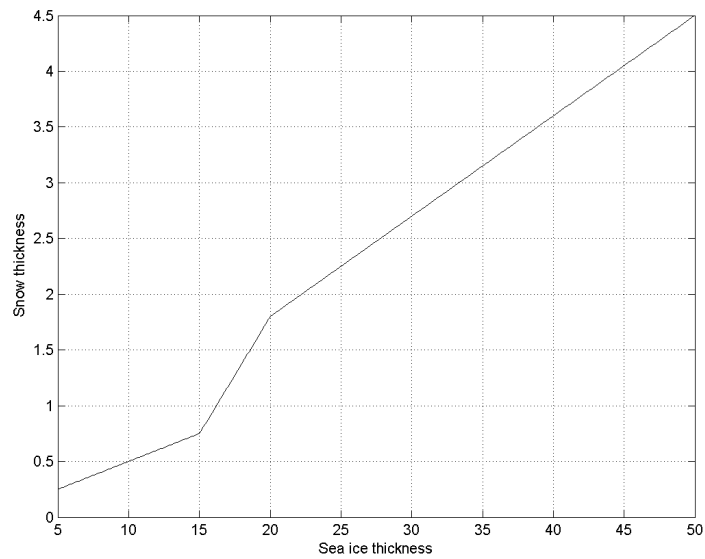


**Figure II.11.:** New snow vs. sea ice thickness relationship for the MODIS ice thickness retrieval.

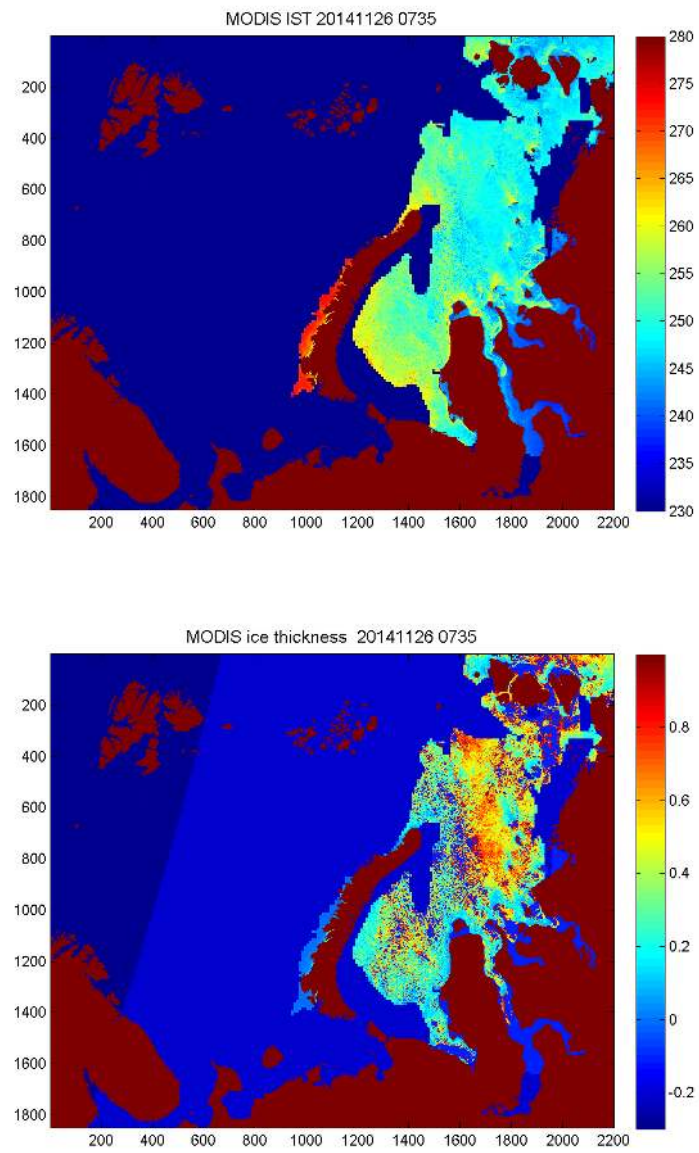


**Figure II.12.:** MODIS IST (upper figure) and SIT (lower figure) charts on 26 Nov. 2014.

A detailed study of MODIS SIT uncertainty has been conducted by (Maekynen et al., 2013) using data for three winters in 2008-2011. The accuracy analysis of the retrieved SIT was conducted with different methods, taking into account inaccuracy of the HIRLAM weather forcing data. Maximum reliable SIT under different air temperature and wind speed ranges was determined. It is 35-50 cm under typical weather conditions (air temperature  $< -20^\circ$ , wind speed  $< 5 \text{ m s}^{-1}$ ) present in the MODIS data. The accuracy is the best for the 15-30 cm thickness range, around 38%. The largest SIT uncertainty comes from air temperature data, and IST and downward longwave radiative flux have somewhat smaller roughly equal contributions. Our ice thickness limits are more conservative than those in many previous studies where numerical weather prediction model data was not used in the SIT retrieval. For the previous MODIS SIT dataset in the SMOSIce project it was found that the HIRLAM model typically underestimated air temperature ( $T_a$ ) in cold conditions, e.g. the mean bias was  $-2.3^\circ$  in the  $T_a$  range of  $-25$  to  $-20^\circ$ . This was determined using coastal weather station data. This HIRLAM underestimation of  $T_a$  leads to underestimation of SIT as now the  $T_a - IST$  difference resembles that of a thinner ice. In the current SMOS+SeaIce MODIS SIT data, this kind of HIRLAM  $T_a$  underestimation was not found. Thus, in the new MODIS SIT data there are likely somewhat larger SIT values for thin ice ( $< 0.5$  m).

### II.2.3.3. Case study in the Kara Sea

For the comparison of SMOS TB and simulated TB, we applied ice concentration in eq. 2 and weighted with antenna gain function for the simulated TB (Figure II.13). We used two different ice concentration datasets for the TB simulation with MODIS-derived ice thickness: 3.125 km AMSR2 ice concentration retrieved with ASI algorithm and 25 km merged SSMIS ice concentration retrieved with a combination of NASA Team and Bootstrap algorithms.

The TB difference between SMOS TB and simulated TB shows different distributions for the two ice concentration datasets. This means, the uncertainty estimation of SMOS ice thickness caused by ice concentration depends highly on which data we use (Figure II.14)

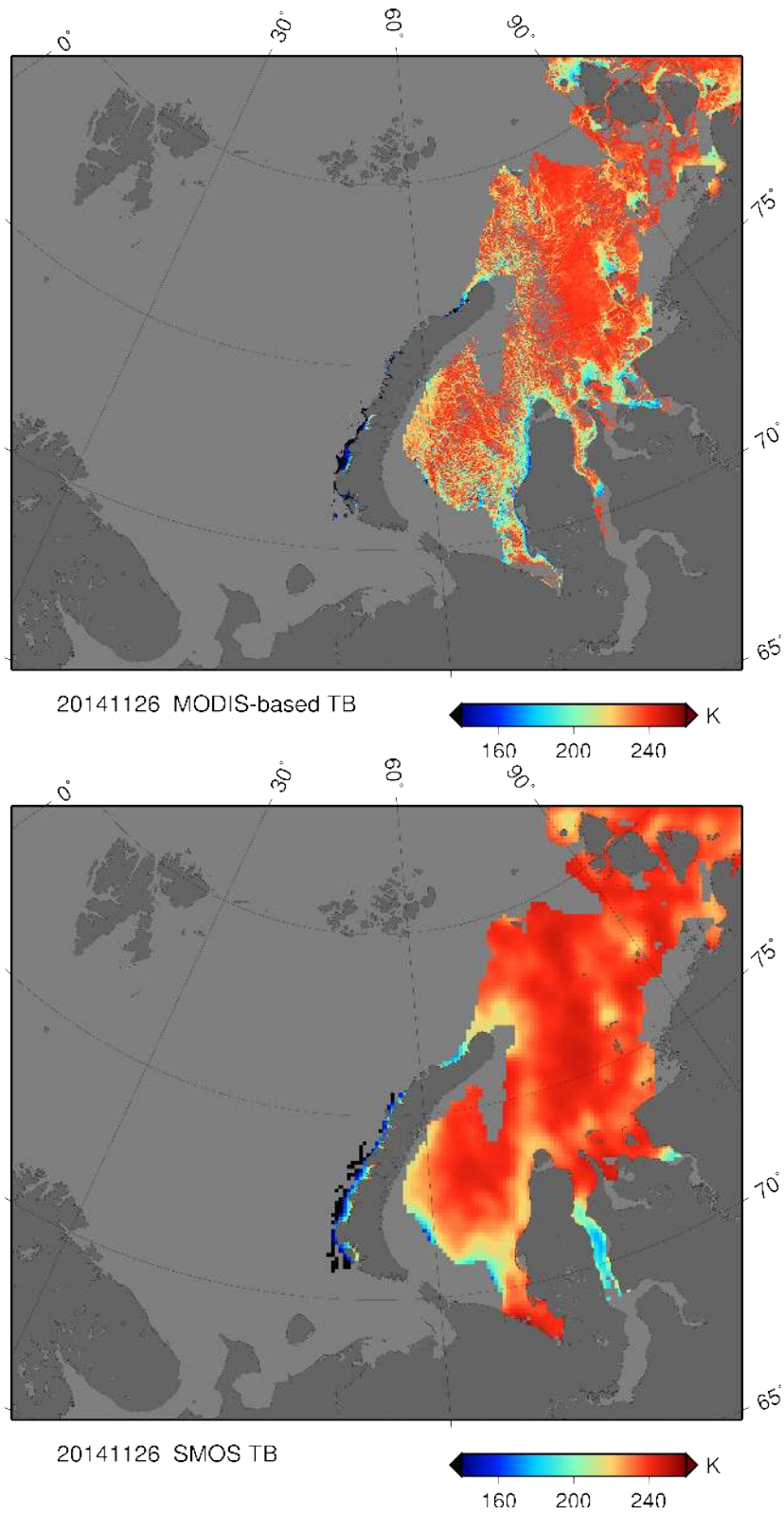


**Figure II.13.:** 1 km MODIS-based TB calculated with MODIS ice thickness and the radiation model used in operational retrieval (upper); 12 km SMOS TB (lower).

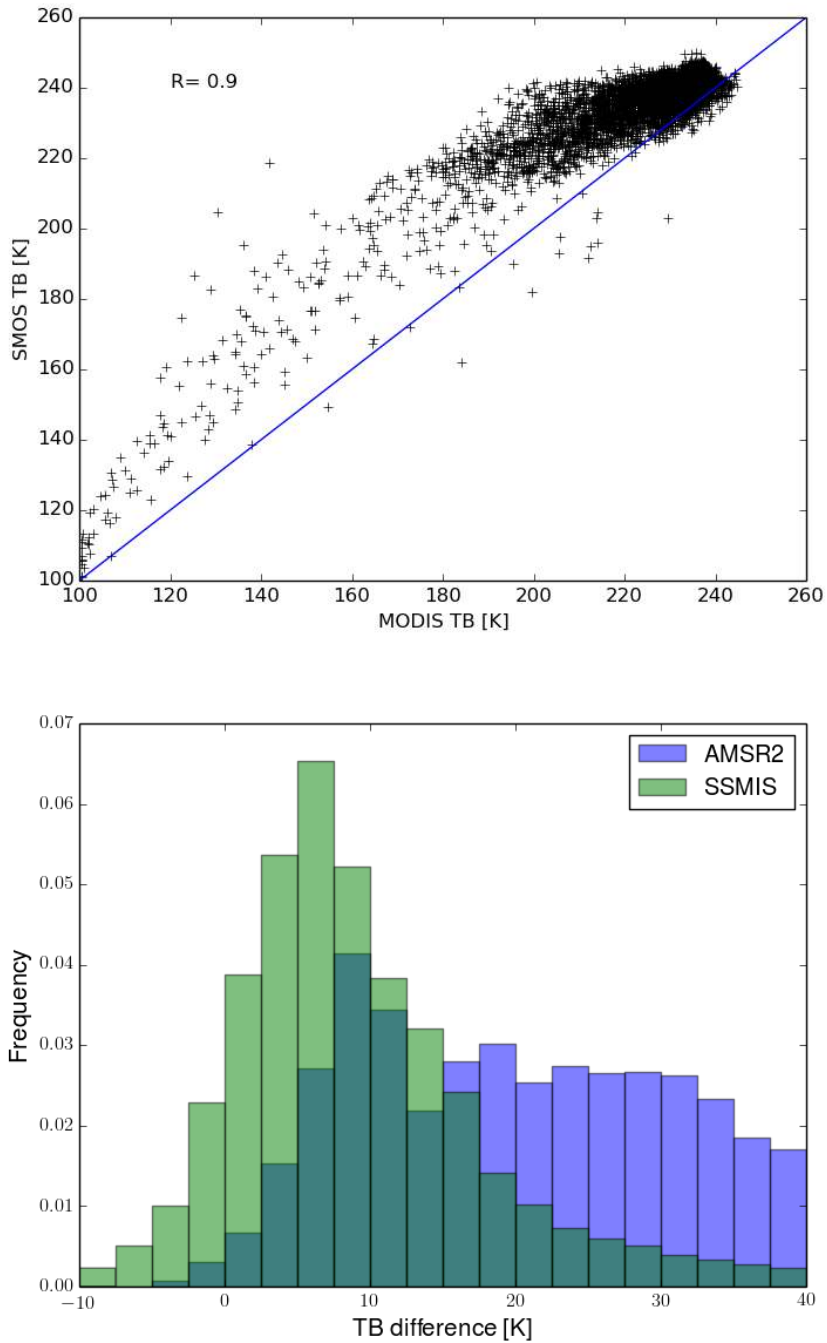


**Figure II.14:** The correlation between simulated TB (using AMSR2 ice concentration) and SMOS TB (upper); the histogram of simulated TB difference with and without ice concentration (blue for AMSR2, green for SSMIS) using MODIS ice thickness (lower).

Furthermore, as Figure II.15 and Figure II.16 show, AMSR2 ice concentration and MODIS ice thickness are almost linearly correlated under low ice concentration. Combining ice concentration into SMOS TB in this area (see eq. 2) will result in very thick ice for the ice-covered area. Therefore, it is better to assume 100% ice coverage in the sea ice retrieval under low ice concentration. The underestimation caused by AMSR2 ice concentration is on average less than 10 cm (for  $C < 50\%$ ).

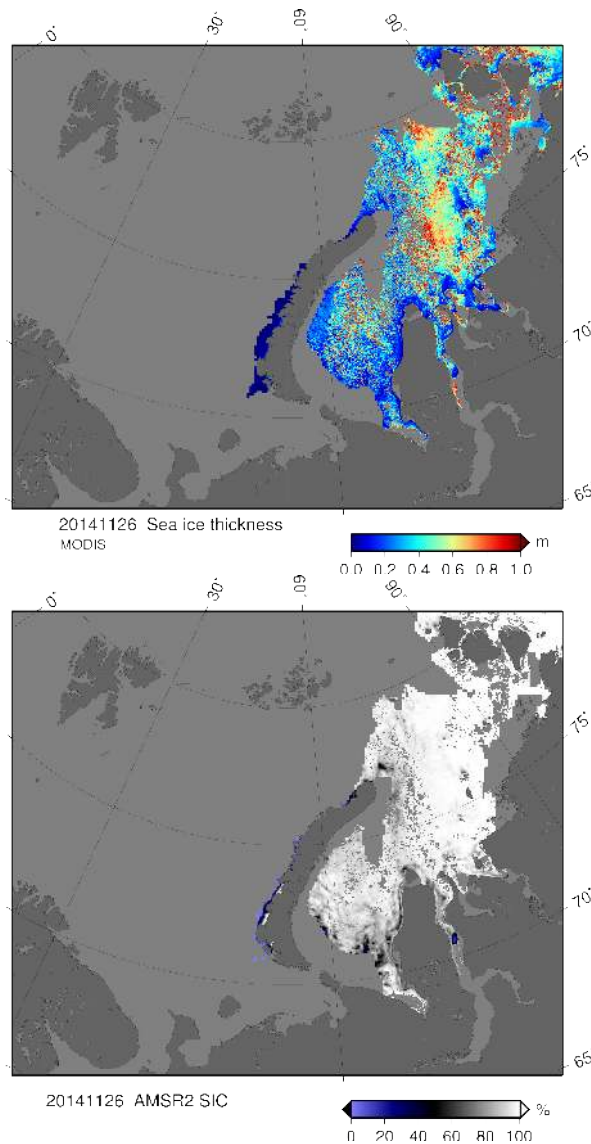


**Figure II.15.:** MODIS-derived SIT in a resolution of 1 km (upper) and AMSR2 SIC in a resolution of 3 km (lower). Date: Nov. 26, 2014.

#### II.2.3.4. Conclusion

Ice concentration impact on the SMOS ice thickness retrieval is not as significant as we assumed in the MIZ. The case study with MODIS-derived ice thickness in the Kara Sea shows that MODIS-derived ice thickness and AMSR2 ice concentration are almost linearly correlated under low ice concentration, which means that under low ice concentration, the 100% ice coverage assumption has less impact on the ice thickness retrieval than suspected.

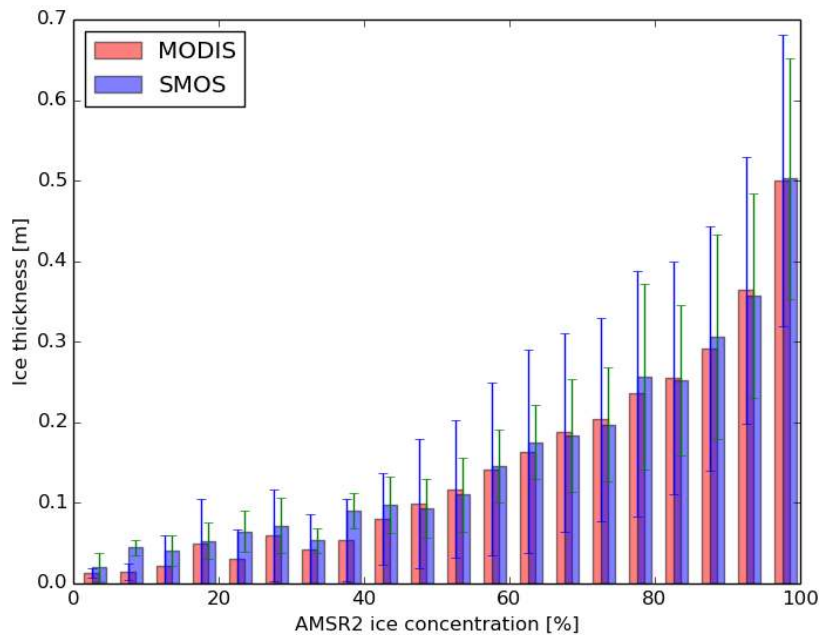


**Figure II.16.:** 1 km MODIS ice thickness is averaged into 3 km grids to match the AMSR2 ice concentration. SMOS ice thickness is retrieved with the assumption of 100% ice coverage. AMSR2 sea ice concentration and MODIS ice thickness are almost linearly correlated under low ice concentration. Date: Nov. 26, 2014.

Correction with ice concentration in this case can cause higher uncertainty and bias in the retrieved ice thickness. The comparison between SMOS TB and simulated TB (based on MODIS ice thickness) shows that the ice concentration correction in TB depends highly on which ice concentration dataset is used. Even the high resolution AMSR2 ice concentration data set can cause unrealistically thick ice in the MIZ and leads area due to the inverse relationship between  $TB_{ice}$  and  $C$ .

#### **II.2.4. Refinement of the look-up table for the correction from plane layer ice thickness to mean ice thickness**

In retrieval Algorithm I and II, plane ice layer is assumed for the SMOS footprint which is about 35 km at nadir. Information about the thickness distribution is needed to correctly estimate the mean ice thickness. However, the thickness distribution within a SMOS footprint is not known and has to be parameterized with sparse measurements. In Algorithm II\* we introduced a lognormal function for the thickness distribution, with logmean and logsigma as parameters. Logsigma is estimated based on the NASA's Operation IceBridge(OIB) data from 2012 and 2013. To save processing time, the conversion from plane layer ice thickness to heterogeneous mean ice thickness is done based on a look-up table.

An analysis of the v2.1 SMOS ice thickness data retrieved with Algorithm II\* has shown several gaps in the histogram of the data, which is caused by the coarse-resolved look-up table (Figure II.17, Figure II.18). We rerun the look-up table with a much finer bins in the ice thickness as well as ice temperature and ice salinity. The ice thickness data with new look-up table reveals less gaps in the histogram, however, the gaps still exist in the higher range of ice thickness. To avoid this inconsistency, we parameterized the look-up table with a polynomial fit function (degree = 3) for each ice temperature and ice salinity. As can be seen in Figure II.19, the polynomial fit function can reproduce the look-up table at each  $T_{ice}$  and  $S_{ice}$  very well. The polynomial fit function can prohibit the inconsistency, which exists in the look-up tables, thus avoid the gaps in the histograms of ice thickness data (Figure II.20). These polynomial fit functions replace the look-up table for the ice thickness correction in Algorithm III.

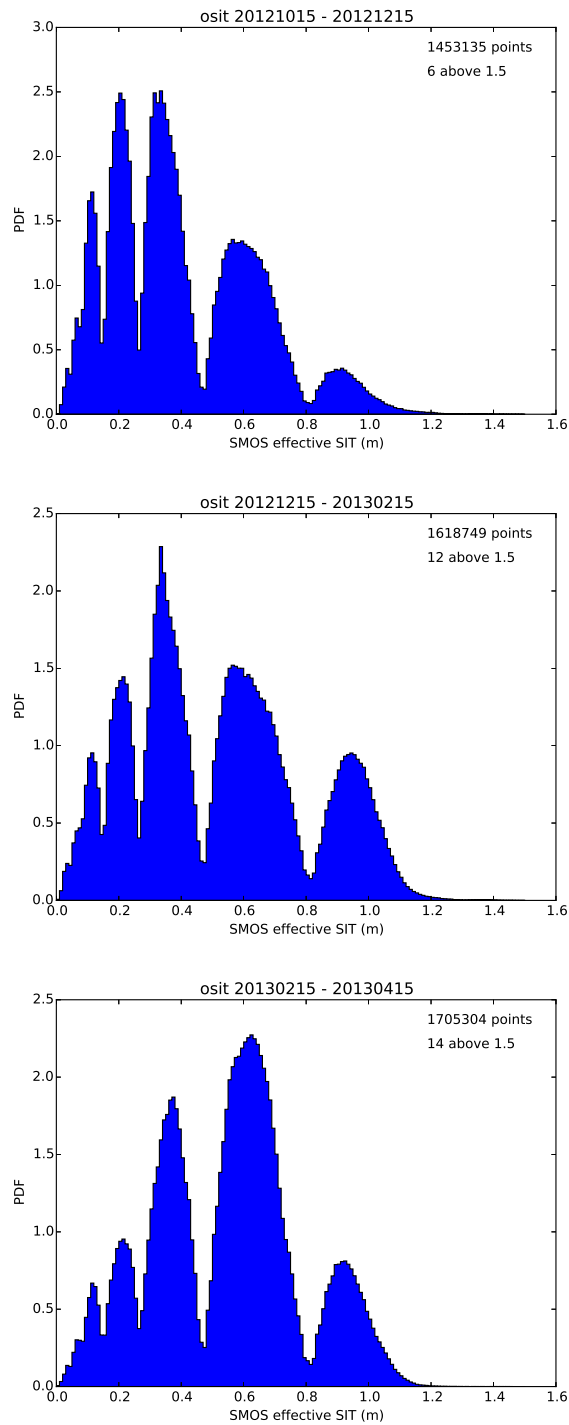


**Figure II.17.:** Gaps in the histogram of effective sea ice thickness data, credit to Steffen Tietsche from ECMWF

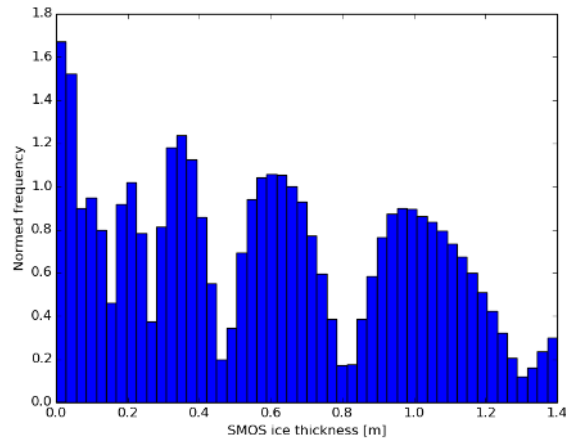


**Figure II.18.:** Gaps in the histogram of sea ice thickness v2.1 data during the winter season of 2012-2013. Only data points with saturation ratio less than 95% are considered. Number of data points: 8497650

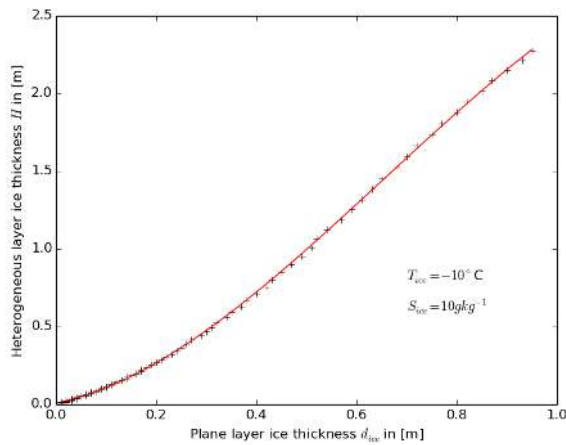


**Figure II.19.:** Black crosses are the plane layer ice thickness  $d_{ice}$  vs. heterogeneous layer mean ice thickness  $H$  at  $T_{ice} = -10^\circ$  and  $S_{ice} = 10 \text{ g kg}^{-1}$ , the red line is the polynomial fit with degree 3.

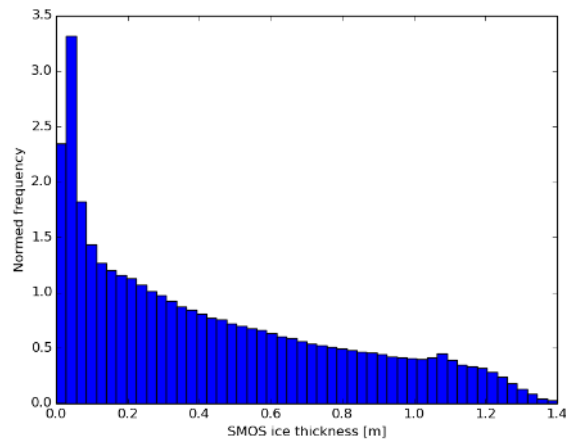


**Figure II.20.:** The histogram of SMOS sea ice thickness v3.1 data during the winter season of 2012-2013 using polynomial fit function instead of look-up table for the plane layer ice thickness correction. Only data points with saturation ratio less than 95% are considered. Number of data points: 7209153

### II.2.5. Sea ice thickness uncertainty estimation in Algorithm III

There are several factors that cause uncertainties in the sea ice thickness retrieval: the uncertainty of the SMOS TB, the uncertainties of the auxiliary data sets, and the assumptions made for the radiation and thermodynamic models.

For our retrieval, we average TB over the incidence angle range of 0–40°. There are mostly more than 100 TB measurements at each grid point in the Arctic region per day. By averaging the measurements, we reduce the measurement uncertainty. We describe the variability of TB by dividing the standard deviation of TB with the square root of the number of measurements during one day at each grid point. Mostly, the TB variability is lower than 0.5 K in the Arctic, except for the strongly RFI affected regions. The uncertainties of  $T_{ice}$  and  $S_{ice}$  depend on the uncertainties in  $T_a$  and SSS, as well as the uncertainty caused by the missing physics. Both  $T_a$  and SSS are derived from model outputs. Due to the sparse observations in the polar regions,  $T_a$  and SSS themselves contain large uncertainties.

A first estimation of SMOS-retrieved ice thickness uncertainty is made with Algorithm II based on the  $std(TB)$ ,  $std(T_{ice})$  and  $std(S_{ice})$ . The  $std(TB)$  is calculated at each pixel by dividing the standard deviation of all available TB measurements with the  $\sqrt{\text{number of TB measurements}}$  for each day. The  $std(S_{ice})$  is calculated based on the  $std(SSS)$  and  $d_{ice}$ . The estimation of  $std(T_{ice})$  is rather difficult, because it depends not only on  $T_a$ , but also on the assumptions made in the thermodynamic model. As a first approximation, we assume 1 K for the  $std(T_{ice})$ , which is estimated with the variations in  $T_a$ . At present, each error caused by the brightness temperature, ice salinity, and ice temperature is estimated by keeping the other parameters constant. Errors caused by the assumptions about fluxes and snow thickness have not yet been included. In the Algorithm II\*, the ice thickness uncertainty is the sum of uncertainties caused by above mentioned parameters- brightness temperature, ice temperature, and ice salinity. Generally, the uncertainty increases with increasing ice thickness. For thinner ice the relationship between ice thickness and ice thickness uncertainty is almost linear.

In Algorithm III, besides the above mentioned uncertainty factors, we also consider the uncertainty caused by the thickness distribution function. The uncertainty caused by this function can be estimated using the standard deviation of  $\log\sigma$ , which is the constant parameter in the lognormal thickness distribution function.  $\log\sigma$  and  $std(\log\sigma)$  are derived from 6 years NASA OIB airborne observations of ice thickness, with  $\log\sigma$  equals to 0.6 and  $std(\log\sigma)$  equals to 0.05. The average ice thickness uncertainty caused by the distribution function is less than 10 cm.

### II.2.6. Operational processing

Since July 2014, SMOS-derived thin ice thickness has been processed operationally and disseminated to the users with a latency of about 24 hours. The daily averaged mean ice thickness data has been made available via data platform <http://icdc.zmaw.de>. The processing steps and the time cost are listed in the Figure II.21.

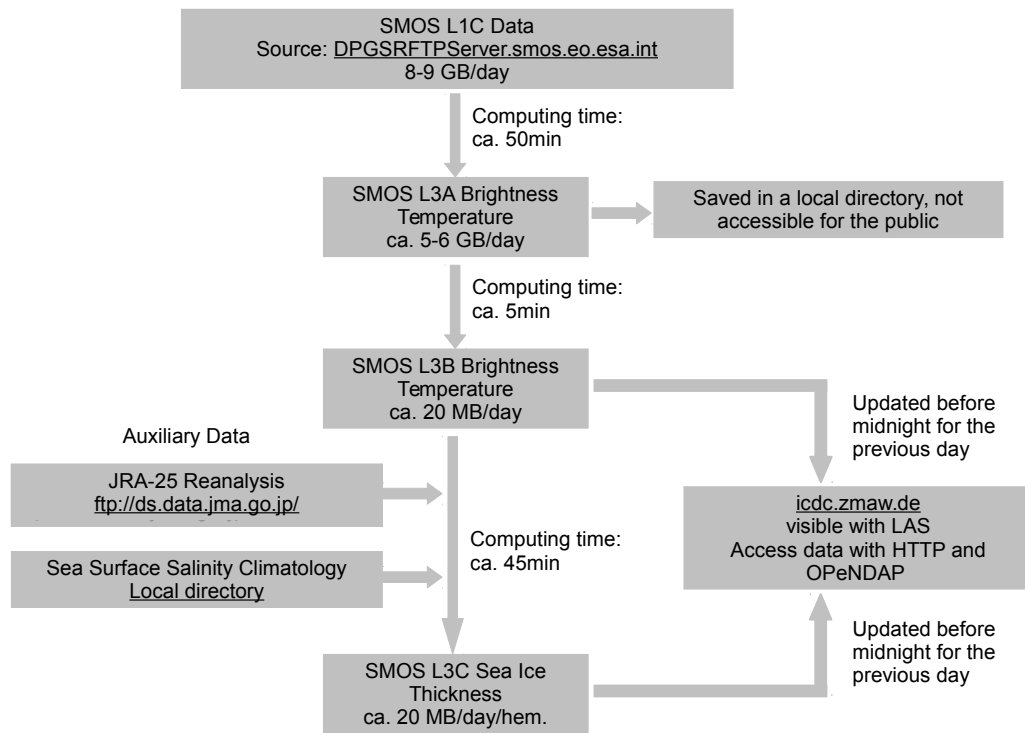


Figure II.21.: Schematic flow chart of the operational processing

**Table II.5.:** Coverage and spatial resolution of L3B SMOS TB and L3C SMOS Ice Thickness data

Spatial coverage	Northern hemisphere poleward of 50°N
Spatial resolution	12.5 km x 12.5 km, polar-stereographic grid of the NSIDC polar-stereographic projection at standard latitude of 70°N
Geographic longitude	0°E to 360°E
Geographic latitude	50°N to 90°N
Dimensions	608 columns x 896 rows
Format	NetCDF

The characteristics of L3B SMOS TB and L3C SMOS ice thickness data are summarized in Table II.5.

## II.3. The thermal microwave effective temperature of sea ice-temperature and salinity profile parameterization schemes

*Rasmus Tonboe, DMI*

From the cold air to the relatively warm water there is a steep temperature gradient in the snow-ice system (Tonboe et al., 2011). Also the salinity varies from the top to the bottom of the ice because of different growth rates. These gradients are not represented in a slab model or even a two layer model and together with the microwave absorption and scattering this is affecting the effective temperature sometimes called the skin temperature. Therefore, to overcome this problem we set-up a temperature and salinity profile parameterization based on the optical thickness of the layer and its optical depth to compute the effective temperature using a limited number of physical input parameters. The effective temperature is important in many applications involving radiative transfer of the atmosphere or the sea ice itself. It is used for regional error reduction in sea ice concentration schemes, it is used for atmospheric sounding over sea ice and for ice thickness retrieval using SMOS data. Here we are testing three different parameterizations of the effective temperature at L-band and comparing them to detailed simulations from a combined thermodynamical model and MEMLS (methodology described in Tonboe et al. (2011)).

- The linear combination (LinC),
- The physical temperature at the penetration depth (Pd),
- The integrated emitting layer physical temperature weighted with intensity (IntT).

### II.3.1. The temperature profile

Linear temperature gradients within the snow and the ice are a good approximation to the temperature profile in sea ice (Nakawo and Sinha, 1981). This has been shown using measurements from thermistor strings frozen into sea ice. The thermal conductivity of ice is an order of magnitude greater than that of snow. The thermal conductivity of snow is about  $0.3 \text{ W K m}^{-1}$  primarily a function of snow density and sea ice is about  $2.1 \text{ W K m}^{-1}$  a function of salinity, temperature and porosity. However, these two values are typical for snow and sea ice and they are therefore used in the parameterization here. The temperature gradient in the ice and snow is estimated using (Nakawo and Sinha, 1981) (their eqs. 6 and 7) and the temperature profile can be constructed using these equations, the surface temperature and the water temperature at 271.3K, the snow and ice depth. We use a vertical resolution of 1 cm, this means that if the snow thickness is 0.1m and the ice is 0.5m thick then there are 60 layers in the profile with temperatures according to the linear temperature profile described above.

### II.3.2. The salinity profile

Rapid initial freezing at the water surface leaves a high salinity at the ice surface layer even when the ice eventually has grown thicker. As the growth rate decreases because of the insulating effect of the ice also the salinity of newly formed ice near the ice water interface decreases. The sea ice salinity as a function of the growth rate of the ice and the water salinity is described by (Nakawo and Sinha, 1981). Inspecting simulated salinity profiles initialized

with measurements of surface salinity at 4 different sites, two on each hemisphere reveals a very similar initial behavior as seen in Figure II.22). A simple model for the sea ice salinity as a function of depth is fitting the salinity profiles. The salinity  $S$  i.e.

$$S = 6 + \frac{16}{(1 + 100d)^2}, \quad (\text{II.3})$$

where  $d$  is the depth in meters.

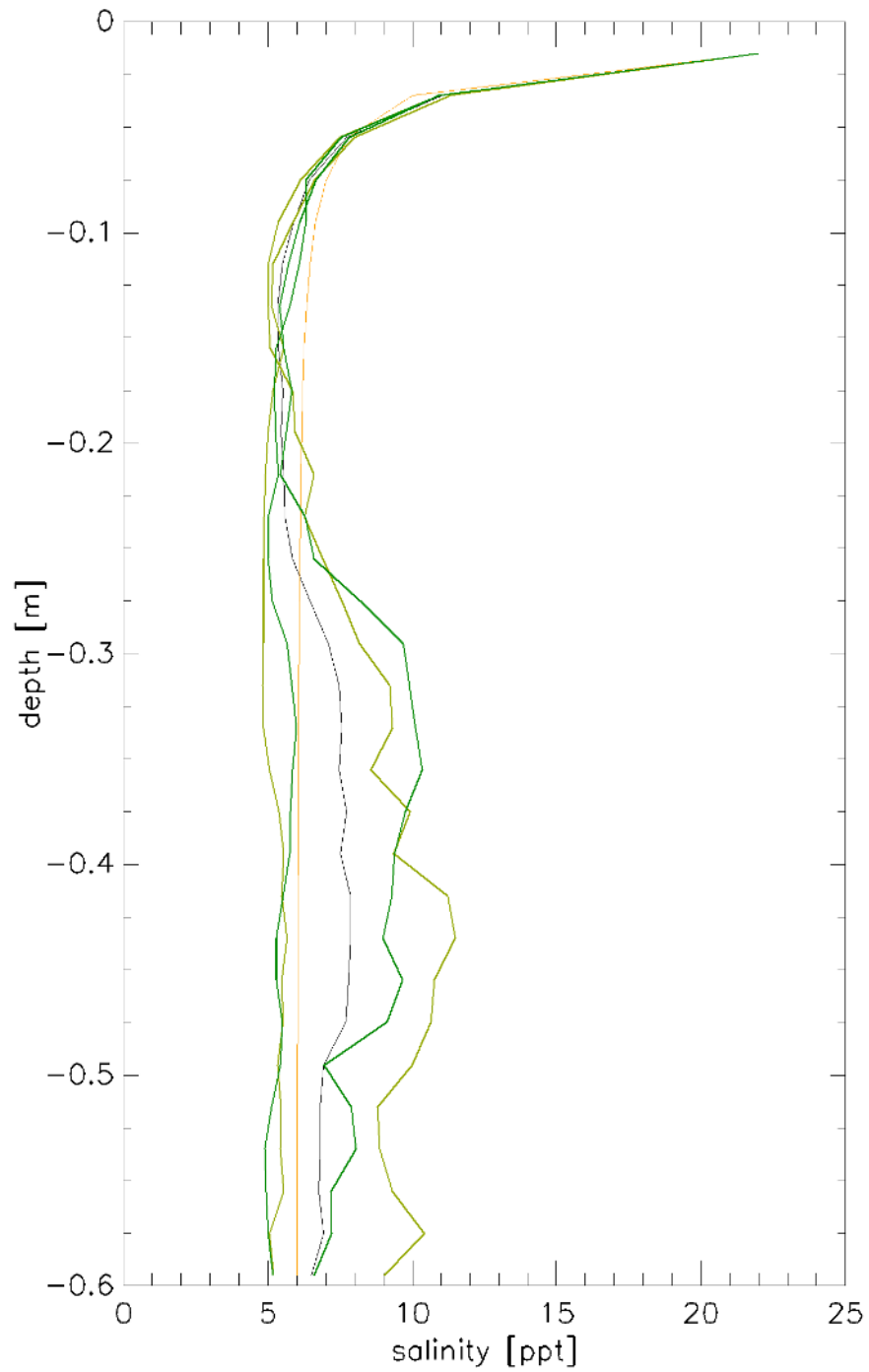


**Figure II.22.:** The simulated salinity of first-year ice initialized with measurements of surface salinity at two sites on each hemisphere in green. The black curve is the average salinity of the four individual profiles and the yellow curve is the model in eq. 3.

### II.3.3. The effective temperature estimation

We test three different ways of computing the effective temperature based on a limited number of input parameters and for two of them the parameterized temperature and salinity profiles. From the introduction, the three different effective temperature estimation methods:

- The linear combination (LinC), at fixed penetration to ice thickness ratio:  $T_{eff} = aT_a + (1 - a)T_w$ , where  $T_a$  is the surface temperature,  $T_w$  is the water temperature (here 271.3K),  $a$ , is a coefficient depending on the penetration depth (here  $a=0.17$ ). This method only requires knowledge of the surface temperature. However, the factor,  $a$ , is a function of penetration depth, i.e. ice type, temperature, snow cover etc.
- The physical temperature at the penetration depth (Pd):  $T_{eff} = T(pd)$ , using optical thickness and transmission loss at the snow and ice surfaces. The optical thickness is computed at a resolution of 1 cm using the temperature profile and the salinity profile. This method requires knowledge of the snow and ice thickness and surface temperature.
- The integrated emitting layer physical temperature weighted with intensity (IntT), using the optical thickness, the transmission loss at the snow surface and the ice surface and the emission intensity at each layer and the temperature and salinity profiles described above. This method requires knowledge of the snow and ice thickness and surface temperature.

#### II.3.3.1. The extinction and emission

The transmission loss is computed only at the snow surface and at the snow ice interface. Between all other layers the transmission coefficient is 1. Scattering in the snow and sea ice is not significant at L-band. Anyway, for completeness the scattering is computed in the snow and in the sea ice using the improved Born approximation and spherical snow grains and brine pockets as scatters. The correlation length of the scatters is 0.1mm throughout the profile. The snow density is  $300\text{kgm}^{-3}$  and the ice density is  $920\text{kgm}^{-3}$ . The permittivity of the snow and ice is computed using a two-phase mixing formula where the background is either air or pure ice and the inclusions are either pure ice or brine. The brine volume is a function of the temperature and the salinity. The absorption is a function of the imaginary part of the permittivity. The emission intensity from each layer is equal to the absorption. The emission intensity measured above the surface is computed using radiative transfer.

#### II.3.3.2. Comparison to detailed simulations

Each of the three methods of computing the effective temperature has been compared to detailed simulations using a thermodynamical model and MEMLS. The reference profile (from the detailed simulations) is a site in the Ross Sea. The Ross Sea profile has relatively complicated snow structure from many snow precipitation events. The reference snow depth grows during the cold season from 0 m to about 0.6 m and the ice thickness ends at about 1.5 m. The surface temperature, the snow depth and the ice thickness are taken from the reference simulation and used in each of the three simplified models (LinC, Pd, and IntT) for computing the effective temperature and finally the effective temperatures are then compared. Figure II.23 is showing the 4 different  $T_{eff}$  during the first 400 time-steps in the model where the ice thickness is growing from 0.015 m to about 0.6 m.

The comparison between the LinC  $T_{eff}$  and the MEMLS reference simulation is shown as a scatterplot in Figure II.24. The bias is 0.08K and the standard deviation of the difference is

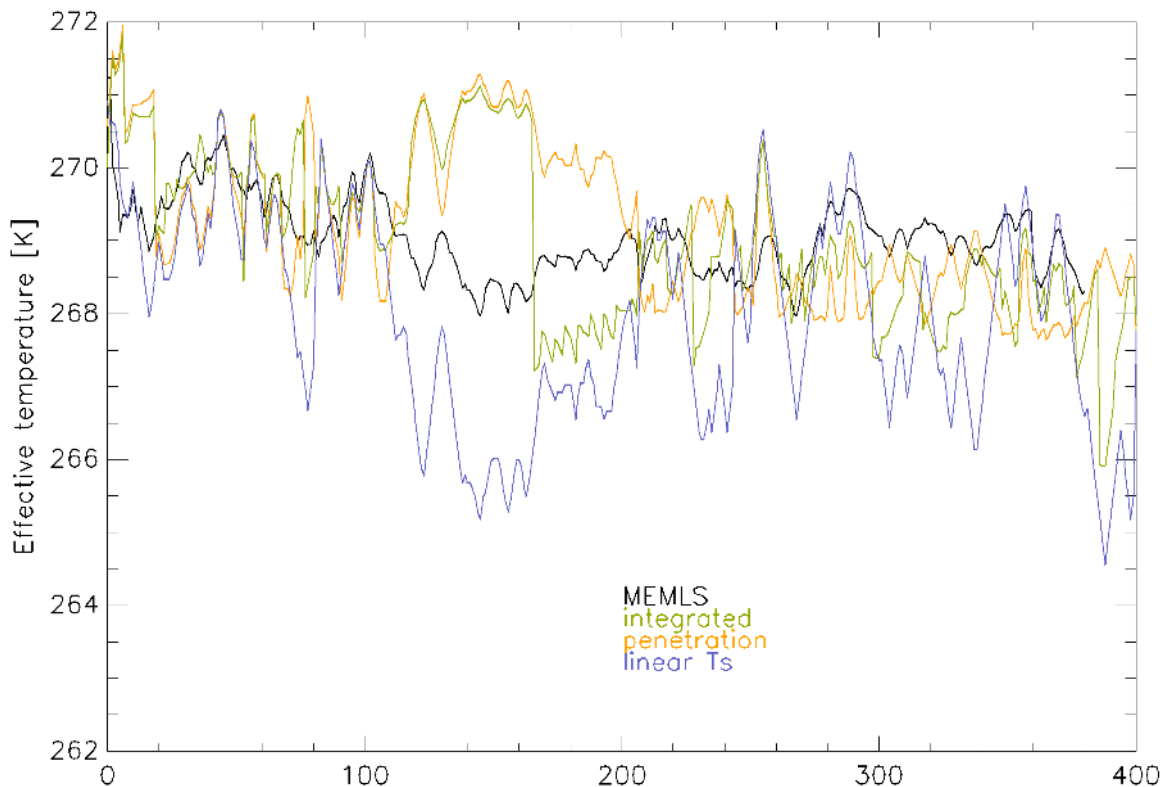


**Figure II.23.:** The effective temperature during the first 400 timesteps from the MEMLS simulation (reference) and the three simplified models.

1.51K. The a-factor has been tuned to minimize the bias (here  $a=0.17$ ). The entire dynamic range of the  $T_{eff}$  in both models is only about 7K.

The comparison between the  $T_{eff}$  using the MEMLS reference and the Pd model is shown as a scatterplot in Figure II.25. The bias is 0.29K and the standard deviation of the difference is 1.07K. There has been no attempt to minimize the bias by tuning the scattering and absorption in the Pd model. Also in this comparison the dynamic range for both models is about 7K.

The comparison between the  $T_{eff}$  using the MEMLS reference and the IntT model is shown as a scatterplot in Figure II.26. The bias is 0.43K and the standard deviation of the difference is 1.07K. There has been no attempt to minimize the bias by tuning the scattering and absorption in the integrated temperature model. Also in this comparison the dynamic range for both models is about 7K.

In the comparison between the IntT and the Pd model the bias is 0.14K, and the STD of the difference is 0.75K. In the IntT vs. the LinC models the bias is 0.35K, and the STD of the difference is 1.38K. For the Pd vs. the LinC model the bias is 0.21K, and the STD of the difference is 1.77K.

### II.3.4. Conclusion and Discussion

It is noted that the reference profile has a very complicated structure and the  $T_{eff}$  is therefore difficult to reproduce using relatively simple models. The LinC model was tuned to minimize

the bias. After doing that the STD of the difference is 1.51K. The two other models without tuning have a STD of the difference of 1.07K. However, the linear combination model is only using the surface temperature as input while the two other models are using the surface temperature, the snow depth and the ice thickness as input to compute the  $T_{eff}$ . When these input parameters are available then it is an advantage to use the integrated temperature model to minimize the uncertainty. However, for many applications the simplicity of the LinC model is attractive. The dynamic range of the  $T_{eff}$  for all the models including the MEMLS reference is about 7K.

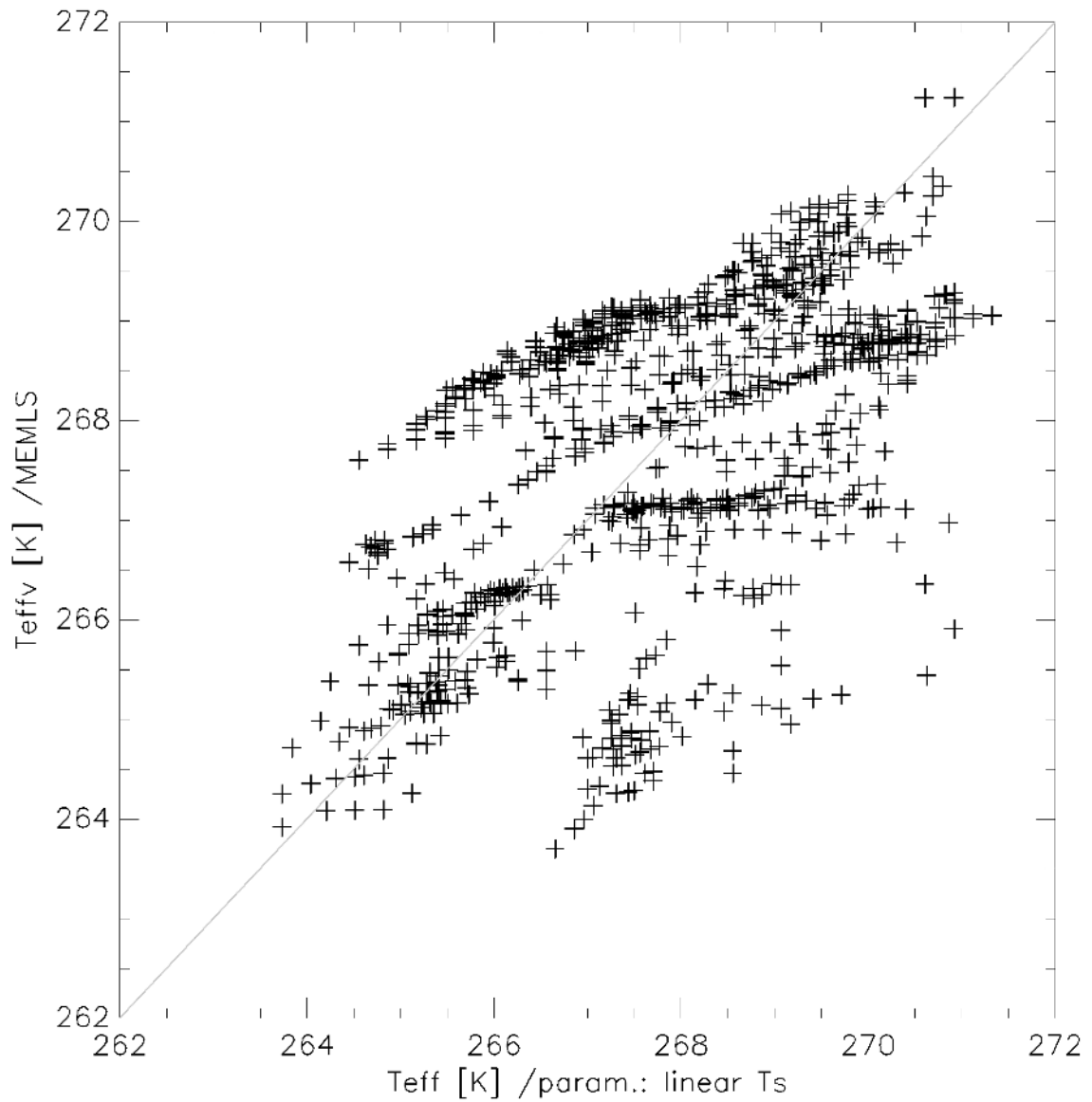


**Figure II.24.:** The comparison between the  $T_{eff}$  using the linear combination method and the MEMLS reference.

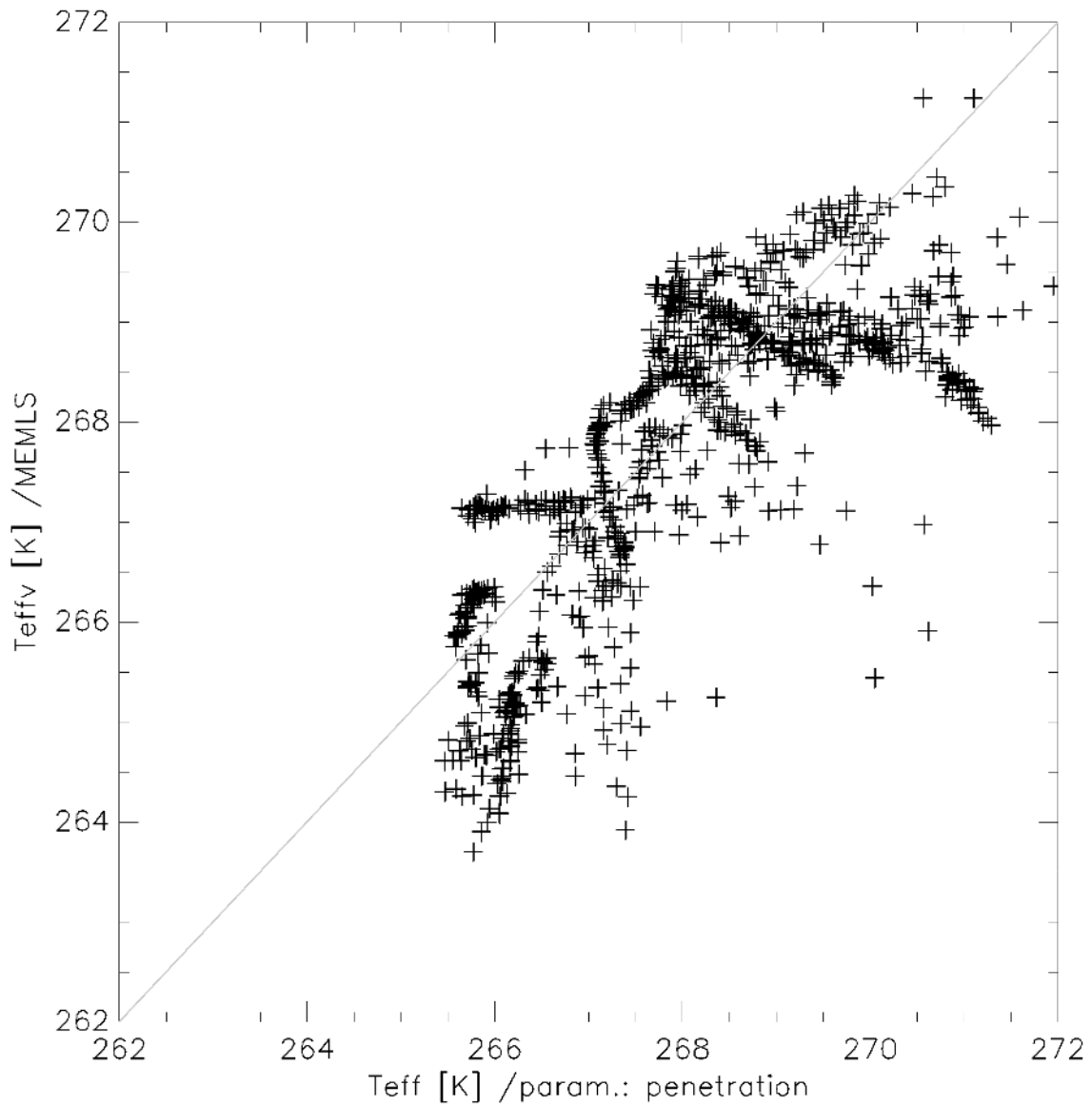


**Figure II.25.:** The comparison between the  $T_{eff}$  using the penetration depth method and the MEMLS reference.

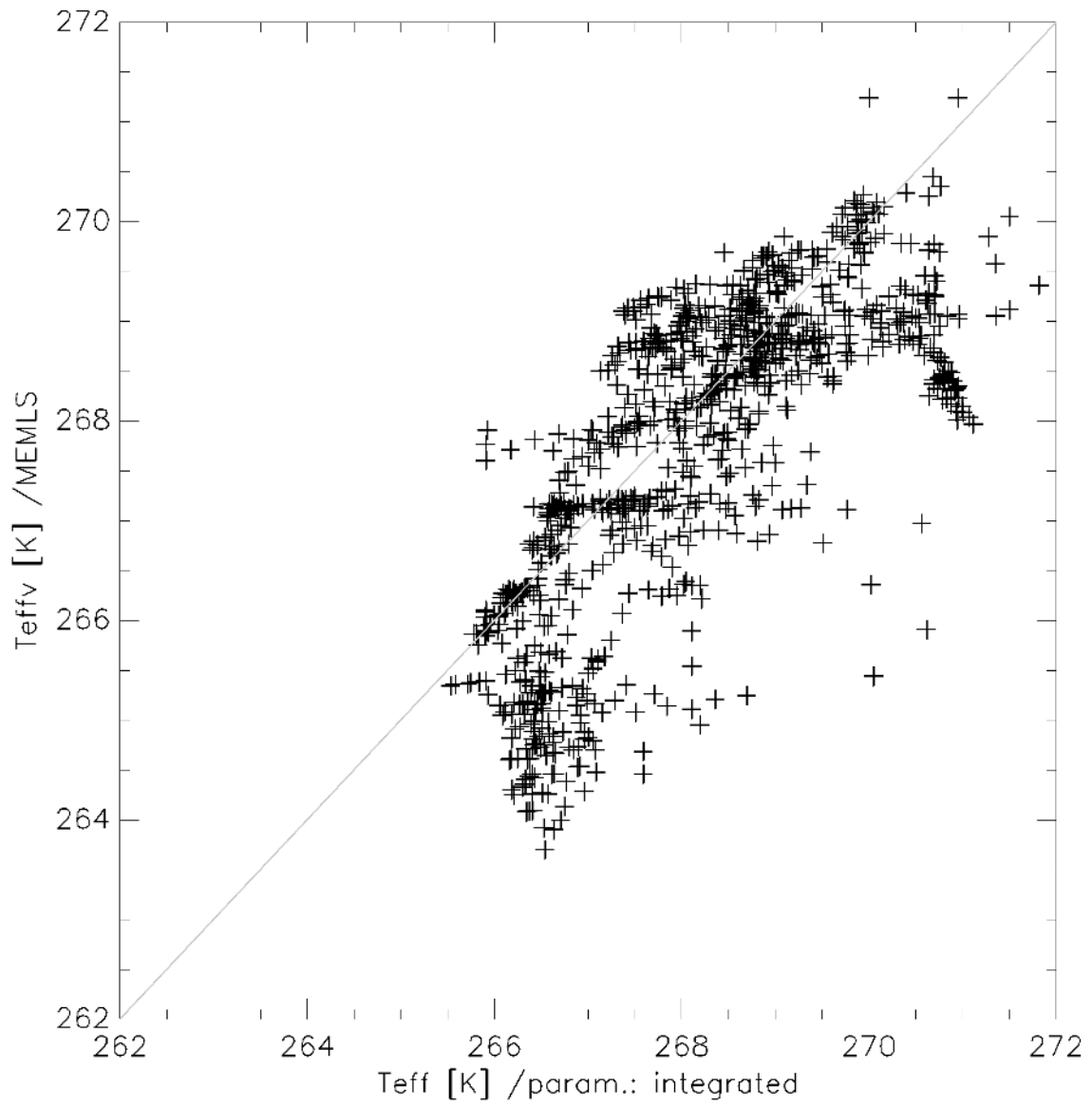


**Figure II.26.:** The comparison between the  $T_{eff}$  using the integrated temperature method and the MEMLS reference.

### III VALIDATION CAMPAIGN IN THE BARENTS SEA, MARCH 2014

*extracted from (Kaleschke et al., 2016)*

#### III.1. Introduction

The Task 4 of this project to analyze, exploit and interpret the datasets acquired in the ESA co-funded field campaigns to further refine the retrieval algorithms. The two ESA campaigns are both carried out in March 2014.

An algorithm developed at the University of Hamburg (UH) is based on a combined thermodynamic and radiative transfer model which accounts for variations of ice temperature and ice salinity (Tian-Kunze et al., 2014; Mecklenburg et al., 2016). The UH algorithm further accounts for an assumed lognormal shape of the statistical thickness distribution which results in a two to threefold maximum mean thickness up to 1.5 m. An empirical algorithm developed at the University of Bremen (UB) is based on training data obtained from ice growth models (Huntemann et al., 2014). The validation of the UB and UH SMOS sea ice thickness data products so far was limited to sparsely available ground truth and considerable uncertainties remained (Kaleschke et al., 2013; Maaß et al., 2015). A main limitation is the applicability of the SMOS sea ice thickness retrieval methods to cold seasons and excludes its use during melting periods.

A dedicated field campaign was conducted in the Barents Sea in March 2014 and gained a substantial amount of new validation data over thin ice. The new validation data comprises measurements from a helicopter based on RV Lance and the research aircraft Polar 5 operated from Longyearbyen airport, Spitsbergen. Sea ice thickness was measured using an electromagnetic induction (EM) system from the bow of RV Lance (Haas, 1998) and another EM-system towed below the helicopter (HEM) (Haas et al., 2009). Polar 5 was equipped among others with a laser scanner (ALS) used to determine sea ice freeboard and the radiometer EMIRAD-2 that measured the fully-polarimetric 1.4 GHz brightness temperature at nadir and tilted at 45°. This chapter will provide an overview of the campaign and will present first results of the validation of SMOS sea ice thickness products. We thereby assume the ship-based and airborne measurements as “ground validation data” to assess the quality of the SMOS sea ice thickness retrievals.

#### III.2. Physical conditions and experimental set-up

The main experimental area between Edgeøya and Kong Karls Land in the east of Svalbard belongs to the Barents Sea which in most years features only a seasonal ice cover despite its high latitude (Smedsrud et al., 2013). The boundary between the relatively warm water brought through the Norwegian Atlantic Current and the cold East Spitsbergen Current defines the oceanic Polar Front (Pavlova et al., 2014). The climatological minimum winter sea ice extent was given as the latitude of 77°N (Sandven et al., 1999). However, the physical conditions between the second half of January to the first half of March 2014 deviated



**Figure III.1.:** RV Lance during the field experiment in the Barents Sea, 24 March 2014. The EM system at the bow is visible by its red color. Photograph taken from Polar 5 aircraft by Stefan Hendricks.

strongly from the climatology. The air temperature measured at Hopen Island meteorological station was on average  $9^{\circ}\text{C}$  to  $12^{\circ}\text{C}$  above the climatological value as defined for the period of 1961 to 1990 (Strübing and Schwarz, 2014). Southerly winds pushed the sea ice at the coast between Barentsøya and Nordaustlandet and only a relatively small strip of compacted ice remained at the beginning of the experiment.

A comparison of historical hydrographic data over the years 1923-2011 with 33 CTD-measurements (Conductivity, Temperature, Depth) conducted during the RV Lance cruise revealed an anomalously northern location of the Polar Front in March 2014 (Dobrynin and Pohlmann, 2015). Significantly warmer (by up to  $3.8^{\circ}\text{C}$ ) and saltier (by up to  $2.49\text{ g/kg}$ ) conditions were observed in 2014 for nine out of ten stations in a point by point comparison with historical stations in 1983 and 1986. The surface salinity was measured covering the Atlantic and Arctic water masses on both sides of the Polar Front: in the Storfjorden Trench (approximately  $35.05\text{ g/kg}$ ) and in the Olga Basin south of Kongsøya (approximately  $34.60\text{ g/kg}$ ). During the main experimental phase between March 16 and March 27 the air temperature at Hopen was about  $5^{\circ}\text{C}$  above the climatological mean. The near-surface air temperatures varied between  $-10^{\circ}\text{C}$  to  $-15^{\circ}\text{C}$  and caused new ice growth in the area of investigation. The anomalous ice retreat together with the subsequent refreezing created the perfect conditions to acquire sea ice thickness validation data over thin ice.

An array of 15 ice drift buoys was deployed from an aircraft before the ship cruise to measure the ice movement. The drift trajectories from the buoys are useful to determine the origin of the ice and help to determine if thickness changes are caused by ice dynamics or ice growth and melting ( Fig. III.2). In addition to 11 Cosmos-Skymed and 8 Radarsat scenes 83 TerraSAR-X images have been acquired in the new experimental 6-beam wide-swath mode

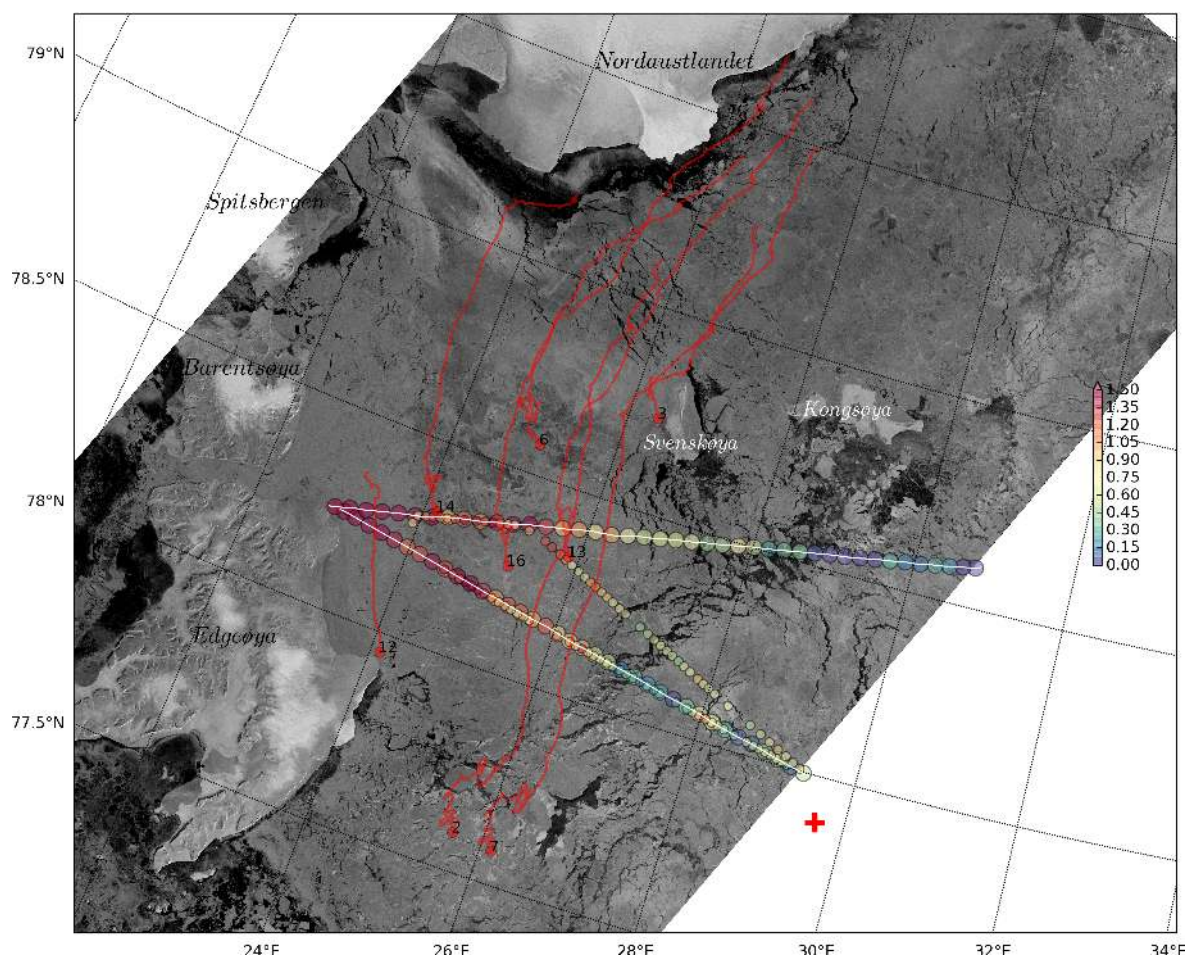


**Figure III.2.:** Sea ice condition during the field experiment on March 24. The TerraSAR-X wide swath frames were taken at 05:36. The positions and trajectories of ice drift buoys are indicated with red circles and lines. Only those buoys are selected that transmitted their positions for the entire period between March 10 and March 24. The color-coded circles show the ice+snow thickness [m] as measured with ALS (60 seconds average) and HEM (50 seconds average). The red cross indicates the position 77.9°N, 29.7°E of RV Lance at 15:00.

to support the interpretation of the field data and to validate ice motion algorithms.

### III.3. Sea ice thickness from electromagnetic induction

Electromagnetic induction (EM) measurements rely on the large contrast in electrical conductivity between sea ice and seawater. An electromagnetic field generated by a transmitter coil induces electrical eddy currents mainly in the seawater below the ice. A second receiver coil measures the secondary field produced by the eddy currents. The ratio of the secondary to the primary field depends on the height of the coils above the sea surface. Ice thickness can be calculated when the distance of the instrument to the ice surface is known (Haas, 1998; Haas et al., 2009).

The distance to the snow or ice surface was measured by an ultrasonic sensor for the Geonics EM31 system installed at the bow of RV Lance and by a Riegl LD90-3 laser altimeter for the EM-Bird carried below the helicopter. The EM-Bird was built by Ferra Dynamics Inc., Ontario, Canada. Henceforth we will use the abbreviations SEM and HEM to distinguish between the shipborne and the helicopter EM systems, respectively.

The SEM was installed below an aluminium boom mounted like a bowsprit to reduce the

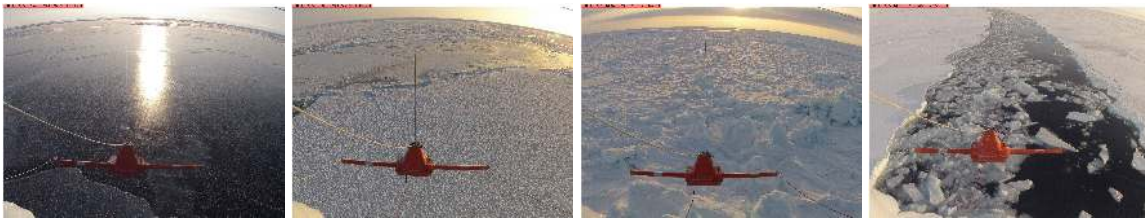


**Figure III.3.:** Example ice conditions and EM thicknesses measured at the bow of RV Lance: a) Dark nilas of 2-4 cm thickness, b) grey white level ice of 17 cm thickness, c) pressure/rubble ice field of 3.4 m thickness, d) navigating through a lead with a mean thickness of 17 cm.

influence of the ship hull and other conductive parts. It was lowered from the boom resulting in a distance to the ship hull of around seven meters with the distance to the water surface between three to four meters (Figs. III.1 and III.3). The time resolution of the SEM was 2 Hz and the ice thickness measurement was complemented with 10 Hz-measurements of surface temperature by a radiation thermometer of type KT19, installed at the bow at the foremost point of the railing and looking downward along an angle of about 30°. With a beam width of 1° the resulting KT19 footprint had a diameter of about 1 m and was within the footprint of the SEM which had a diameter of about 5 m. Two calibrations of the SEM were performed, the first in Longyearbyen on March 14 and a second one within a small patch of open water in the sea ice on March 19. After that the SEM instrument was operated continuously and stable ice thickness results could be retrieved without any further correction. The accuracy and precision of the SEM thickness measurement was about 2 cm as estimated over thin nilas (Fig. III.3) and the signal was remarkably stable - as seen by the accurate detection of zero levels in leads - for the 1800 km track (Fig. III.4). The accuracy decreased in the presence of surface waves which were present in particular during the last southerly sections of the cruise on March 26 and thereafter.

The HEM system is operated at a height of approximately 15 m above the sea ice surface. With a nominal flying speed of 70 knots (36 m/s), the sea ice thickness is measured every 3 to 4 m within a footprint of about 50 m. In total eight HEM flights were performed as summarized in Table III.1. The HEM data processing involves some manual steps to remove the instrument drift during the measurements and to define the zero ice thickness level. To avoid unrealistic data the processing routine automatically removes data outside minimum & maximum thresholds in laser height, and data that coincide with a change in heading (to avoid roll events on change of direction). Other small gaps in the data occur due to GPS dropout and to the laser failing over open water. The nominal uncertainty for a single ice thickness measurement is 10 cm for level ice while larger errors can occur for ridges (Haas et al., 2009). Both the SEM and the HEM measure the thickness of sea ice plus snow. We note that the helicopter usually avoided flying over thin ice and open water for safety reasons while the ship mainly navigated through leads (Fig. III.3).

### III.4. Sea ice thickness from airborne laser scanner and L-band radiometer

One primary goal of the airborne field campaign was to obtain high resolution, polarized L-Band brightness temperatures at different incident angles together with independent sea ice thickness measurements for the validation of retrieval algorithms. The two primary independent data sources are the EM-bird flown from the helicopter and the ALS aboard the Polar 5.

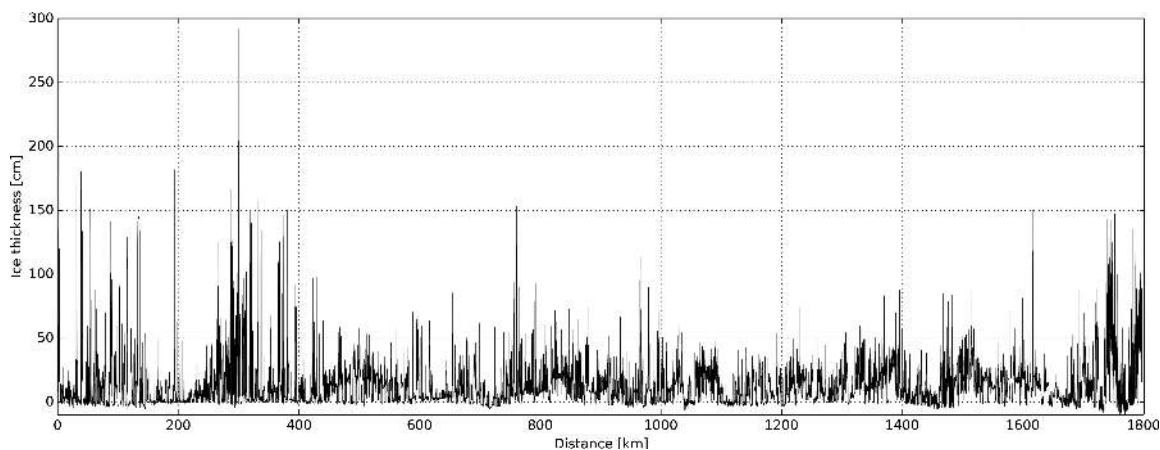


**Figure III.4.:** Sea ice thickness profile measured with the SEM at the bow of RV Lance from March 18 to 27, 2014. The location of the 1800 km long track is shown in Fig. III.6. The thickness measurements were spatially averaged over 25 meter distances according to the GPS position of RV Lance.

**Table III.1.:** Primary thickness validation datasets.

Platform	Sensors	Periods	Comments
RV Lance	SEM, KT19	18. 15:19 - 27. 11:09	Fig. III.4
Polar 5	ALS, EMIRAD-2	24. 9:15 - 12:52	Fig. III.2 and III.5
		26. 8:47 - 12:22	
		26. 14:27 - 16:27	CryoSat underflight
Helicopter	HEM	19. 14:50 - 15:42	CryoSat underflight
		20. 08:52 - 11:03	
		20. 14:23 - 16:28	
		22. 08:32 - 10:52	CryoSat underflight
		22. 13:51 - 15:55	
		23. 12:45 - 13:56	
		24. 10:39 - 13:16	
26. 11:06 - 13:17	Fig. III.2 and III.5 With Polar-5		

In this campaign only measurements from the latter instrument are truly co-incident and co-located with the L-Band radiometer EMIRAD-2. The combination of ALS and EMIRAD-2 data is thus suitable to assess the performance of the instruments and to verify the retrieval of thickness from 1.4 GHz brightness temperatures at high spatial resolution. Comparisons between ALS and SMOS ice thickness will be discussed in the next section.

The EMIRAD-2 L-band radiometer developed by DTU-Space is a fully polarimetric system with advanced RFI detection features (Sobjaerg et al., 2013). Two Potter horn antennas - one nadir pointing, one side looking at 45° incidence angle measure the radiation from the surface with a footprint of approximately 250 m at 300 m flight altitude. The receiver has a sensitivity of 0.1 K for 1 s integration time. Internal calibration every 8 to 16 minutes maintains a stability of better than 0.1 K. External calibration with liquid Nitrogen gives estimates of the uncertainty associated with the cables connecting the antenna to the receiver below 0.5 K of equivalent noise temperature. During all flight operations navigation data are collected and used to transform the polarimetric brightness temperature into the Earth reference frame (Hendricks et al., 2014).

The EMIRAD-2 data have been screened by evaluating kurtosis, polarimetric, and brightness temperature anomalies and revealed up to 30% radio frequency interference (RFI) contamination. When subtracting the mean value of the RFI-flagged data from the mean value of the full data a difference of typically a few K is present for side looking horn and typically 10 K for the nadir looking horn. Especially for the last flight on March 26, a difference of 25 K between raw and cleaned data is observed for the nadir looking horn. Data analysis further revealed a 20 K offset relative to the nadir vertical channel caused by a continuous wave signal from the camera that was mounted at the airplane to obtain visual images. This contamination could not be detected by the RFI filters but the analysis concludes a purely additive characteristic and allowed a bias correction (Hendricks et al., 2014). In the following we use an RFI-cleaned and bias-corrected data set which was validated using aircraft wing wags and nose wags over open ocean (Hendricks et al., 2014).

A Riegl VQ-580 laser scanner (ALS) used on the Polar 5 operates in near infrared with an accuracy and precision of 25 mm over snow and ice. The linear across-track scans are performed in the range of 30° to -30° with a pulse repetition frequency of 50 kHz leading to a horizontal sampling resolution of 30 cm at 60 meter altitude. A calibration of the instrument mounting position and orientation in the aircraft reference frame was done using a fixed ground target, namely the airport buildings in Longyearbyen. The determination of the ellipsoidal (WGS84) surface heights from the laser range data and the aircraft altitude and instrument mounting position and orientation was performed according to Helm et al. (2006). Finally, the surface height was referenced to the local sea level by manual classification of tie points in leads.

The ALS freeboard data are resampled to one second and to one minute by taking the arithmetic mean value. To estimate the ice thickness from the freeboard one has to make some assumptions about the density of ice and snow and the snow thickness. While the snow depth on the sea ice was not measured in situ, continuous visual observations from Lance were done. From these observations as well as from imagery from a camera at the bow of the ship, the snow cover of the ice near the ship can be estimated to be a few centimeters whenever the ship was in thin ice (when the thickness measured by the SEM is between about 0 and 20 cm). Only very thin ice like freshly frozen leads was snow-free. Snow depths near 10 cm were only observed occasionally when the ship was navigating through thicker floes or ridges (SEM reading about 1 m). In addition, snow depth on the sea ice was retrieved from AMSR2 (UB product, based on the algorithm by Markus and Cavalieri (2013)) with a

resolution of about 15 km. Only in the region Northeast of Egdeøya (where ice thickness in Fig. 7 exceeds 1 meter), the retrieved snow depth reaches 20 cm while in all other areas, the retrieved snow depths are generally between 0 and 5 cm throughout the cruise. Therefore, it is justified to use a simple parameterization  $h_s = 0.1 \cdot h_i$ , with the snow thickness  $h_s$  and ice thickness  $h_i$  (Yu and Rothrock, 1996; Maekynen et al., 2013).

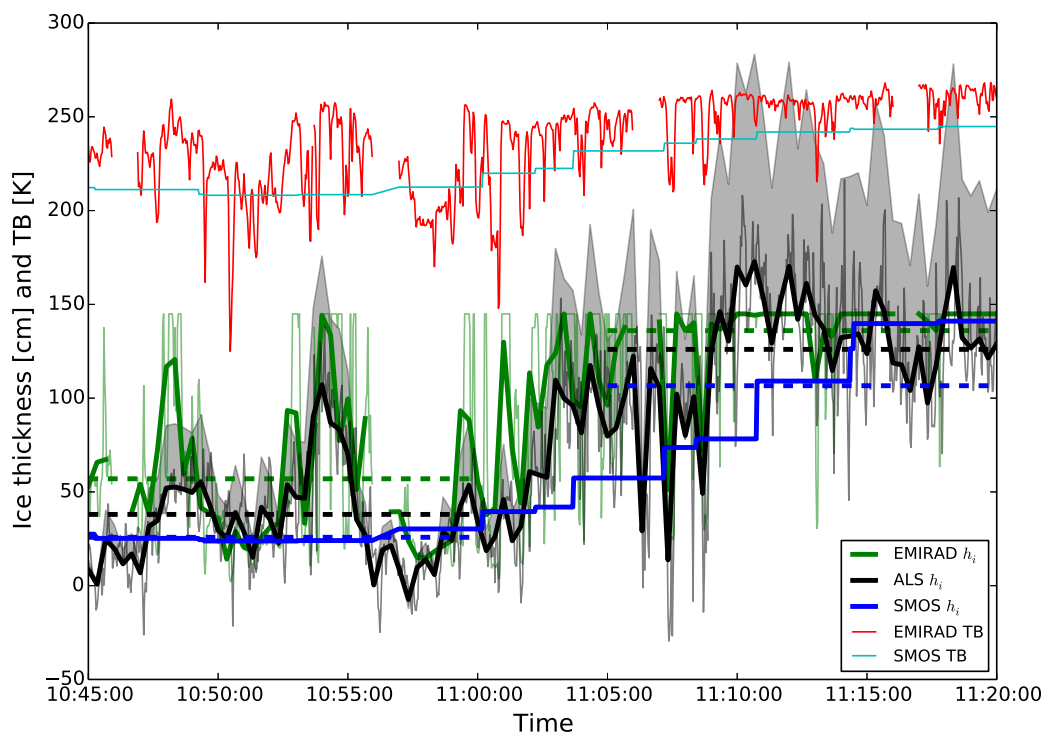
We assume a snow density of  $300 \text{ kg/m}^3$  (Warren et al., 1999), a typical density of first year ice as  $917 \text{ kg/m}^3$  (Ricker et al., 2014), and seawater as  $1027 \text{ kg/m}^3$ . The resulting factor of 5.6 is used to estimate the ice thickness from the ALS freeboard measurement. The assumption of a snow-free ice surface results in a conversion factor of about 9. The difference of both calculations can be seen as a first rough error estimate of the ALS thickness retrieval: with the assumption of a snow free ice surface we obtain a maximum observed sea ice thickness of about 4 m (one minute average). It reduces to about 2 m with the assumption of the snow thickness as 10% of the ice thickness.

Figure III.2 shows the tracks flown on 24 March 2014. Figure III.5 depicts the east-west profile from the position  $78.0^\circ\text{N}$ ,  $29.4^\circ\text{E}$  to  $78.25^\circ\text{N}$ ,  $23.0^\circ\text{E}$  (155 km length). This case includes a strong gradient from thin newly-formed ice to thick deformed ice. The data of the other Polar 5 tracks on March 24 look very similar and are therefore not shown. The mean thickness derived from ALS for the track shown in Fig. III.5 is 0.8 m and 1.3 m for the assumption of  $h_s = 0.1 \cdot h_i$  and for the snow-free surface, respectively. The corresponding ice thickness retrieved from EMIRAD-2 using the operational SMOS algorithm described in Tian-Kunze et al. (2014) is 1 m. The correlation coefficient between ALS and EMIRAD-2 ice thickness is  $R \approx 0.9$  and the RMSD is 0.3 m for the overall track ( $N = 105$  data points).

When only the first and last 15 minutes are considered (thus omitting the transition zone between thin and thick ice) slightly reduced correlations of  $R \approx 0.7$  ( $N = 45$ ) are obtained while the RMSD remains similar. The mean values of both 15 minute sections shown in Fig. III.5 demonstrate that the thin and thick ice regimes can be well distinguished. The EMIRAD-2 thickness is greater than the ALS thickness estimate for the snow-covered and lower compared to the snow-free assumption. The brightness temperatures from SMOS are about 10 K lower compared to the EMIRAD-2 measurements but the gradient is well captured with however much coarser resolution. The differences can be explained with the coarse resolution of SMOS  $100 \times 100$  bigger than the EMIRAD-2 footprint. The footprints of the individual SMOS measurements that are averaged into the 12.5 km grid have resolutions of about 35-40 km. EMIRAD-2 samples only a small fraction and is not representative for the SMOS measurement area. Moreover, we can not rule out problems with the bias correction and problems due to self-reflection of the aircraft. Special care was taken to avoid potential sun glint but some uncertainty still remains. A comparison of low-level and high-level flights in opposite directions showed no systematic differences in the nadir brightness temperatures. The reason for the 10 K bias remains therefore speculative and restrains the use of the EMIRAD-2 nadir brightness temperatures in terms of absolute values.

### III.5. SMOS ice thickness retrievals

For the following comparison we use two SMOS sea ice products of the University of Hamburg (UH) and University of Bremen (UB). Both products have been obtained from the respective websites, and no modifications have been applied. Thus, they represent the retrieval algorithms as described in Tian-Kunze et al. (2014) and Huntemann et al. (2014). The sea ice thickness products were derived from SMOS data based on the baseline processor version 505 operational in March 2014.



**Figure III.5.:** Sea ice thickness derived from ALS surface elevation and EMIRAD-2 brightness temperature (TB) on March 24, 2014. The thin and thick lines represent 2s and 20s averages, respectively. The TB is averaged along track and the freeboard is averaged along and across-track for ALS. EMIRAD-2 measured TB near nadir while the SMOS TB is the average between nadir and  $40^\circ$  taken from the closest grid cells. The values for the ice thickness from SMOS were taken from the UH product and the same algorithm was used to derive the ice thickness from EMIRAD-2 TB. The thick black line indicates the sea ice thickness derived with the assumption of  $h_s = 0.1 \cdot h_i$  while the upper limit of the grey shaded area is calculated without snow. The dashed lines indicate the mean values when only the first and last 15 minutes are considered.

We calculate the temporal average of all SEM, HEM, and ALS measurements over the period of March 18 to 27 in order to achieve sufficient spatial coverage. We acknowledge that the UH SMOS thickness is already corrected for a statistical thickness distribution and should therefore be compared to the mean and not the modal ice thickness. The data are spatially averaged using the arithmetic mean value of all measurements within grid cells of 12.5 km resolution (same as the UH SMOS product grids) without any weighting. The resulting average gridded mean is first calculated separately for the different sensors and in a second step combined in a single thickness field which is taken for validation of the satellite data. We thereby assume that the average compensates to some extent preferential sampling biases inherent in the different data sets: the shipborne measurements probably underestimate the ice thickness due to local navigation through leads and the limited ice-breaking capability up to about 0.5 m while the helicopter was not flying over open water and thin ice due to safety reasons. The SMOS thicknesses are temporally averaged over a slightly shortened period as the ground data. March 18 and 27 are not considered because of the sparse data coverage with only SEM data on these two days. An analysis performed for the single days of SMOS data (not shown) yields similar statistical parameters not significantly different compared to those numbers discussed in the following with the only exception of March 24.

The spatial distribution of the ground data together with the SMOS ice thickness (UH product) is shown in Fig. III.6. It should be noted that the UB thickness product (not shown) resembles the spatial patterns but resolves ice thickness only up to a maximum of 0.5 m (thus, a retrieved thickness of 0.5 m means thickness  $\geq 0.5$  m). The statistical parameters of the comparisons are summarized in table III.2.

The overall linear correlation coefficient between the combined ground data and the two different SMOS thickness products is  $R = 0.75$ . The day with the highest in-situ gradient, March 24 with tracks including the patch of thick deformed ice, shows a higher correlation coefficient of about  $R \approx 0.9$  (Fig. III.7). Other days with a smaller gradient show smaller correlations.

Both SMOS data products underestimate the thickness on average by about 50-60%. However, the UH product performs better in comparison with the UB product with a reduced mean difference and RMSD. When the SMOS products are compared only against the SEM data they both agree within 1 cm with an observed mean thickness of 17 cm along the ship track of Lance. However, Lance is not an ice-breaker and its ability to navigate through the ice is limited to relatively thin ice up to about half a meter level ice thickness. Pressure ridges appear on a very local scale and frequently resulted in an interruption of the route validation. The validation is further complicated because of the manual optimization by the helmsmen who preferably navigated through open leads (Fig. III.3d). The very local navigation and the different location of the thickness transects is a likely cause for the mean difference between the (thicker) airborne ALS and HEM data in comparison to the (thinner) HEM measurements. The SEM measurements are neither correlated to HEM or ALS nor to SMOS thickness data. However, the SEM instrument provided accurate thickness measurements which were in very good agreement with visual estimates of the level ice thickness.

Figure III.7 shows the thickness distribution and a scatter plot for the case of March 24. The combined airborne (ALS and HEM) data reveal a bi-modal distribution in the thickness histogram. SMOS and airborne data agree well over the thin ice with a modal thickness of about 20 cm. The thicker deformed ice is substantially underestimated in the SMOS product resulting in a mean thickness difference of about 30%. The correlation  $R = 0.88$  between SMOS and the airborne data is similar to the correlation between EMIRAD-2 and ALS

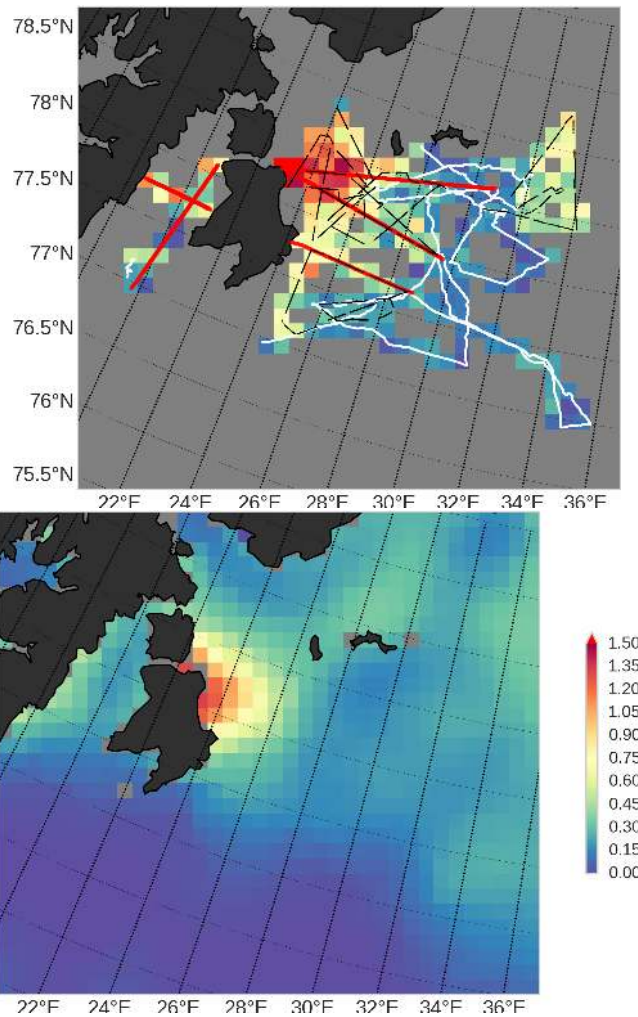


**Figure III.6.:** Ground (left) and SMOS sea ice thickness (right) color-coded in meter. The ground data consists of SEM (white) and HEM (black) and ALS (red) measurements block averaged with 12.5 km grid resolution. The SMOS map represents a temporal average over the period March 19 to 26.

shown in the previous section.

### III.6. Conclusion

A comprehensive validation field campaign in the Barents Sea was conducted in March 2014. An anomalously strong ice retreat together with the subsequent refreezing was perfectly suited to obtain sea ice thickness validation data over relatively thin ice in the seasonal ice zone. Measurements from the ice strengthened research vessel Lance, a helicopter based on Lance, and the research aircraft Polar 5 operated from Svalbard airport form an extensive and unique sea ice thickness validation data set. Furthermore, high resolution brightness temperatures were measured with the EMIRAD-2 L-band radiometer aboard the Polar 5. This ground data was used for a comparison to SMOS-based estimates of the sea ice thickness.

The overall main pattern of the spatial thickness distribution is well captured in two different SMOS sea ice products from the Universities of Hamburg (UH) and Bremen (UB). The origin of a patch of thick deformed ice at the east coast of Edgeøya was determined using trajectories of ice drift buoys that were deployed before the field campaign. The upper value of

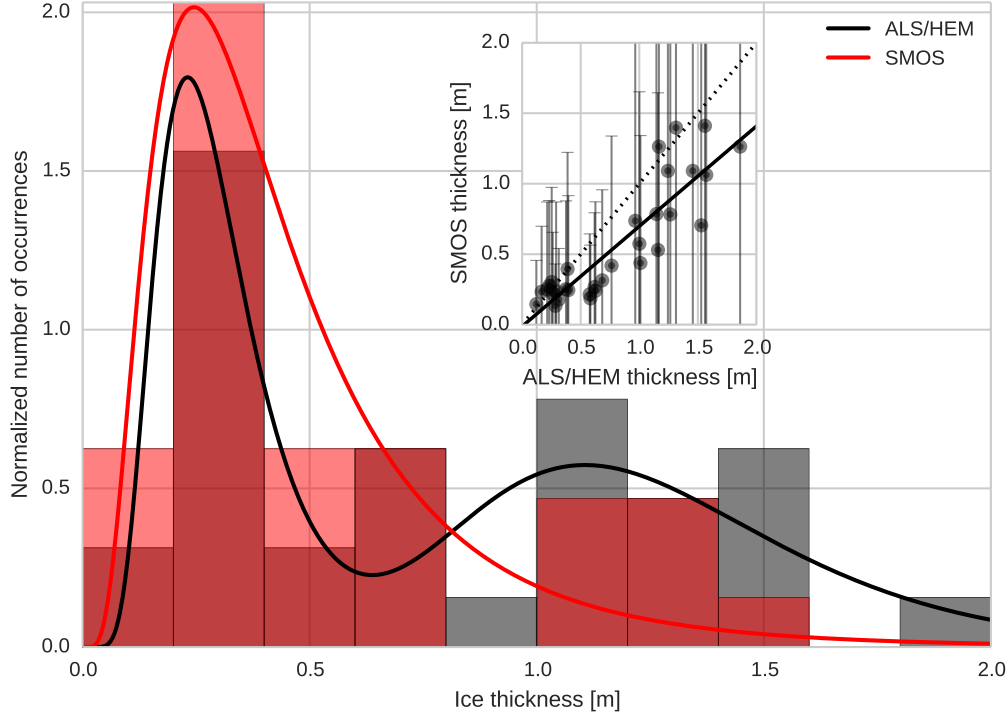


**Figure III.7.:** Sea ice thickness distributions and scatter plot for the case of March 24. The histograms and probability distribution functions (PDF) were derived from the gridded HEM and ALS validation data. The corresponding flight tracks are shown in Fig III.2. The SMOS histogram and the scatter plot was derived from the corresponding pixels of the ground data (number of pixels  $N = 32$ ). The error bars in the scatter plot show the uncertainty as provided with the UH product. The solid lines are lognormal PDFs. A linear regression (inset) yields  $Y = 0.71 * X - 0.01$  [m] with a correlation  $R = 0.88$ . The mean and standard deviation are  $\mu_G \pm \sigma_G = 0.79 \pm 0.5$  m for the airborne ground data (ALS and HEM average) and  $\mu_S \pm \sigma_S = 0.55 \pm 0.4$  m for SMOS. The mean and RMS difference are 0.24 m and 0.34 m, respectively.

**Table III.2.:** Statistical comparison between SMOS and ground sea ice thickness for different subsets (selected pixels with 12.5 km resolution) averaged over the entire spatial and temporal domain. The subsets are selected according to different data sources and conditions. The ground (index G) and SMOS (index S) thickness mean and standard deviation for different subsets are given in the second and third column, respectively. Measurements and SMOS data have been averaged as described in section III.4. Correlation  $R$ , mean difference (MD), and root mean square difference (RMSD) have been calculated on pixel level. The number of pixel data pairs is given in the fourth column. The condition based on the UB product ( $h_{UB} < 0.5$  m) results in  $N = 213$  selected pixels with the UB SMOS ice thickness below half a meter. This subset of pixels is also for the UH product to derive a consistent comparison. The two first rows refer to the comparison of the UH and UB SMOS product for the entire averaged ground data (SEM&HEM&ALS), respectively. All units are in [cm] except for correlations and number of pixels  $N$ .

Data	$\mu_G \pm \sigma_G$	$\mu_S \pm \sigma_S$	N	$R$	MD	RMSD
SMOS UH	44±36	26±19	229	0.75	-18	31
$h_{UB} < 0.5$ m	39±30	22±10	213	0.65	-15	29
SEM	17±13	18±7	121	0.12	-1	14
HEM&ALS	65±33	31±21	149	0.72	-33	41
SMOS UB	44±36	22±11	229	0.76	-22	36
$h_{UB} < 0.5$ m	39±30	19±8	213	0.66	-20	32
SEM	17±13	17±5	121	0.10	0	14
HEM&ALS	65±33	25±12	149	0.70	-40	48

the thickness range was set by this area of deformed ice with thickness between 1-3 meters. The lower range was determined by an area of newly formed sea ice with a mean thickness of 17 cm that was extensively sampled by the shipborne EM on Lance. The thickness gradient between the new thin ice and the thick ice is well represented by the airborne sensors as well as with the SMOS products. The SMOS retrieval substantially underestimates the thickness of the deformed thick ice but agrees well with the shipborne measurements in the extensive areas of newly grown young sea ice.

The UB SMOS product provides ice thickness only up to a maximum of 0.5 m while the UH product resolves thicknesses up to about 1.5 m. Sea ice thickness derived from high resolution EMIRAD-2 data using the UH SMOS retrieval algorithm mostly agrees with the thickness derived from the airborne laser scanner within the range of uncertainties and shows correlations up to 1.5 m. A statistical bias correction had to be applied to the EMIRAD-2 nadir data because of contamination with radio frequency interference (RFI) from a camera. Another large uncertainty is caused by the insufficient knowledge about the snow thickness. A new snow radar system aboard the Polar 5 did not perform as expected and the data could not be used for the analysis. We recommend further validation campaigns with an improved snow radar to close this gap of knowledge.

## IV CS2SMOS: A WEEKLY ARCTIC SEA-ICE THICKNESS DATA

*extracted from (Ricker et al., 2017b)*

### IV.1. Introduction

The thickness of the sea ice is difficult to access from space than the ice area. However, recent satellite altimeter missions such as ICESat or CryoSat-2 (CS2) demonstrated the capability to provide reliable Arctic sea-ice thickness and volume estimates (Kwok et al., 2009; Laxon et al., 2013). They are used to measure the freeboard, the height of the ice or snow surface above the water level, which can be converted into sea-ice thickness assuming hydrostatic equilibrium. The current CS2 mission was launched in 2010 and is primarily designed to measure the thickness of the perennial ice cover, but lacks the sensitivity for thin ice regimes (Wingham et al., 2006). On the other hand, SMOS mission, also launched in 2010, provides surface emissivity observations at microwave frequencies (L-band), which are sensitive to the sea-ice thickness, but restricted to thin ice regimes, in particular during the freeze-up (Kaleschke et al., 2012).

Kaleschke et al. (2015) drew attention to the complementary nature of the relative uncertainties of CS2 and SMOS ice thickness retrievals. Figure IV.1 illustrates maps and the relative uncertainties of CS2 and SMOS monthly means from November 2015 and March 2016. While the SMOS relative uncertainties are lowest for thin ice ( $< 1$  m), CS2 relative thickness uncertainties are smaller over thick ice and rise asymptotic towards thickness values  $< 1$  m. This is due to the fact that CS2 thickness estimates over thin ice rely on small surface elevations above the sea level but experience the same or higher magnitude of uncertainties as over thick ice (Ricker et al., 2014). We acknowledge that the CS2 uncertainties represent statistical uncertainties only. Systematic errors such as associated with the usage of a snow climatology or due to snow-volume scattering may alter the uncertainty estimate (Ricker et al., 2014, 2015). Moreover, due to the different orbital inclinations, the spatial coverage of the two data sets is complementary. Figure IV.2 shows weekly means of CS2 and SMOS for November 2015 and March 2016. While valid SMOS ice thickness estimates are found mostly in the marginal ice zones, the CS2 ice thickness retrieval covers major parts of the Arctic multiyear ice (MYI). In November, during the freeze-up, the SMOS retrieval covers major parts of the Beaufort Sea, Chuckchi Sea, and East Siberian Sea. Towards spring, due to advancing ice growth, the SMOS retrieval domain retreats southwards, covering major parts of the Bering Sea and the Sea of Okhotsk. Figure IV.3 illustrates the number of valid grid cells of the weekly means as shown in Figure IV.2. The number of grid cells with co-located SMOS and CS2 estimates is less than 2000, while the number of grid cells that contain thickness estimates from CS2 and SMOS exclusively is about 5000 for each sensor, highlighting the complementary coverage.

The spatial and interannual variability of sea-ice thickness is driven by dynamics and thermodynamics (Zhang et al., 2000; Kwok and Cunningham, 2016). For an accurate description of the Arctic sea-ice thickness distribution, it is necessary that thick and deformed ice as well

as thin ice regimes are represented adequately. Moreover, particularly the forming of new thin ice during the freeze-up characterizes a large area of the ice cover in autumn. In order to detect changes and interannual variabilities in such areas, accurate thin ice thickness estimates with high temporal and spatial resolution are required.

Wang et al. (2016) evaluate six different sea-ice thickness products, including SMOS and CS2, and find that all satellite products as well as the Pan-Arctic Ice-Ocean Modeling and Assimilation System (PIOMAS) overestimate the thickness over thin ice compared to the airborne retrieval by NASA's Operation IceBridge. The smallest bias (0.26 m) over thin ice has been found using the SMOS product.

Considering the depicted complementarity of CS2 and SMOS retrievals and the need for a better representation of thin ice regimes in global-scale sea-ice thickness products, the goal of this project is to provide a data fusion product of CS2 and SMOS sea-ice thickness retrievals, which has the capability to complete Arctic sea-ice thickness distributions over the entire thickness range. Here, we describe and test a method to merge both data sets on a suitable spatial and temporal scale. Moreover, airborne validation data are used to evaluate the benefit of the merged product (CS2SMOS) compared to the individual CS2 and SMOS products.

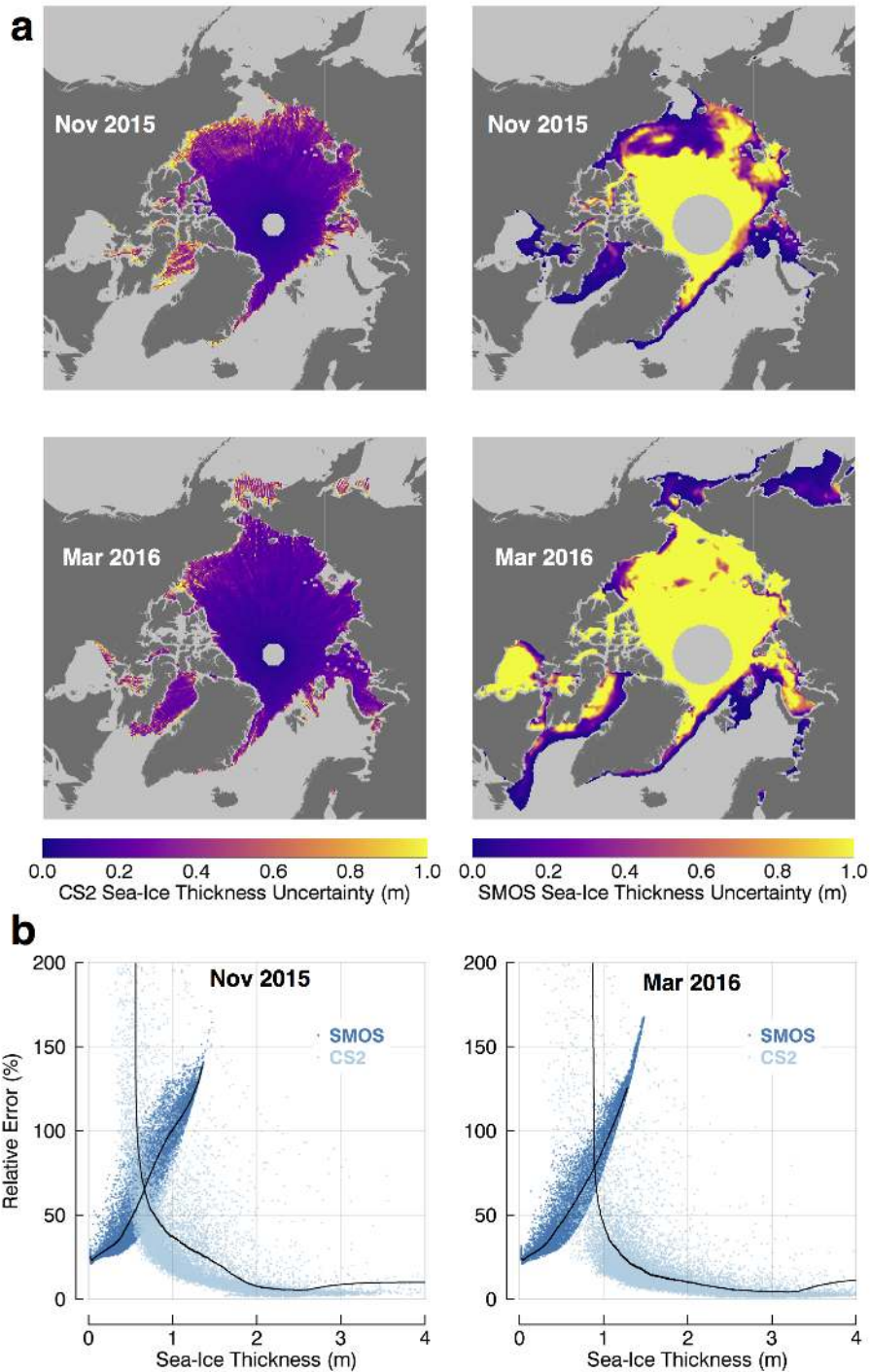


**Figure IV.1.:** a) Monthly sea-ice thickness uncertainty maps of the CryoSat-2 and SMOS retrieval from November 2015 and March 2016. The SMOS thickness uncertainty is cropped by a 1 m maximum filter. b) Relative uncertainties from November 2015 and March 2016. A running mean is represented by black solid lines.

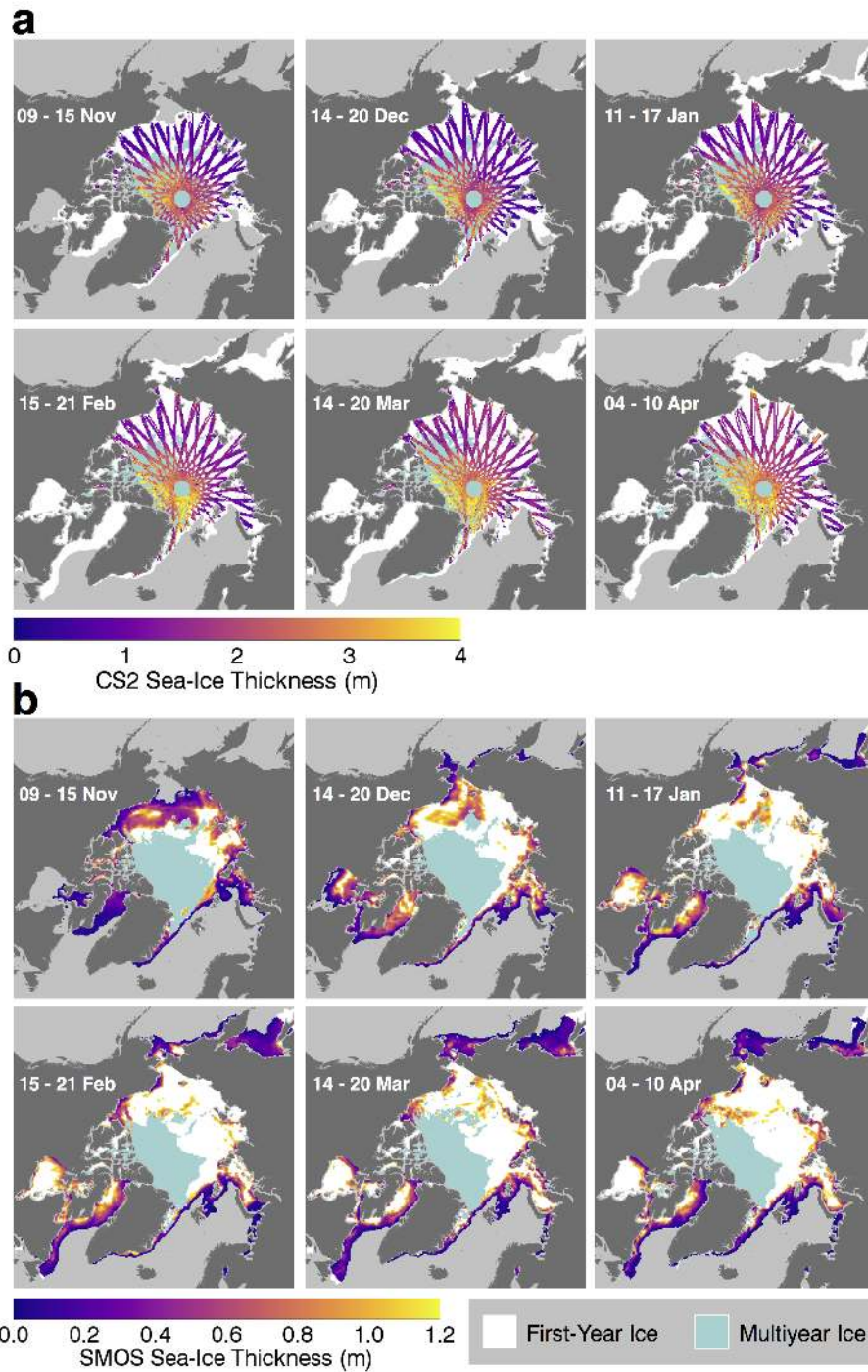


**Figure IV.2.:** Weekly input data grids for November 2015 and March 2016. a) Weekly CryoSat-2 retrieval. b) Weekly means of daily SMOS ice thickness retrievals, cropped by a 1 m maximum SMOS thickness uncertainty and a multiyear ice filter. The background fields indicate first-year and multiyear ice coverage. Note the complementary coverage in a) and b).

## IV.2. Data

We use the AWI CS2 product (processor version 1.2) (Ricker et al., 2014; Hendricks et al., 2016) and the SMOS sea-ice thickness retrieval from the University of Hamburg (processor version 3.1) (Tian-Kunze et al., 2014; Kaleschke et al., 2016) as input ice thickness data. As auxiliary data we use ice concentration and ice type provided by the Ocean and Sea Ice Satellite Application Facility (OSI SAF).

In the first step we use CS2 SIRAL Level-1b orbit data files that are provided by ESA. They contain geolocation information and time of the Doppler beam formed radar echoes. SIRAL is operated in two different modes over sea ice. The Synthetic Aperture Radar (SAR) mode covers major parts of the ice covered area, while the Interferometric Mode (SIN) is applied mostly in coastal areas. Both modes serve for retrieving ice thickness, but must be processed separately.

The radar echoes (waveforms) are processed for each CS2 orbit according to (Ricker et al., 2014; Hendricks et al., 2016). A 50% threshold-first-maximum retracker (Ricker et al., 2014; Helm et al., 2014) is used to obtain ellipsoidal surface elevations ( $L$ ), which are corrected for geophysical perturbations as tides and atmospheric effects (Ricker et al., 2016). Main undulations due to the geoid and the mean sea-surface height (MSS) are removed by subtracting the Danish Technical University version 2015 (DTU15) MSS height (Andersen et al., 2015):

$$L_{MSS} = L - MSS. \quad (IV.1)$$

The shape of the waveform is determined by the characteristics of the surface. Specifically, radar returns from surfaces that contain leads, which are openings in the ice pack, appear as specular echoes and can be separated from echoes that contain reflections from sea ice only. The lead elevations are used to interpolate the instantaneous sea-surface height anomaly (SSHA). Finally, the SSHA is subtracted from the ice surface elevations to retrieve the freeboard ( $Fb$ ):

$$Fb = L_{MSS} - SSHA. \quad (IV.2)$$

$Fb$  can be converted into sea-ice thickness ( $Z$ ) by assuming hydrostatic equilibrium (Laxon et al., 2003):

$$Z_{cs2} = Fb \cdot \frac{\rho_W}{\rho_W - \rho_I} + S \cdot \frac{\rho_S}{\rho_W - \rho_I}, \quad (IV.3)$$

where  $S$  is the snow depth and  $\rho_S$ ,  $\rho_I$ , and  $\rho_W$  the densities of snow sea ice and sea water.  $S$  and  $\rho_S$  are represented by the modified Warren snow climatology (W99) (Warren et al., 1999).  $S$  is reduced by 50 % over FYI to accommodate the recent change towards a seasonal Arctic ice cover (Kurtz and Farrell, 2011). FYI and MYI are separated by adopting the daily OSI SAF ice type product (Eastwood, 2012). We exclude CS2 measurements over Hudson Bay and Baffin Bay as they are not located within the domain of the W99 climatology, which is constrained by in-situ measurements from Soviet drifting stations and airborne landings from the 1950's to 1990 (Warren et al., 1999). We use ice densities of 916.7 kg/m<sup>3</sup> and 882.0 kg/m<sup>3</sup> for FYI and MYI (Alexandrov et al., 2010), and 1024 kg/m<sup>3</sup> for the sea water density.  $Z$  is calculated for each individual CS2 orbit. All orbit retrievals are averaged on a 25 km EASE2 grid (Brodzik et al., 2012) within one calendar week (Figure IV.2a).

The daily SMOS product (details of the SMOS retrieval can be found in Part II in this report and SMOS+Sea Ice ATBD UHH) are averaged weekly and are projected on an EASE2 25 km grid to be in line with the CS2 retrieval. Here, we only allow SMOS thickness values with a corresponding uncertainty < 1m which corresponds to a maximum theoretical thick-

ness of about 1.1 m. Furthermore we expect strong biases for the SMOS ice thickness in thicker MYI regimes. Therefore we apply the OSI SAF ice type product (Eastwood, 2012) and discard any SMOS grid cells that are indicated as MYI. The weekly composites are shown in Figure IV.2b.

We use the OSI SAF sea-ice concentration (OSI-401-b) and type (OSI-403-b) products (Eastwood, 2012) in order to identify grid cells that contain  $\geq 15\%$  sea ice and whether it is first-year (FYI) or multiyear (MYI) sea ice. The products are delivered daily, projected on a 10 km polar stereographic grid. To combine these data with the CS2 and SMOS thickness grids, we calculate weekly means that are projected on a EASE2 25 km grid (Brodzik et al., 2012) to be in line with the thickness retrievals. The original ice type product contains grid cells that are flagged as "ambiguous". We apply an inverse-distance interpolation on those grid cells to obtain FYI or MYI flags for all ice-covered grid cells, because it is needed for further processing steps.

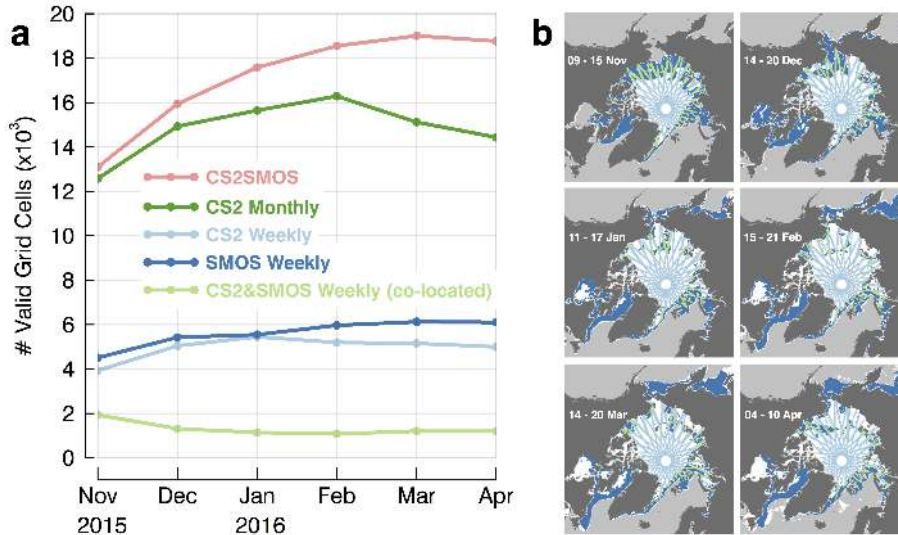
### IV.3. Methods

We use an optimal interpolation scheme (OI) similar to Boehme et al. (2008) and McIntosh (1990) that enables the merging of datasets from diverse sources on a predefined, so-called analysis grid. The data are weighted differently based on known uncertainties of the individual products and modeled spatial covariances. OI minimizes the total error of observations and provides ideal weighting for the observations at each grid cell. In this section we present the processing methods, on which our OI approach is based. Figure IV.4 shows the processing scheme, which will be described in more detail in the following.

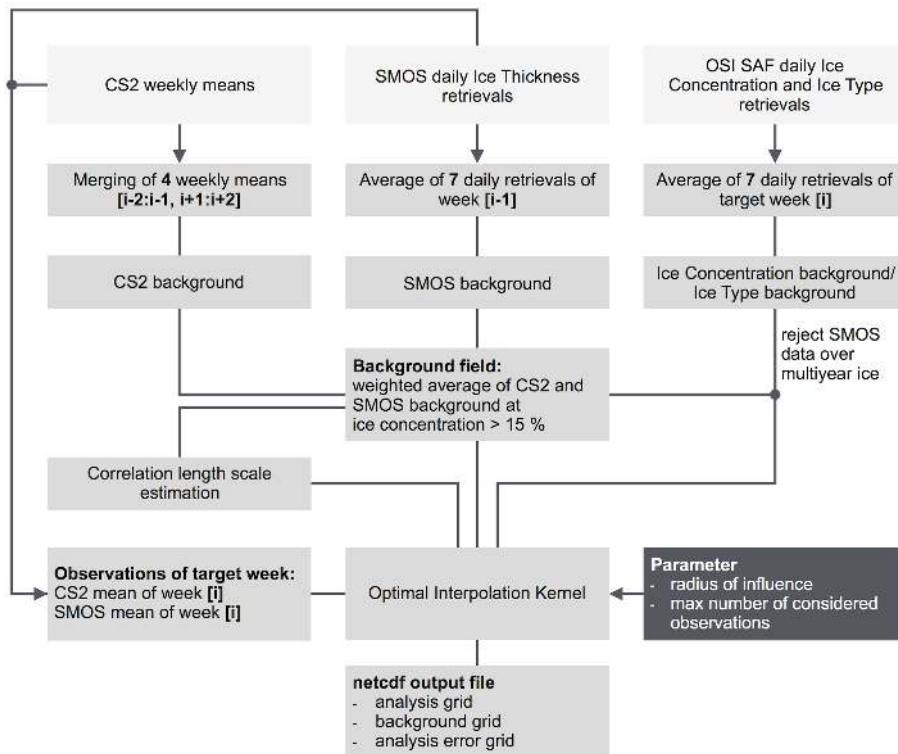
The OI scheme is used to get an objective estimate of values at observed or unobserved locations. The basic equation is:

$$Z_a = Z_b + K[Z_o - H(Z_b)], \quad (\text{IV.4})$$

where the vector  $Z_a$  is the analysis field that represents the merged CS2SMOS ice thickness retrieval which we aim for.  $Z_b$  is the background field vector and  $Z_o$  the vector that contains all SMOS and CS2 observations. As observations we here define already gridded thickness estimates, based on weekly averages as shown in Figure IV.2. This approach reduces statistical uncertainties and provides equally distributed observations, which improves the performance of the OI. In addition, it is reasonable to reduce the number of observations, otherwise computing can become expensive. We assume that the observations are static, which is a simplification, because the satellite thickness estimates are temporally incoherent due to ice deformation and motion. Therefore, we neglect any temporal correlations.  $H$  is an operator that transforms the background field into the observation space. To be more specific, this is realized by an inverse distance interpolation method. We aim to retrieve weekly analysis fields, based on calendar weeks that reach from Monday to Sunday. Melting does not allow the retrieval of summer sea-ice thickness estimates from CS2 or SMOS. Hence, the CS2SMOS product is limited to the period from October/November to April.



**Figure IV.3.:** a) Spatial coverage in number of valid 25 km grid cells from November 2015 to April 2016. Here, 'valid' indicates grid cells that contain a valid thickness estimate. b) Spatial distribution of valid weekly thickness retrievals by CS2 (light blue) and SMOS (dark blue) during a week in November 2015. Co-located grid cells are colored light green. The white background field indicates the reference ice extent.



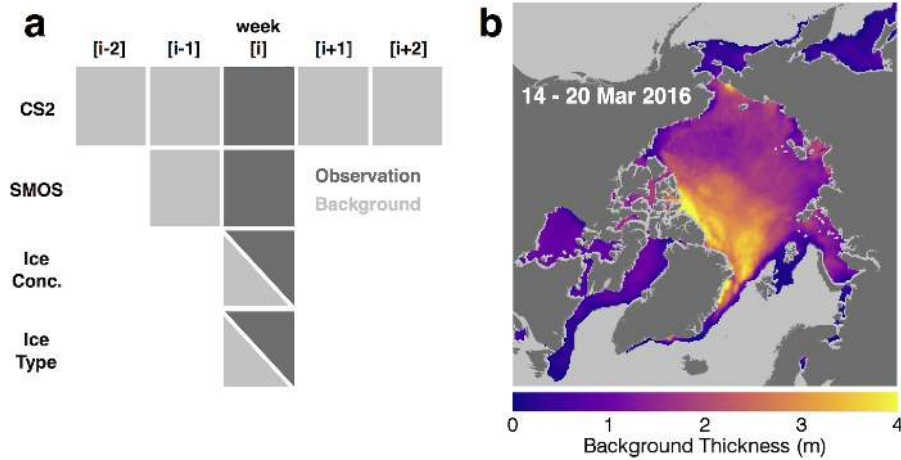


**Figure IV.5.:** a) The scheme illustrates how the background field and the observation field are generated from weekly input grids. [i] represents the target week. b) Interpolated and low-pass filtered background field as it is used for the optimal interpolation.

### IV.3.1. The Background Field

The weekly CS2 ice thickness products leave gaps due to the incomplete orbital coverage (Figure IV.2a). Therefore, we use a composite of weekly retrievals, ranging from 2 weeks behind to two weeks ahead, to get a nearly complete background field coverage for the Central Arctic at a certain target week (Figure IV.5). In order to ensure an independent background field, the target week is not included. For the same reason, we use a SMOS weekly mean from the previous week. The initial background field is represented by a weighted average:

$$\bar{Z} = \frac{Z_{cs2}/\sigma_{cs2}^2 + Z_{smos}/\sigma_{smos}^2}{1/\sigma_{cs2}^2 + 1/\sigma_{smos}^2}. \quad (IV.5)$$

$Z$  is the sea-ice thickness and  $\sigma$  the statistical uncertainty of the individual products. Since we use CS2 and SMOS retrievals for the background field beyond the target week and because the SMOS composite contains artifacts of thin ice (< 10 cm) in coastal regions, we additionally use a weekly mean of the daily OSI SAF ice concentration product to determine the ice coverage during the target week. Here, we apply a threshold of 15 % and only grid cells that exceed this value will be considered as ice covered, which corresponds to the ice extent products provided by OSI SAF and the National Snow and Ice Data Center (NSIDC). Gaps in the weighted average, derived from Eq. IV.5, are interpolated by using a nearest neighbor scheme. In order to reduce noise, the background field is low-pass filtered before it is applied in the optimal interpolation algorithm (Figure IV.5b).

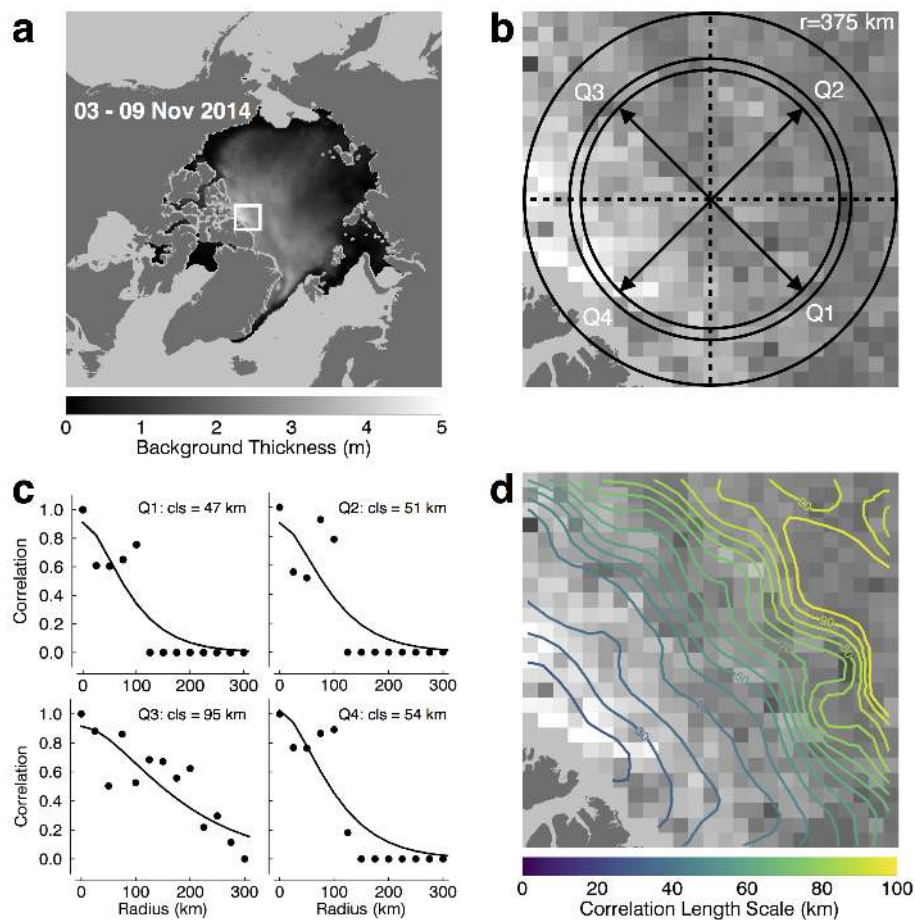


**Figure IV.6.:** Scheme for the estimation of the correlation length scale  $\xi$  for a single grid cell for the target week 3-9 November 2014. a) Background field with indicated area of interest (white box). b) Adjacent ice thickness grid cells within a radius of 375 km are binned into annuli of distance and 4 quadrants. (c) Binned thickness estimates are used to calculate the structure function of each quadrant.  $\xi$  is estimated by fitting an exponential function. d) Contour map of estimated correlation length scales for the considered area.

### IV.3.2. Correlation Length Scale Estimation

The correlation length scale  $\xi$  controls the impact of a data point on the analysis grid point depending on the distance. Considering the grid resolution of 25 km, we aim for large scale correlations. Ideally, our correlation length scale estimate is large in the center of a certain ice type regime with similar ice thickness (i.e. level FYI). On the other hand, we expect a low  $\xi$  value at locations with varying thickness gradients. Figure IV.6 illustrates the estimation of  $\xi$  for a certain grid cell  $Z_0$  in the Lincoln Sea during a week in November. In order to estimate  $\xi$ , we consider the unfiltered background field  $Z_b$  (Figure IV.6a). In the following, we define a structure function  $\epsilon^2$ , which is related to the normalized auto correlation function  $R(d,Q)$  as follows (Böhme and Send, 2005):

$$\begin{aligned}\epsilon^2(d, Q) &= \overline{(Z'_0 - Z'_{Q,d})^2} = 2\overline{\sigma_{Z'}^2} - 2\overline{\sigma_{Z'}^2}R(d, Q), \\ R(d, Q) &= 1 - \frac{\epsilon^2(d, Q)}{2\overline{\sigma_{Z'}^2}}.\end{aligned}\quad (IV.6)$$

Quadrants  $Q$  are defined to accommodate the anisotropy of the spatial ice thickness distribution (Figure IV.6b).  $\epsilon^2(d, Q)$  represents the square differences between ice thickness of the grid cell and the ice thickness of the grid cells of binned 25 km distances  $d$  in a quadrant  $Q$ .  $Z'_{Q,d}$  is the unfiltered background thickness, binned according to  $d$  and  $Q$ . Figure IV.6b reveals the annuli of distance and the 4 Quadrants.  $\overline{\sigma_{Z'}^2}$  are the corresponding mean variances of a certain quadrant. With Eq. IV.6 we then obtain the auto correlation function  $R(d,Q)$ , which is computed up to radius of 750 km (30 bins). In the next step, we fit a function of the form:

$$C(d, \xi) = \left(1 + \frac{d}{\xi}\right) \exp\left(\frac{-d}{\xi}\right) \quad (IV.7)$$

to  $R(d,Q)$  and obtain an estimate for  $\xi$ . Figure IV.6c shows the calculated auto correlation function  $R(d,Q)$  and the functional fit (Eq. IV.7). A stronger decay of  $R(d,Q)$  occurs with rising deviation between  $Z_0$  and the thickness at a certain distance in a certain quadrant.  $R(d,Q)$  can also become negative if  $\epsilon^2(d,Q)/2\overline{\sigma_{Z'}^2}$  becomes  $>1$ . In order to improve the fitting performance, we set  $R(d,Q) = 0$  if  $R(d,Q)$  becomes  $< 0$ . Furthermore,  $\xi$  is rejected if the computation fails. Finally, we average the  $\xi$  values from the 4 quadrants. In order to remove outliers and noise, the derived  $\xi$  grid is low-pass filtered with a smoothing radius of 25 km. Grid cells with failed computation are interpolated by a nearest neighbor scheme afterwards. Figure IV.6d shows the spatial correlation length scales  $\xi$  for 3-9 November 2014. It highlights the sensitivity to changing thickness gradients as  $\xi$  decreases towards the coast of the Canadian Archipelago, where higher sea ice thickness gradients likely occur due to increased deformation.

### IV.3.3. The Optimal Interpolation Algorithm

The weight matrix  $K$ , which is needed for the computation of  $T_a$ , is retrieved by the background error covariance matrix  $B$  in the observation space, multiplied by the inverted total error covariance matrix:

$$K = BH^T(R + HBH^T)^{-1}, \quad (IV.8)$$

where  $R$  is the error covariance matrix of the observations. In order to reduce computation expense we assume the following:

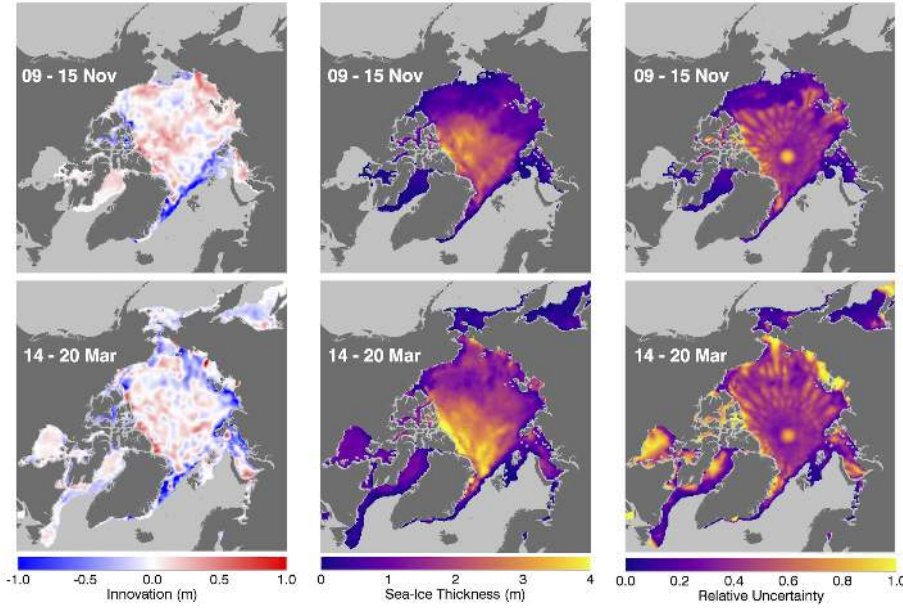


**Figure IV.7.:** a) Normalized K weights and according sea-ice thickness observations in the vicinity of the target grid cell. b) Optimal interpolation output grids for weeks in November 2015 and March 2016: The innovation (left column) shows the difference between background field and the CS2SMOS ice thickness (center column). The right column shows the relative uncertainty associated with the optimal interpolation.

1. We neglect correlations of observation errors which means that  $R$  is a matrix with non-zero elements only on the diagonal. These variances are represented by the SMOS and CS2 product uncertainties.
2. We assume that the influence of observations that are located far away from the analysis grid point can be neglected. Therefore, instead of computing the entire covariance matrix, we only consider observations within a radius of influence. This radius is set to 250 km to gather just enough observations in regions which large gaps, for example over MYI between two CS2 orbits where valid SMOS observations are not available.
3. To further reduce computation expense we limit the number of matched observations to 120, meaning that in the case of more matches, only the 120 closest observations are considered.
4. We generally assume that all observations are unbiased.

$BH^T$  and  $HBH^T$  are estimated using the correlation function in Eq. IV.7:

$$\begin{aligned} BH^T &= \left( 1 + \frac{d(x_{o_i}, x_{a_i})}{\xi} \right) \exp \left( \frac{-d(x_{o_i}, x_{a_i})}{\xi} \right), \\ HBH^T &= \left( 1 + \frac{d(x_{o_i}, x_{o_j})}{\xi} \right) \exp \left( \frac{-d(x_{o_i}, x_{o_j})}{\xi} \right), \end{aligned} \quad (IV.9)$$

with the Euclidian distance function:

$$d(x, y) = \|x - y\|_2 \quad (IV.10)$$

Here,  $x_{o_i}$  and  $x_{a_i}$  represent the locations of the observations and the analysis grid points. The covariances in Eq. IV.9 are scaled with the variances of the observation ensemble. As a

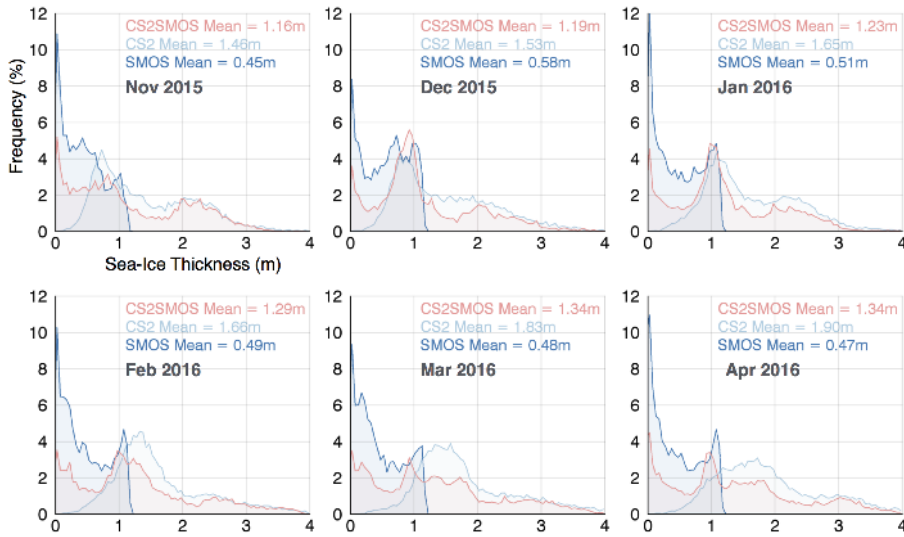


**Figure IV.8.:** a) Difference between the CS2SMOS fusion product and weekly SMOS retrieval for weeks in November 2015 and March 2016. b) Difference between CS2SMOS thickness for weeks in November 2015 and March 2016, and the corresponding monthly CryoSat-2 thickness retrieval

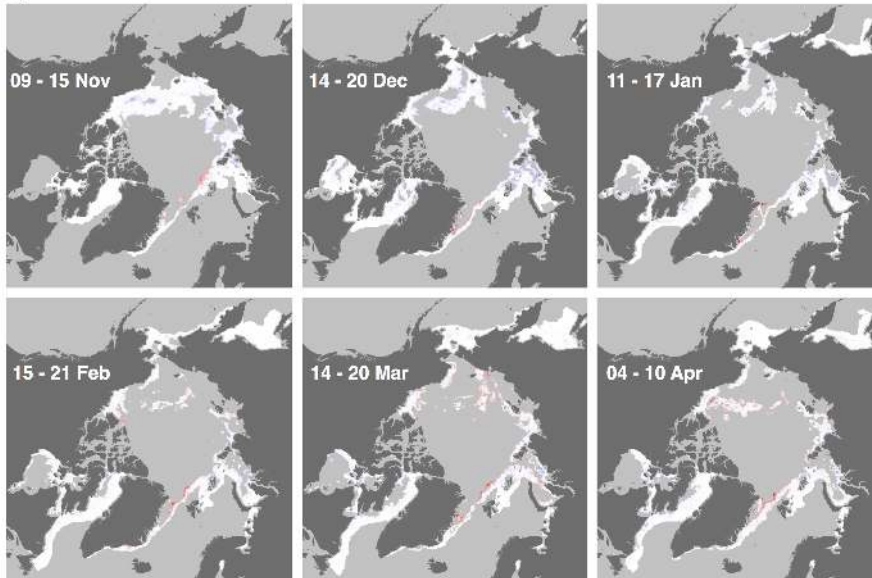
consequence of Eq. IV.9, the impact of a data point decreases with increasing distance.

Computing  $BH^T$  and  $HBH^T$  allows the computation of the K weights. Thus, we retrieve the second part of Eq. IV.4, which is called innovation. This iterative procedure is accomplished for each analysis grid cell, leading to the complete analysis grid  $T_a$ . The corresponding analysis error covariances are derived by:

$$\sigma_{T_a}^2 = (I - KH)B \quad (IV.11)$$

Since we consider variances exclusively, we only calculate the diagonal elements of  $\sigma_{T_a}^2$ . Figure IV.7a illustrates how the analysis thickness is derived at a certain grid point considering ice thickness estimates grid cells in the vicinity. The K weights decrease with increasing distance to the analysis grid point as a consequence of Eq. IV.9. On the other hand, the individual uncertainties affect the weighting according to Eq. IV.8. The considered grid cell is located at the boundary between the CS2 and SMOS domain. SMOS ice thicknesses of about 1 m reveal higher uncertainties than corresponding CS2 estimates (Figure IV.1) and hence the K weights of CS2 estimates exceed the SMOS weights. Figure IV.7b shows the innovation field, the data fusion product and the analysis error field, which is the root of the error variance (Eq. IV.11). The analysis error is a relative quantity with values between 0 and 1. It increases where the weekly CS2 retrieval leaves gaps and where valid SMOS observations are not available, for example at the North Pole or over MYI. In this case the analysis depends on the accuracy of the background field, leading to increased uncertainties.

**a** CS2SMOS - SMOS



**b** CS2SMOS - CryoSat-2

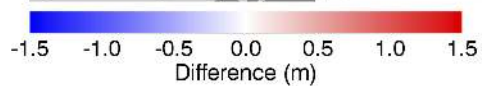
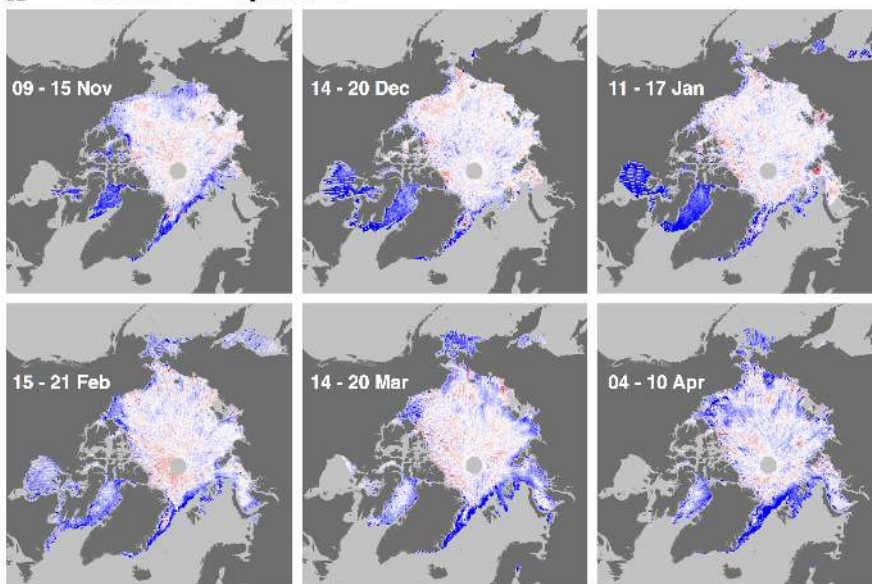


**Figure IV.9.:** a) Sea-ice thickness distributions of CryoSat-2, SMOS, and CS2SMOS retrievals for November 2015 and March 2016. CS2SMOS is represented by one week in the middle of a month, while the CryoSat-2 and SMOS retrievals are monthly means. b) Scatter diagrams illustrating the ice thickness differences between the CS2SMOS fusion product and the individual satellite retrievals of CS2 and SMOS, for November 2015 and March 2016.

## IV.4. Evaluation of the CS2SMOS Fusion Product

In this section, we aim to evaluate the CS2SMOS product by a comparison with the individual satellite products as well as a cross validation experiment and validation with airborne sea-ice thickness measurements in the Barents Sea.

### IV.4.1. Comparison with individual Products

Figure IV.8 illustrates the differences between CS2SMOS and the CS2 and SMOS retrievals from November 2015 to April 2016. The difference between CS2SMOS and SMOS weekly grids are shown in Figure IV.8a, limited to the SMOS domain over thin ice. Positive anomalies of up to 1 m occur mostly in the transition zone between the SMOS and the CS2 domain where the thick ice in the CS2 retrieval leads to an increase of ice thickness in these grid cells with respect to the SMOS data (Figure IV.7). However, the general pattern remains the same during the season. Subtracting the CS2 monthly mean sea-ice thickness from the CS2SMOS product, represented by one week within each month, reveals substantial scattering between -1 m and 1 m within the CS2 domain (Figure IV.8b). This is mainly caused by the fact that the monthly retrieval is compared with the weekly product. During the different time spans, the sea-ice thickness distribution is subject to ice drift, convergence and divergence, as well as thermodynamic ice growth. In addition, the optimal interpolation algorithm evokes a low pass filtering of the spatial thickness distribution, reducing the noise in the original CS2 product, which is unfiltered. Within the SMOS domain we find consistently negative anomalies, indicating a reduction of the CS2 ice thickness representation due to the impact of the SMOS retrieval.

Figure IV.9a shows ice thickness distributions of monthly means of CS2 and weekly SMOS and CS2SMOS ice thickness retrievals for November 2015 and March 2016, illustrating the different thickness ranges of CS2 and SMOS retrievals. Table IV.1 presents the corresponding statistics for the entire winter season including the mean and the standard deviation of each month or week respectively. The CS2 retrieval lacks sensitivity for thin ice (< 0.5 m) over the entire season. This gap is closed by the SMOS retrieval. While the mean thickness of the CS2 retrieval consistently grows from 1.46 m in November to 1.90 m in April, the SMOS thickness mean remains at about 0.5 m after an increase from November to December. Due to the lack of sensitivity for thick ice and the maximum uncertainty filter that is applied to the SMOS product, the frequency steeply drops at about 1 m for each month. Therefore, the SMOS mean thickness is mostly affected by the boundary condition at about 1 m in conjunction with thermodynamic ice growth and the new formed ice (< 0.1 m). The thickness distributions show the capability of the CS2SMOS product to combine the complementary ice thickness ranges. As a consequence, the standard deviation of the merged product ranges between 0.8 m (December) and 0.99 m (April), and therefore exceed the standard deviations of the individual products that reach maximum values of 0.78 (CS2) and 0.38 (SMOS) in April. The scatter diagrams in Figure IV.9b illustrate the thickness differences between CS2SMOS and the two individual products, with respect to the maps shown in Figure IV.8. Using the SMOS data reduces the thickness in the CS2SMOS product below 1m compared to the CS2 retrieval. The comparison between CS2SMOS and SMOS shows increasing scattering with rising thickness. As shown in Figure IV.8, this originates from the transition zone between the CS2 and SMOS domain.

**Table IV.1.:** Statistics of the merged product (CS2SMOS) and the individual CryoSat-2 (CS2) and Soil Moisture and Ocean Salinity (SMOS) retrievals for the winter season 2015/16. Mean and standard deviation (sdev) are given in meters.

	Nov	Dec	Jan	Feb	Mar	Apr
CS2SMOS mean	1.16	1.19	1.22	1.29	1.36	1.34
CS2 mean	1.46	1.53	1.65	1.66	1.83	1.90
SMOS mean	0.45	0.58	0.51	0.49	0.48	0.47
CS2SMOS sdev	0.88	0.8	0.81	0.92	0.96	0.99
CS2 sdev	0.76	0.76	0.72	0.73	0.75	0.78
SMOS sdev	0.33	0.36	0.38	0.37	0.36	0.38

#### IV.4.2. Cross Validation

In order to test the performance of the optimal interpolation algorithm, we carry out a cross validation. We randomly separate different fractions of the observation data of the target week (see Figure IV.4 and IV.5). Specifically, we sort out 10% (Figure IV.10a), 25% (Figure IV.10b) and 50% (Figure IV.10c) of CS2 and SMOS grid cells of the target week. In the fourth case, all data contained in a box in the Western Arctic are withdrawn (Figure IV.10d). The box intentionally covers both the SMOS and the CS2 domain. After the separation, the optimal interpolation algorithm is applied using the reduced target week data set. The maps shows the difference between the retrieved CS2SMOS sea-ice thickness and the withdrawn thickness data for each case. Compared to the SMOS domain, the CS2 domain in the Central Arctic (Figure IV.2) reveals a higher level of noise with deviations of up to 1 m. On the other hand, the SMOS domain shows a slightly negative shift of up to 10 cm in some areas. The general pattern remains the same in all cases, independent from the fraction of data that are withdrawn in advance. The shape of the histograms of the differences indicates a normal distribution with similar standard deviations between 14 and 17 cm. The mean differences are between -2 and -3 cm. The slightly negative value likely originates in the SMOS domain, indicated by the difference maps. Since we use the weekly SMOS thickness mean of the previous week for the background field (Figure IV.5), the temporal delay might cause a small negative bias due to the advancing ice growth. However, in contrast to CS2, the weekly SMOS data coverage during the target week is complete and therefore, this negative bias should not affect the CS2SMOS sea-ice thickness retrieval. The root mean square deviation (rmsd) is 22-24 cm for the first 3 cases and 14 cm for the last case where we separated a box. The smaller rmsd is likely caused by the lack of thicker ice in the chosen box, which does not contain sea ice thicker than about 2 m. This experiment demonstrates the performance of the applied algorithm. In particular, it shows that the background field conserves the mean values even when co-located observations are missing.

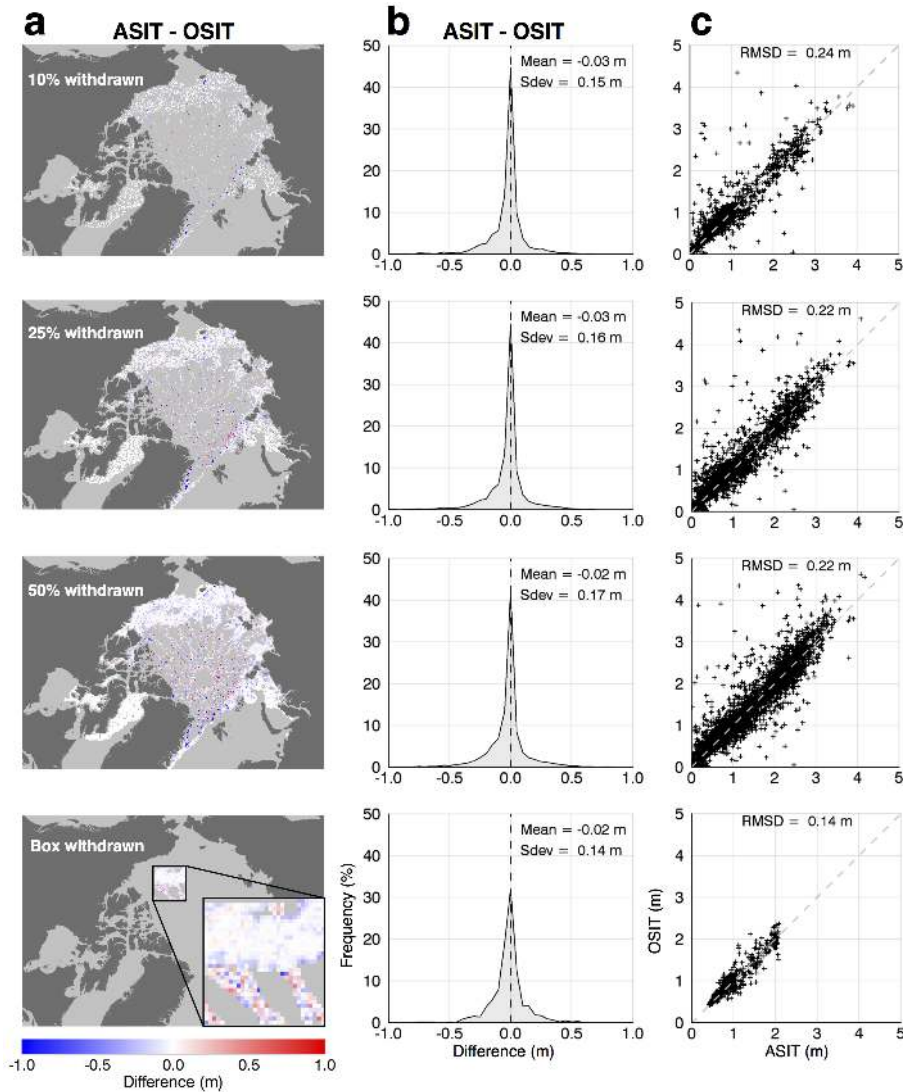


**Figure IV.10.:** Cross-validation experiment. Difference between the CS2SMOS ice thickness and gridded CryoSat-2 and SMOS observations (OBS) that have been separated in advance as different fractions/areas of withdrawn data: a) 10%, b) 25%, c) 50%, and d) Box. The maps show the withdrawn data subtracted from the CS2SMOS product. The Histograms show the differences according to the maps, indicating mean and standard deviation (Sdev) of the differences. Scatter diagrams indicate the root mean square deviation (RMSD).

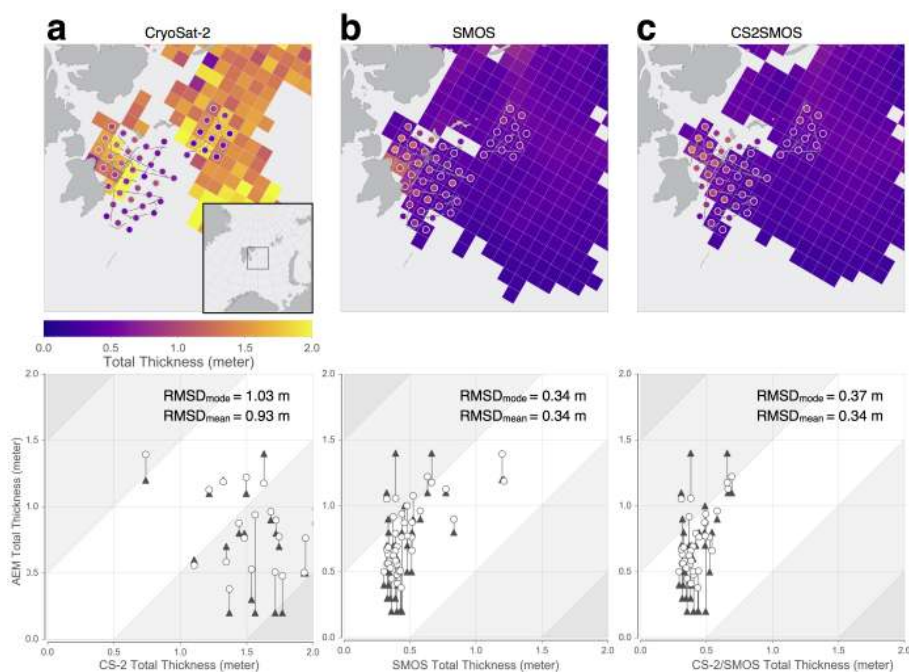


**Figure IV.11.:** Comparison of airborne EM validation data (AEM) over thin ice in the Barents Sea east of Spitsbergen with a) monthly CryoSat-2 sea-ice thickness, b) weekly SMOS sea-ice thickness, c) CS2SMOS fusion product. In the scatter diagrams, triangles indicate modal AEM ice thickness, while circles indicate mean AEM ice thickness.

### IV.4.3. Validation with Airborne EM

We use sea-ice thickness measurements obtained during the SMOS-ice 2014 campaign east of the Spitsbergen Archipelago to validate the CS2SMOS product. Between March 19-26, 8 flights have been carried out with an airborne electromagnetic induction thickness sounding device (EM-Bird) (Pfaffling et al., 2007; Hendricks, 2009) that was towed by a helicopter based on the Norwegian research vessel Lance. The airborne thickness data (AEM) are projected and averaged on the EASE2 grid as given by the CS2 and CS2SMOS products. The AEM data set represents total thickness, comprising snow + sea-ice thickness. Therefore, we add the climatological snow depth, which is likewise used for the CS2 freeboard-to-thickness conversion, to the satellite products. Figure IV.11 shows the comparison between AEM ice thickness measurements and the three satellite products: CS2 (a), SMOS (b), and CS2SMOS (c). The maps illustrate the spatial distribution and the mean thickness of AEM measurements and the co-located satellite retrievals. In addition to the mean AEM thickness in each grid cell, we also calculated the modal AEM thickness. The scatter diagrams illustrate the difference between the satellite products and the corresponding mean and modal AEM thickness. For the CS2 retrieval, the rmsd is 0.93 m for the AEM mean thickness and 1.03 m for the AEM modal thickness, indicating a slightly better representation of the mean thickness in the CS2 product. However, the scattering is substantial and the bias with respect to the mean AEM thickness of 0.78 m suggests a bias towards thicker ice. Such errors might originate from erroneous sea-surface height interpolation along the CS2 orbits. The SMOS and CS2SMOS retrievals are almost identical for that region, which is caused in part by the better coverage of the SMOS retrieval in that region. In addition, this region is dominated by thin ice, leading to a higher weighting of the SMOS retrieval due to the lower uncertainties (Figure IV.1). The scatter diagrams reveal a better agreement of the AEM measurements with the SMOS and CS2SMOS retrievals (rmsd = 0.34) than with the CS2 retrieval. The observed bias with respect to the mean AEM thickness is 0.29 m for the SMOS product and 0.3 m for the CS2SMOS product, suggesting a bias towards thinner ice. Moreover, the maps indicate that the SMOS (CS2SMOS) retrieval captures the small thickness gradients visible in the AEM thickness data. This provides evidence that using SMOS data in areas with a thin ice regime will reduce the rmsd and the mean bias when compared to the CS2 product.

## IV.5. Conclusions

We presented results of the first joint data fusion of CryoSat-2 sea-ice thickness fields and thin ice thickness estimates obtained from the L-Band radiometer onboard the Soil Moisture and Ocean Salinity (SMOS) satellite. While CryoSat-2 lacks the capability to observe thin ice formation, SMOS is restricted to ice regimes thinner than about 1 m. We have shown that the merged product (CS2SMOS) has the capability to allow for thickness estimates, that are sensitive to the entire thickness range, providing weekly ice thickness estimates using the complementary sensitivity of the individual products to different thickness regimes. In addition, the weekly CS2SMOS retrieval benefits from the increased coverage at lower latitudes in conjunction with higher temporal resolution compared to the weekly CryoSat-2 retrieval. In particular, the usage of the combined product will improve thickness retrievals in all areas with a thin ice regime, which we have demonstrated using a case study from Barents Sea during spring 2014. Comparisons with Airborne electromagnetic sounding thickness measurements reveal a reduced root mean square deviation of about 70 cm compared to the CryoSat-2 thickness retrieval. Moreover, the comparison shows that the SMOS/CS2SMOS

retrieval seems to capture small thickness gradients, whereas the CryoSat-2 retrieval is very noisy. The CryoSat-2 retrieval overestimates mean thin ice thickness by 78 cm, while SMOS and CS2SMOS underestimate by about 30 cm. The optimal interpolation approach used in this study can be adopted to merge further sea-ice thickness or freeboard data sets derived from other satellite missions, such as the recently launched European Space Agency mission Sentinel-3, which carries a Ku-band radar altimeter similar to SIRAL onboard CryoSat-2.

## **IV.6. Data availability**

The CS2SMOS and the CryoSat-2 products are provided by AWI via <http://www.meereisportal.de>. The SMOS ice thickness data are provided the University of Hamburg via <http://icdc.cen.uni-hamburg.de>. Sea-ice concentration and Sea-ice type data are provided by OSISAF via <http://osisaf.met.no/p/ice/>.



## V ASSIMILATION OF SMOS DATA IN THE TOPAZ SYSTEM

*extracted from (Xie et al., 2016b)*

### V.1. Introduction

One of the tasks in this project is to evaluate the impact of the SMOS observations on a forecast ocean-ice-atmosphere model. Based on the multi-year dataset available and together with complementing observations and (or) a model estimate, the observations can be used to get a better description of the current state of sea ice. This analysis represents a value in itself and can subsequently be used as the initial condition in a forecasting system. First guess departures with respect to the observed variables (i.e. the difference between the model and the observations), shall ideally be obtained from a coupled (ocean-ice-atmosphere) forecasting system.

For this purpose, we investigate the benefit of assimilating SMOS thin ice thickness data (SMOS-Ice) into the TOPAZ system. The operational daily product provided by university of Hamburg, henceforth called SMOS-Ice, has been validated during a field campaign in the Barents Sea (Kaleschke et al., 2016; Mecklenburg et al., 2016) and will be used in this study. Aiming at the operational application of the thickness measurements for sea ice, the SMOS-Ice data contain daily products of sea ice thickness since October 2010 (Tian-Kunze et al., 2014).

Yang et al. (2014) studied the benefit of assimilating SMOS-Ice during the freezing period, with the Localized Singular Evolutive Interpolated Kalman filter (LSEIK, ref. Nerger et al. (2005)) in a nested Arctic configuration of the MITgcm. They found that SMOS-Ice leads to improvement of ice thickness and ice concentration. The present study follows up the work from Yang et al. (2014) but use a different model and assess: 1) the impact of assimilating SMOS-Ice both during the beginnings of melting and freezing seasons; 2) the relative contribution of SMOS-ice compared to a complete set of observations typically used in a state of the art forecasting system.

The TOPAZ system is a coupled ocean-sea ice data assimilation system that focuses on the marine environment in the Arctic region. It is the operational Arctic forecast system in the Copernicus Marine Services (<http://marine.copernicus.eu/>). The system provides 10-days coupled physical-biogeochemical forecast every day and long-term reanalysis (Sakov et al., 2010; Lien et al., 2016; Xie et al., 2016a). At present, the TOPAZ system assimilates the Sea Surface Temperature (SST), along-track Sea Level Anomalies (SLA) from satellite altimeters, in situ temperature and salinity profiles, Sea Ice Concentration (ICEC) and sea ice drift data from satellites with the Ensemble Kalman Filter (EnKF). The reanalysis product of the TOPAZ system has been widely used in studies about ocean circulation and sea ice in the northern Atlantic Ocean or in the Arctic region (Lien et al., 2016; Johannessen et al., 2014). However, TOPAZ does not assimilate sea ice thickness, and does not apply post processing for this variable. In the Arctic reanalysis, the daily sea ice thickness of TOPAZ has been validated for the period 1991-2013 compared to the different types of available observations

(Xie et al., 2016a). TOPAZ shows good agreement with the spatial distribution of ice thickness in ICESat data (available between 2003 and 2008) with a spatial correlation 0.74 in spring and 0.84 in autumn. However, TOPAZ shows a clear overestimation of ice thickness in the Beaufort Sea and an underestimation in the other areas of the Arctic. Inaccuracy in the ice thickness is a common limitation of coupled ice-ocean models in the Arctic (Johnson et al., 2012; Schweiger et al., 2011).

## V.2. Data and Method

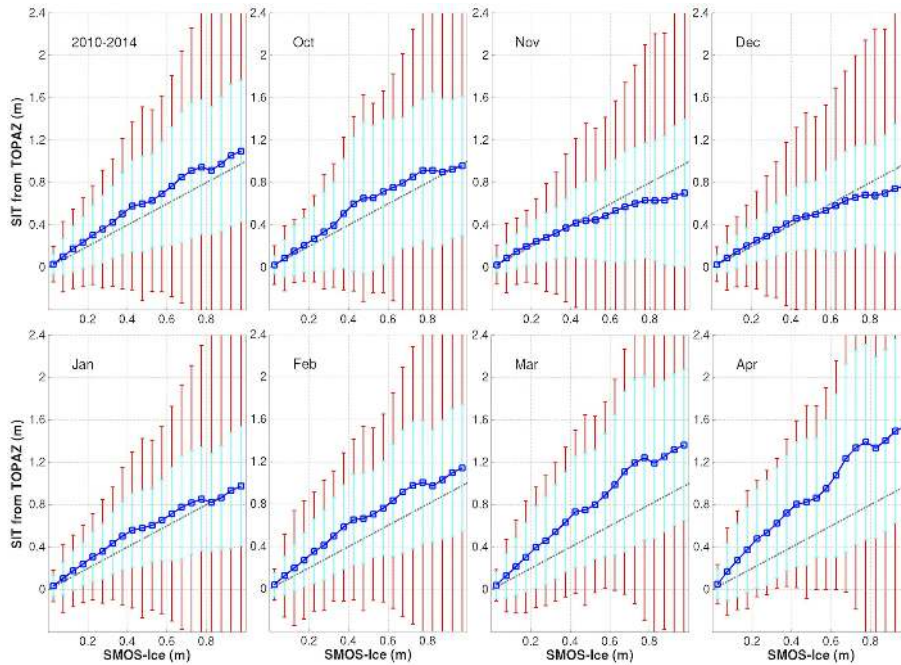
The conditions for assimilation of sea ice thickness thinner than 0.4 m are favorable, as observations are reliable below this threshold and their probability distribution is comparable to that of the model. Two paralleled runs of TOPAZ have been performed respectively in March and November 2014, with assimilation of thin sea ice thickness (thinner than 0.4 m) in addition to the standard ice and ocean observational data sets. An assumption made for data assimilation is that the model and observations have unbiased mean and uncertainties estimates. Therefore, we investigate in this section the thickness misfits of thin sea ice during five cold seasons of 2010-2014. We use v2.1 SMOS-Ice products. The sea ice thickness of TOPAZ is extracted from the model state on daily average, and then compared with the observations by calculating the bias and the Root Mean Square Difference (RMSD).

Figure V.1 shows the TOPAZ ice thickness as conditional expectations with respect to SMOS-Ice data organized by bin of 5 cm. The TOPAZ ice thicknesses shown in Figure V.1 are at the same location and time as the observations. Overall, the sea ice thickness in TOPAZ tends to be overestimated but it varies with the month and with the amplitude of ice thickness (more pronounced for thick ice). As an example, TOPAZ overestimates the high thickness values (>0.4 m) during October and February-April, while they are underestimated in November. For thicknesses lower than 0.4 m, the match between the observations and the simulations of TOPAZ is closer and rather consistent through the cold season. There is no clear bias from October to December but an increasing thick bias from January to April. There is a priori no indication whether the bias is a model bias or an observation bias. The penetration depth into sea ice is about 0.5 m for the L-Band microwaves frequency (Kaleschke et al., 2010; Huntemann et al., 2014), and the effect of ice melting may lead to a saturation thickness of less than 0.4 m (Heygster et al., 2009). In order to avoid multivariate transfers of bias (whichever the source) to other state variable during the assimilation of SMOS-Ice, we restrain the observation to thickness that are less than 0.4 m.

In Figure V.2, we estimate the yearly bias of ice thickness compared to SMOS-Ice for ice that is thinner than 0.4 m over the period 2010-2014. After 2011, the thick bias is increased, and reaches a maximum with 0.1 m in 2014. The thick bias in March is also found larger than that in November. There is spatial variability in the distribution of the bias (right panel of Figure V.2), with the bias being largest in the Beaufort Sea and in the Kara Sea. In 2014, there is a thick bias in all the regions.

The SMOS-Ice ice thickness data is gridded at a resolution of approximately 12.5 km and available at daily frequency in the cold season. Only the observations between 0 and 0.4 m, with a distance of at least 30 km away from the coast are used. To highlight the additional impacts of observations, two assimilation runs for Observing System Experiment (OSE) are named as follows:

- Official Run: uses the standard observational network of the TOPAZ system. It assimilates weekly the along-track Sea Level Anomaly, SST, in situ profiles of temperature and salinity, sea-ice concentrations and sea-ice drift data.



**Figure V.1.:** Conditional expectations of TOPAZ versus SMOS-Ice (with bins of 5 cm) for each month calculated over the period 2010-2014. The cyan error bars correspond to the RMSD against observations within each bin. The red error bars corresponds to the averaged standard deviations of observation error. The gray dashed line denotes the line  $y=x$ .

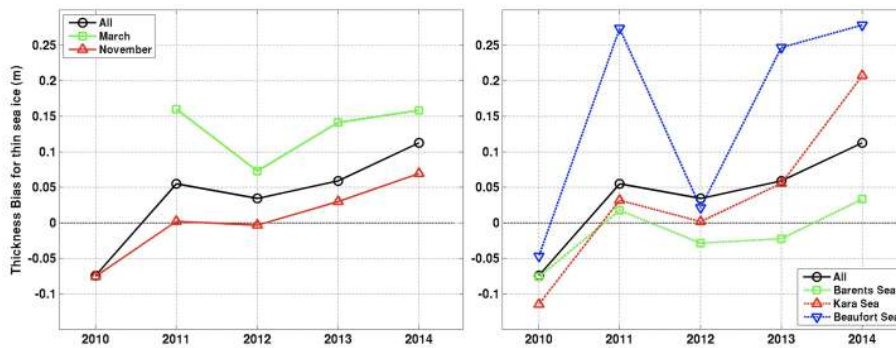


**Figure V.2.:** Yearly thickness biases of thin sea ice from TOPAZ compared to SMOS-Ice observations. The black line represents the yearly mean bias. Left: the green (red) line represents the mean bias for March (November) months. Right: the colored lines represent the biases in the Barents Sea, the Kara Sea, and the Beaufort Sea.

-Test Run: assimilates the SMOS-Ice data in addition to observations assimilated in the official run. The observation error of the sea ice thickness uses the uncertainties recommended by the provider, with an upper limit of 5 m beyond which the observations are assumed to have negligible impacts. This uncertainty is rather a priori estimate of the maximum uncertainty with respect to variations in some parameters (Tian-Kunze et al., 2014). Here, the observation error is assumed spatially uncorrelated.

We have two parallel assimilation runs focusing on two typical time periods within the beginnings of ice melting and freezing, from 19th February to 31st March and from 22nd October to 30th November in 2014. Both runs are driven by the same atmospheric high frequency forcing from ERA-Interim (Dee et al., 2011). Finally, the daily averaged outputs in March and November are used for the evaluation.

### V.3. Results

The error analysis focuses on the following target quantities: sea ice thickness, sea ice concentration, SST and SLA. All quantities are derived from daily averages at same observation locations and time, and the calculation of the bias and the RMSD.

The spatial distribution of selected SMOS-Ice data for thin sea ice is shown in the top panels of Figure V.3 during March and November of 2014. In March, the available observations in the Beaufort Sea are very few, and inhomogeneously distributed - mainly located in the coastal estuary areas. During this period, most of the observations are unreliable in the Beaufort Sea (with error of approximately 5 m) so that they are rejected. Therefore in the following analysis, we will only present the result in November for the Beaufort Sea. In the middle panels of Figure V.3, the differences of RMSD for sea-ice thickness between the Official Run and the Test Run are shown (red color indicates an improvement due to assimilation of SMOS-Ice). In March, the improvements are mainly found to the east of Franz Josef Land and to some extent near the ice edge in the Greenland Sea. In November, the reduction of RMSD is larger than 0.2 m in the Beaufort Sea, the Greenland Sea and to the north of Svalbard. Finally, the differences of monthly ice thickness between the Official Run and the Test Run are shown in the bottom panels of Figure V.3. It suggests that the impact of assimilating SMOS-Ice leads to a reduction of sea-ice thickness both in March and November of 2014.

The time series of daily bias and RMSD for thin ice thicknesses in the OSE runs are shown in the top panels of Figure V.4. The bias of thin sea-ice thickness is reduced from 16 cm to 12 cm in March, and from 7 cm to 4 cm in November, when SMOS-Ice data is assimilated. The RMSD of thin sea ice is reduced from 35 cm to 31 cm in March, and from 27 cm to 21 cm in November. This corresponds to a reduction of the bias of 25% in March and 43% in November, and a reduction of the RMSD of about 11% in March and 22% in November. In the other panels of Figure V.4, the bias and RMSD of sea ice concentration, SST and SLA are presented. There is a slight benefit for the bias and RMSD of sea ice concentration, but the statistics for SST and SLA are unchanged.

Moreover, the averaged thicknesses of thin sea-ice in the marginal seas - in the Kara Sea, Barents Sea and Beaufort Sea - are shown with marked lines in the panels of Figure V.5. The corresponding daily RMSDs of ice thickness relative to thin SMOS-Ice data are added with shading. In each month, there are four assimilations marked with the vertical lines.

In the Kara Sea, the thickness observed in March is very stable with a slight gradual increase. There is a relatively uniform reduction of RMSD by about 21%, which is mainly the result from a correction of the large (too thick) bias in the model. In November, the bias

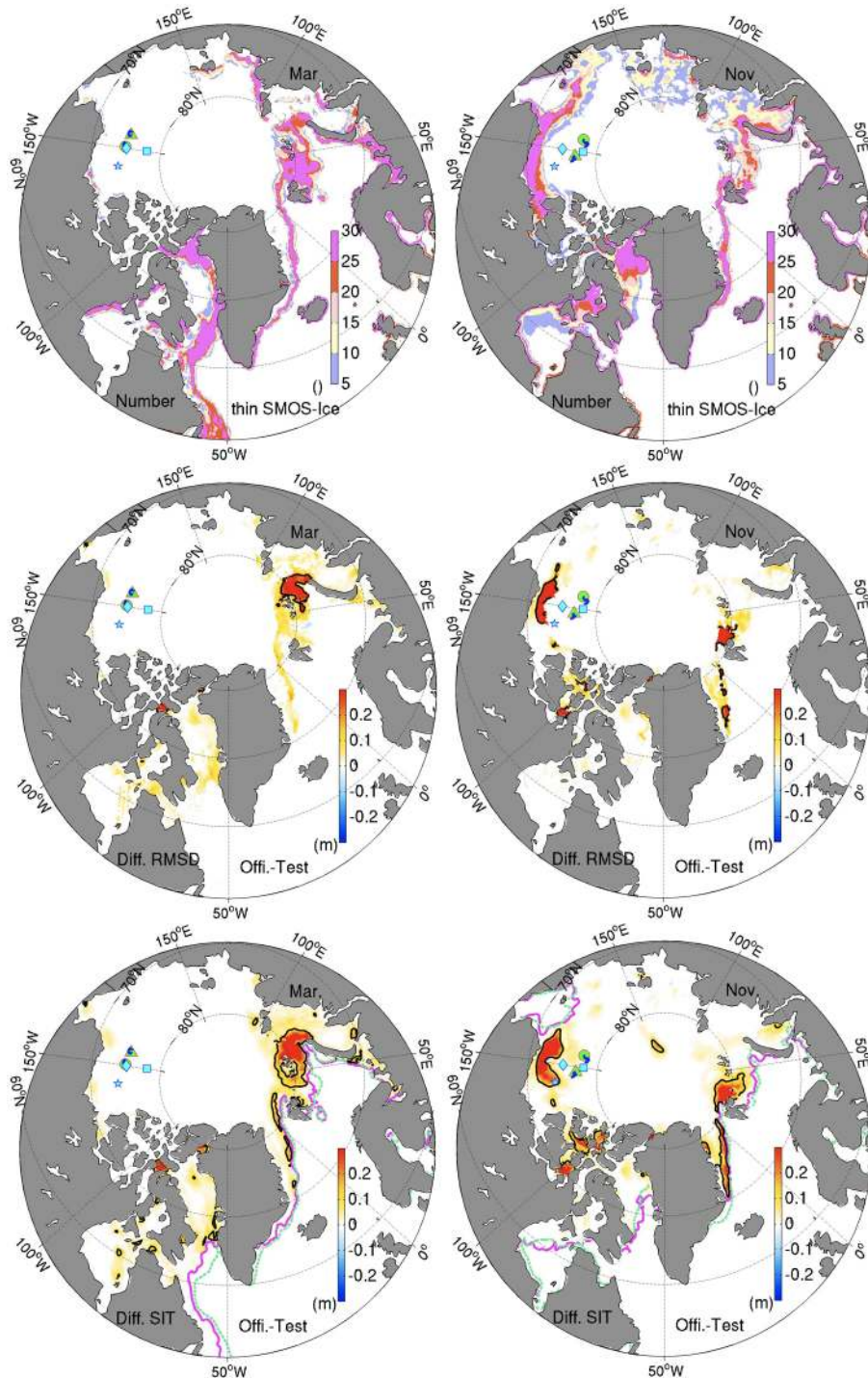


**Figure V.3.:** Top row: number of the valid SMOS-Ice data in March (left) and in November (right) of 2014. The trajectories of the buoys 2013F and 2013G (2013F and 2014F) from IMB are the blue lines in March (November). Their first positions are marked by circle and triangle respectively. In March (November), the mooring locations from BGEP-2013a,b, and d)- are marked by diamond, square, and pentagram respectively. Middle row: difference of RMSDs for the thin SIT between official run and test run. The black line denotes the 0.2 m isoline. Bottom row: difference of SIT between official run and test run. The black line denotes the 0.2 m isoline, and the green (magenta) line is the 15% concentration isoline from OSISAF (official run).

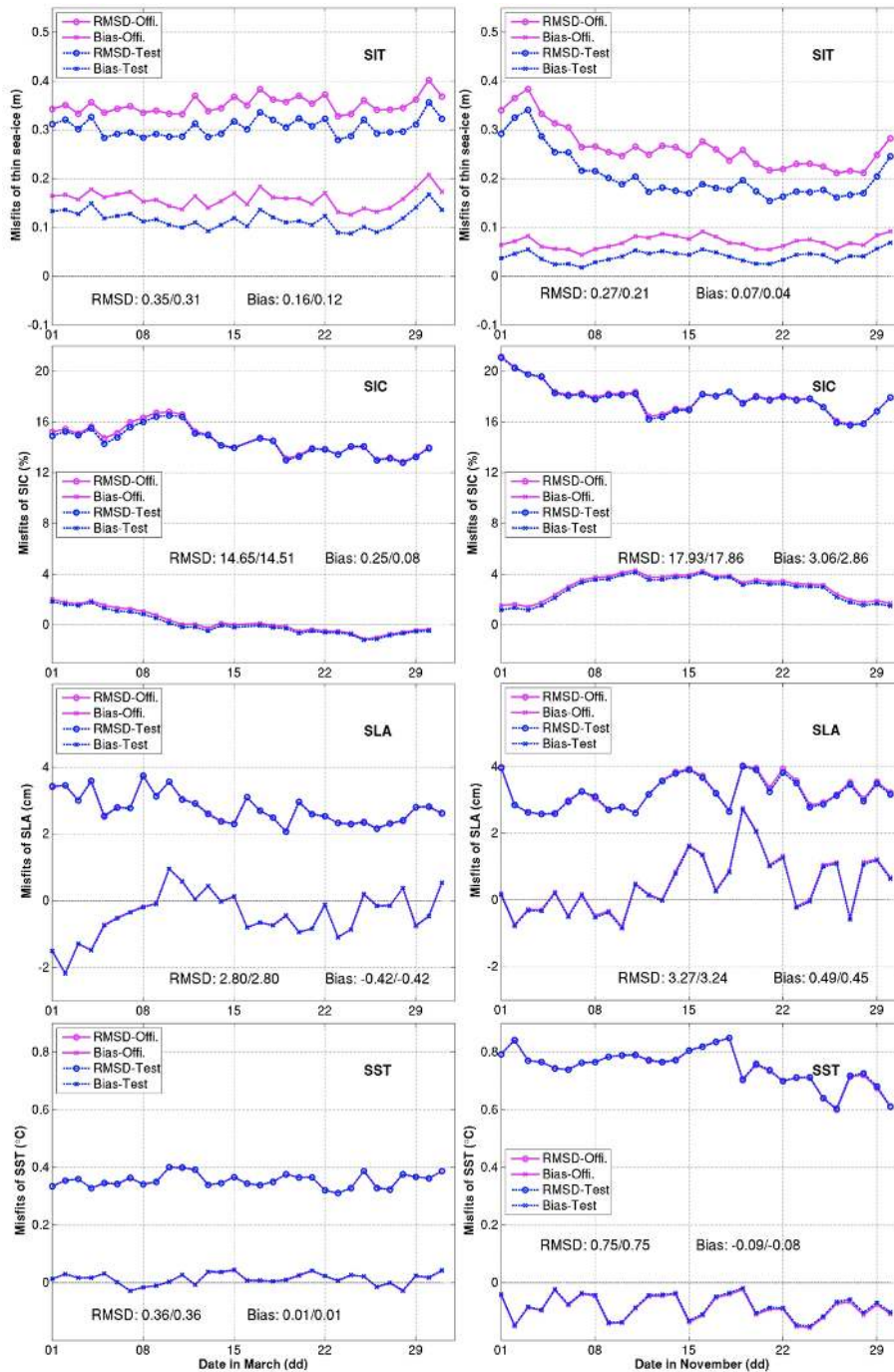
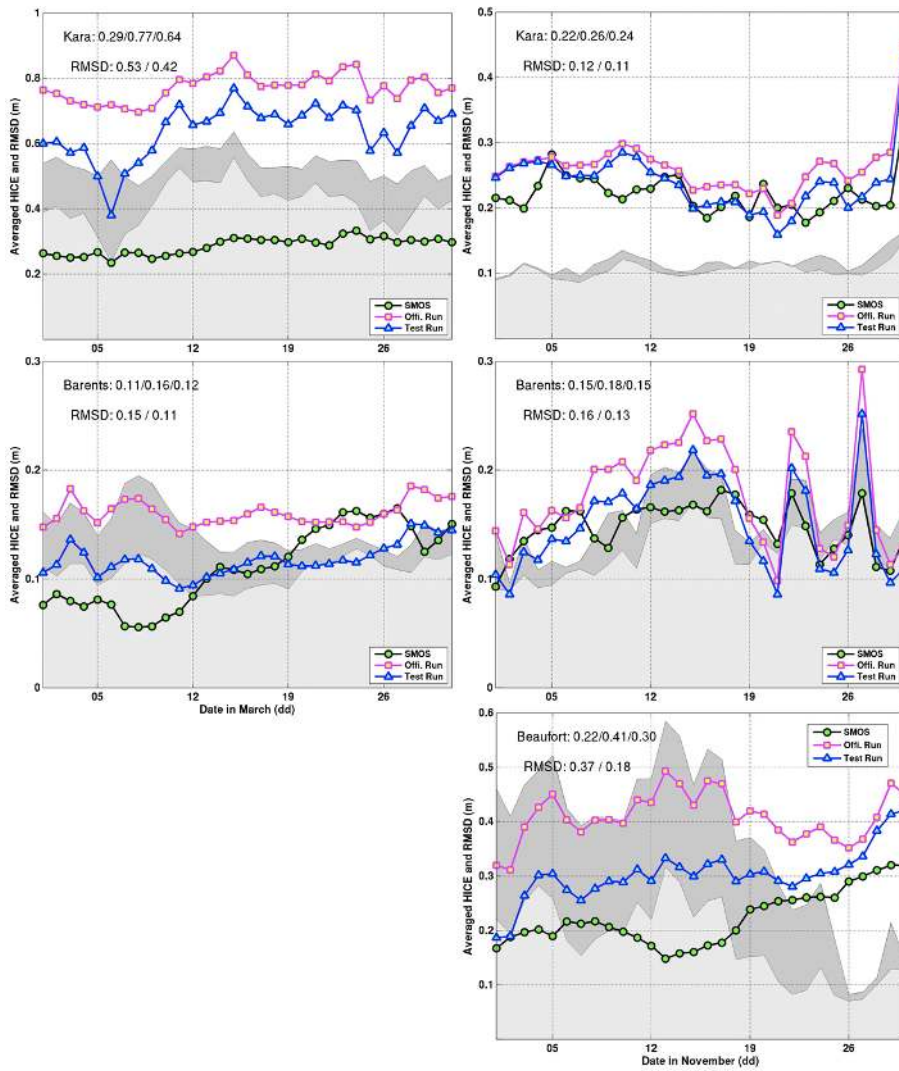


Figure V.4.: Daily time series of the bias (marked with crosses) and the RMSD (marked with circles) calculated for the Arctic region in the official run (magenta) and the test run (blue) for different variables in March (left) and November (right).



**Figure V.5.:** Daily time series of the mean SIT for thin sea ice in the Kara Sea (top row), the Barents Sea (middle row), and Beaufort Sea (bottom row) in March (left) and November (right). The light (dark) gray shading is the daily spatial RMSD of thin sea ice in the test run (official run).

is much smaller and the resulting improvement is smaller (8%) but the performances are slightly improving through the month for RMSD.

In the Barents Sea, in March, the observations show an increasing trend. The official run shows initially a large (thick) bias that is reduced as the thickness increase in the observation. Assimilation of SMOS-Ice data reduces well the initial bias, but the bias converges with the official run at the end of the month and so is the RMSD. On average, the RMSD of ice thickness is decreased about 27% from the Test Run. In November, the observations show large variability that is well captured in the Official Run but the ice is initially too thick. The RMSD reduction is about 19% from the Test Run compared to from the Official Run and both the bias and the variability seem to be reduced.

In the Beaufort Sea, there are too few observations to provide a representative estimate of the system performance in March (top panels of Figure V.3) and the statistic are not presented. In November, the observations shows an increasing trend and the official run shows once more a relatively large thick bias initially. The RMSD in the Test Run is reduced by about 51%, which is mainly caused by a reduction of the bias. The increasing trend in the Test Run is in relatively well agreement with the observations.

In Figure V.6, we are validating the ice thickness with independent observations of sea-ice thickness from three buoys (2013F, 2013G, and 2014F). Their drift trajectories are shown in Figure V.3. These measurements are estimated from the autonomous Ice Mass Balance (IMP; <http://imb.ercd.dren.mil/buoyinst.htm>) buoys respectively. Along the buoy trajectory, the daily series of the observed sea ice thickness from 21st October to 30th November are shown with the blue squared line and the standard deviation is shown with error bars. The overestimation of sea ice thickness in the Official Run is slightly reduced (with a maximum decrease of 2 cm). It is expected that the impact of SMOS-ice on the two buoys are small because they are located far away from location where SMOS-Ice data is assimilated. Note that in TOPAZ system, we use localization, meaning that the impact of observations is limited to a certain radius and their influence reduces as function of distance. In TOPAZ the effective localization radius is 90 km. It is encouraging to see that the improvement seems to be increasing with time suggesting that the region influenced by SMOS-ice is spreading in the domain with time.

The additional benefit of assimilating SMOS-Ice into the TOPAZ system is quantitatively compared to the standard observation network used. To do so, we evaluate a metric calculated during the analysis, the Degree of Freedom for Signal (DFS), which is now widely used for such purpose (Rodgers, 2000; Cardinali et al., 2004).

DFS quantifies the reduction of mode that can be attributed to each observation type. A value of DFS close to 0 means that the observation had no impact, while a value of  $m$  means that the assimilation has reduced the number of degree of freedom of the ensemble by  $m$ . Note that the reduction cannot exceed the ensemble size; i.e. 100 here. In Sakov et al. (2012), it was proposed that a system should in fact not exceed 10% of the ensemble size to avoid a collapse of the ensemble.

In Figure V.7, we are plotting the averaged DFS for the different observation data set assimilated with space in March and November. In the Arctic the total DFS is dominated by the ice concentration with large value near the ice edge. The DFS for SMOS-Ice is comparatively smaller. It is larger in March than in November. However, in some region, the monthly DFS of SMOS-ice reaches value larger than 2.

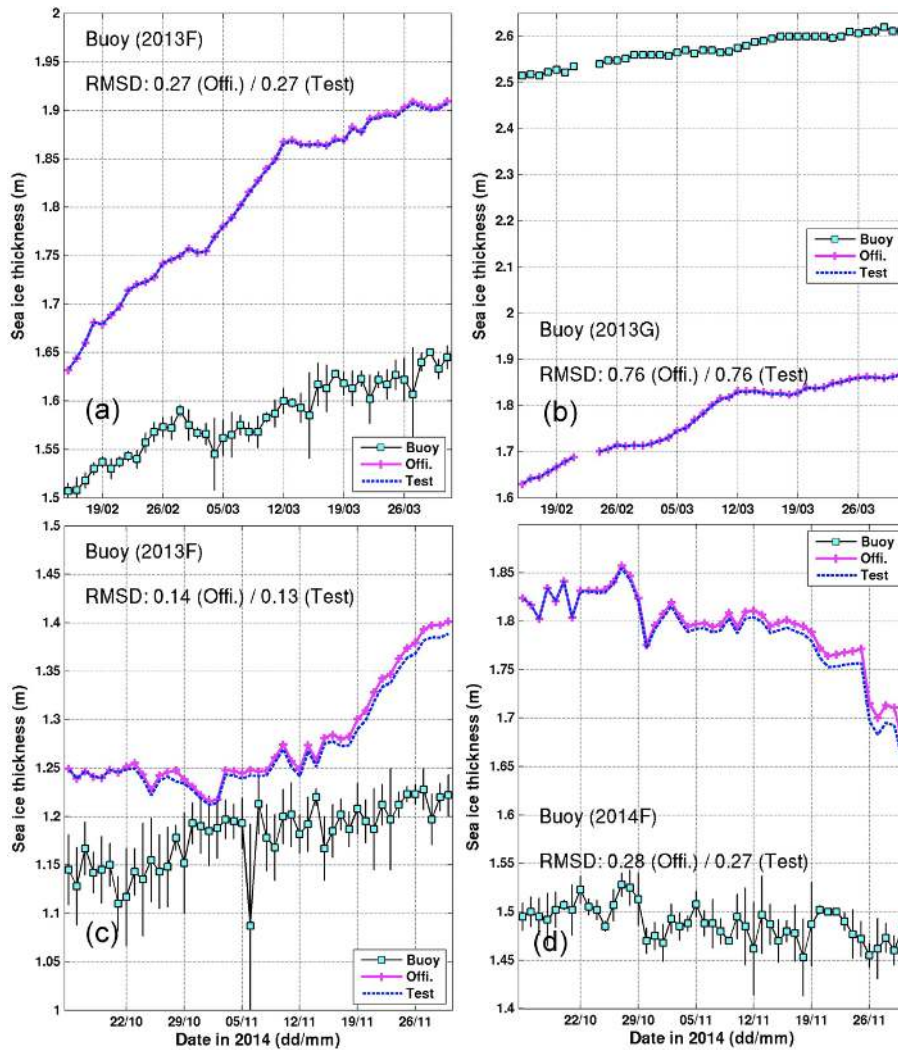


**Figure V.6.:** Daily time series of SITs from official run (crossed magenta line) and test run (dashed blue line) compared to the buoy measurements from IMB (squared black line). The daily standard deviations of the observations are shown with error bars. The buoy locations and their drift trajectories in the month are shown in Fig. 5. Upper row covers the period 15 Feb. to 30 Mar. 2014 by (a) Buoy 2013F and (b) Buoy 2013G. Bottom row covers period 15 Oct. to 30 Nov. 2014 by (c) Buoy 2013F and (d) Buoy 2014F.

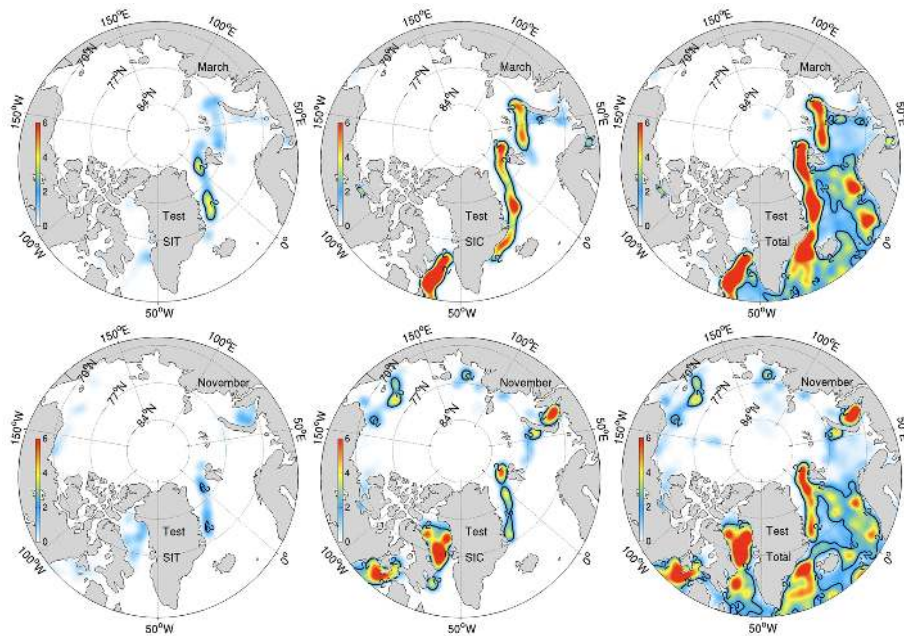


**Figure V.7.:** Monthly averaged DFS from the test run in March (upper) and in November (lower) for sea ice thickness from SMOS-Ice (left column), sea ice concentration from OSISAF (middle column), and the total DFS of all assimilated observations (right column). The black line denotes the isoline of DFS equal to 2.

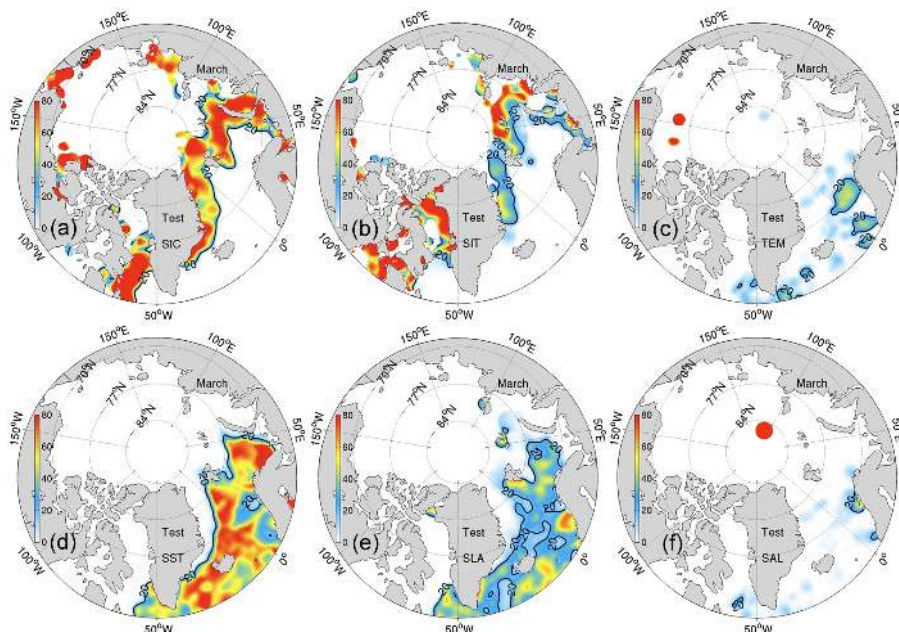


**Figure V.8.:** Relative contributions of each observational data set in the total DFS during March 2014. (a) Sea ice concentration from OSISAF; (b) sea ice thickness from SMOS-Ice; (c) temperature profiles; (d) SST; (e) along-track sea level anomaly (SLA); (f) salinity profiles. The black line is the 20% isoline.

Figure V.8 and Figure V.9 show the relative contribution of each observational data set. As expected, the assimilation of ice concentration dominates the total DFS, while the impacts of SST and SLA are limited to the region that are not ice covered. Profiles near the North Pole in the Arctic are the Ice-Tethered Profiles (ITP), which are collected by the Ice-Tethered Profiler Program (Krishfield et al., 2008; TOOLE et al., 2011). They have a very large impact but they are very sparse. In March the SMOS-ice data has a significant impacts (> 20% of the total DFS) in the Northern Barents Sea, the western Kara Sea, in the Baffin Bay, in the Greenland Sea and in the Hudson Bay. In November, the relative contribution is still large in the Barents Sea, the Kara Seas and the Greenland Sea, but it is now also large in the Beaufort Sea, and in the Canadian Archipelagos.

## V.4. Conclusions

To conclude, our study suggests that SMOS-Ice can be assimilated without degradation of other skills in our operational forecasting system. The benefits are generally small but can be significant for some regions near the ice edge. However, further work needs to be done to better understand the uncertainty of the assimilated SIT from the SMOS-Ice. Recently, Yang et al. (2016) tested the sensitivity of assimilating the SMOS-Ice data with the LSEIK during the winter of 2011-2012, and they found that perturbations of the atmospheric forcing is important for improving the performance of assimilation, in agreement with (Lisæter et al., 2007).

In the future, we may use the “saturation ratio” that is defined by the relationship of the variable L-band penetration depth and the maximal retrieval thickness as a function of temperature and salinity with which we can better identify the valid observations of sea ice thickness from SMOS.

In addition, the satellite CryoSat-2 provides freeboard height data in thick ice that can complement the observations from SMOS (Kaleschke et al., 2010). The new sea ice thicknesses

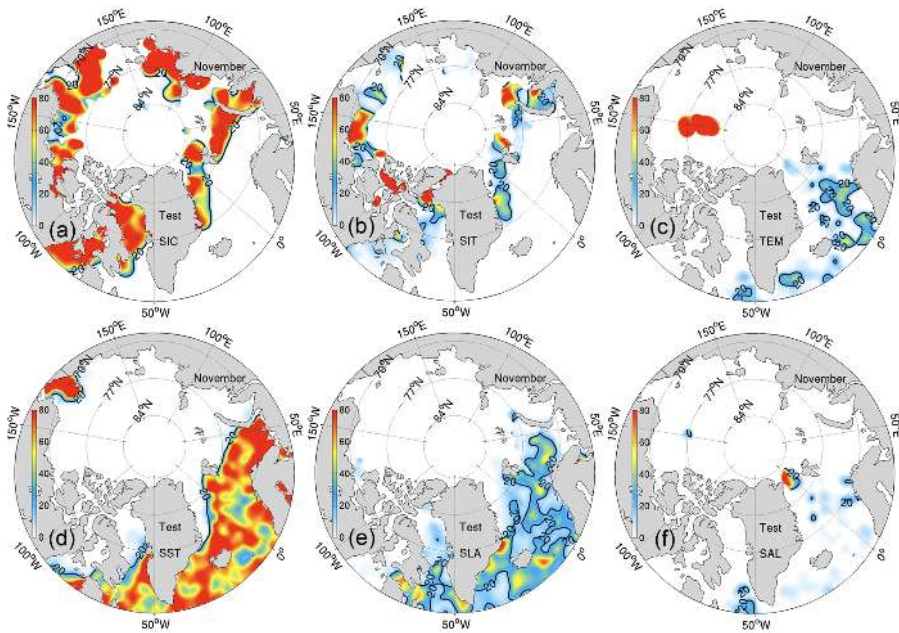


**Figure V.9.:** Same as Figure V.8 but for November 2014.

derived from a combination of SMOS and CryoSat-2 will be soon available (Kaleschke et al., 2015). Incidentally, the US Navy Arctic Cap Nowcast/Forecast System (ACNFS) is currently testing the assimilation of a combined sea ice thickness product (personal communication from David Hebert) where the sea ice thickness is blended from SMOS-Ice and CryoSat-2 based on each satellite retrieval error.

## VI GEOPHYSICAL NOISE

*Georg Heygster and Catalin Patilea*

### VI.1. Introduction

Microwave radiation is defined as being electromagnetic radiation within the frequency range of 300 MHz-300 GHz. Its initial use in remote sensing was for extraterrestrial measurements. For terrestrial investigations microwave remote sensing is used due to its capability to penetrate clouds and is unaffected by rain cells at lower frequencies. The SMOS (Soil Moisture and Ocean Salinity) sensor works at 1.4 GHz frequency, at the low end of the microwave spectrum. The central frequency of the sensor is at 1.413 GHz (L-band) with a 19 MHz bandwidth. The spectral window 1.400-1.427 GHz is restricted to part of L-band because it contains the hyperfine transitions of the neutral hydrogen making it an important area of interest for astronomy. This should have kept contamination of SMOS from ground emitters to a minimum.

Although the low frequency should make surface parameters retrieval (ocean salinity, sea ice thickness, etc.) easier due to lack of atmospheric influence there are other sources of error that need to be considered. In this study we consider four error sources that needed investigation for their impact on sea ice thickness retrieval. The first one is the Faraday rotation. This represents a rotation of the polarization vectors when the radiation passes through the ionosphere. The rotation is variable in time and space. Although it doesn't change the total intensity of the radiation, if the retrievals are based on polarization difference, the rotation will have to be computed and corrected for. The second source for errors is represented by discrepancies in the brightness temperature values between ascending and descending overpasses over the same region. These differences can appear due to difference in time between the data acquisition of the brightness temperatures while the surface geophysical conditions (different surface temperature, freezing/melting of sea ice, etc.) have changed, geolocation errors, thermal variation of the instrument or effects resulting from the image reconstruction. The last two error sources are represented by extraterrestrial radiation: galactic noise and sun glint. The galactic noise represents the radiation from the cosmic microwave background (CMB) and the neutral hydrogen and continuum emissions reflected by the Earth's surface into the sensor. Besides the CMB which is constant in time and space, the other two sources are highly variable. Sun glint represents the reflection and scattering of the sun's radiation on the surface into the sensor. Although the sun never appears into SMOS's field of view, due to scattering and the image reconstruction process, the field of view scene can be contaminated by sun glint.

This study focused on these four error sources and their impact on the retrieval of sea ice thickness.

## VI.2. Faraday Rotation

### VI.2.1. Problem Background

#### VI.2.1.1. Ionosphere

The ionosphere represents a part of the upper atmosphere which includes the thermosphere, the upper mesosphere and the lower exosphere extending from around 60 km to 600 km altitude. Here due to the sun's activity and lack of a dense atmosphere, free electrons exist with density high enough to influence the propagation of the electromagnetic waves. The ionosphere has diurnal and seasonal cycles and varies with geographic position. Ionization depends mainly on the sun's activity and is caused by the interaction of the upper atmosphere with high energy radiation (ultraviolet and X-ray) and particles emitted by it.

#### VI.2.1.2. Faraday Rotation

The SMOS mission uses the Microwave Imaging Radiometer with Aperture Synthesis (MIRAS) sensor which works in the L-band (1.4 GHz). Due to its low frequency, the plane of polarization of the microwave radiation signal will suffer a rotation while passing through the ionosphere. The angle of rotation depends on the angles formed by the microwave radiation detected by the sensor and the geomagnetic field of the earth and the state of the ionosphere (electron density). The Faraday rotation angle is Le Vine and Abraham (2000):

$$\Delta\Omega = \frac{\pi}{cv^2} \int v_p^2(s)v_b(s) \cos(\Theta_b(s))ds \quad (\text{VI.1})$$

where  $c$  is the speed of light,  $v$  is the frequency of the microwave radiation,  $v_p$  is the electron plasma frequency,  $v_b$  is the gyro frequency of the electrons in the earth's magnetic field. Also,

$$\cos(\Theta_b) = \cos \Theta \sin I - \sin(\Theta) \cos(I) \cos(\varphi - D) \quad (\text{VI.2})$$

where  $\Theta_b$  represents the angle between the microwave radiation ray and the earth's magnetic field, with  $I$  and  $D$  being the inclination (angle made by the magnetic field lines with a horizontal line relative to the earth's surface) and declination (angle made by the magnetic field lines on the horizontal plane relative to the true geographic north) of earth's magnetic field, while  $\Theta$  and  $\varphi$  represent the polar coordinates of the line which connects the satellite sensor to the observed ground point. A simplified version of equation VI.1 is used in the SMOS processing chain to compute the Faraday rotation Zundo et al. (2010):

$$\Delta\Omega = 6950 \cdot B(400) \cdot [-\sin El \cdot \sin I + \cos El \cdot \cos I \cdot \cos(Az - D)] \cdot \frac{1}{\cos(90 - |El|)} \cdot VTEC \quad (\text{VI.3})$$

here  $Az$  and  $El$  represent the azimuth and elevation of the ground target point to satellite,  $B$  is the geomagnetic field strength at 400 km altitude, measured in Tesla (T), and  $VTEC = \int N_e(z)dz$  which represents the Vertical Total Electron Content as an integral of the electron density over the whole height beneath the sensor<sup>1</sup>, measured in VTECU (VTEC Units) equivalent with  $10^{16}$  electrons/m<sup>2</sup>. The elevation is  $90 - \Theta$  in a flat earth approximation, which

<sup>1</sup>Total Electron Content (TEC) represents the total number of electrons integrated between two points, VTEC and TEC will be use interchangeably

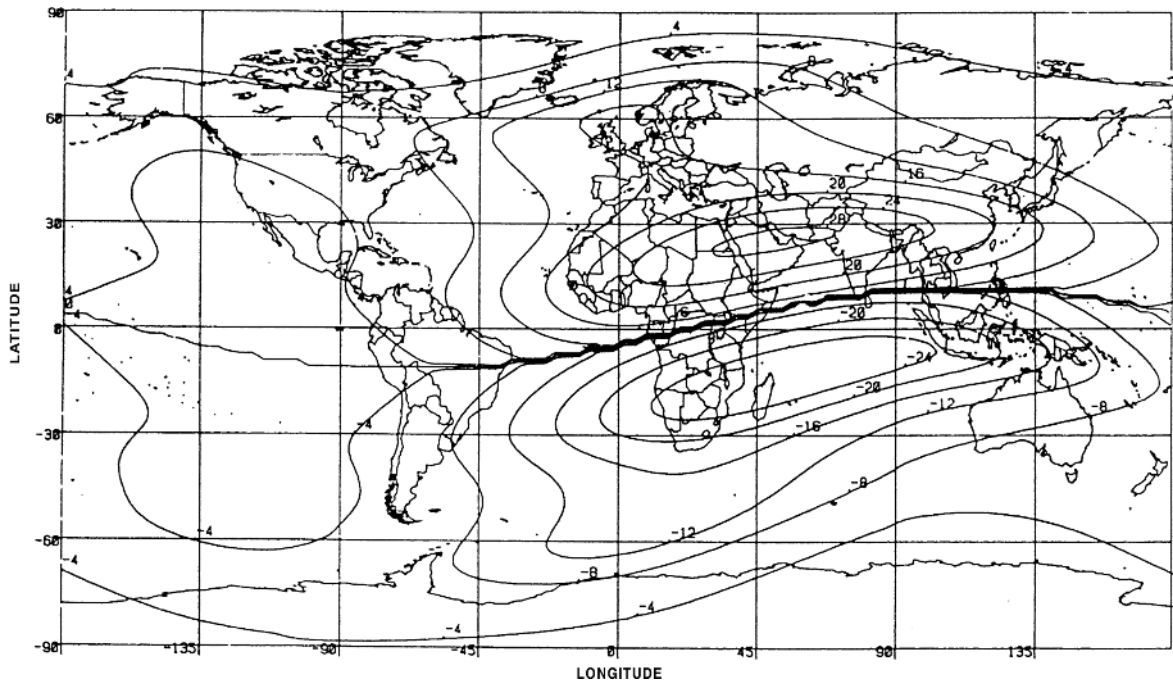


**Figure VI.1.:** Modeled one way ionospheric Faraday rotation at 1.4 GHz for 20 March (equinox) 12:00 UTC. Ground incidence angle 50 deg, azimuth worst case. Values in degrees Svedhem (1986).

means that the curvature of the earth is not taken into account. Thus the normal direction of the satellite nadir point and the ground target point are the same. A single magnetic field a single vector containing B, D and I is used in computing of the Faraday rotation for each snapshot, considering that the variability over the area of the snapshot is small enough to be neglected. The optimal value considered is taken at 400 km altitude, where the error induced by the variation of the magnetic field strength with altitude is minimal. The VTEC is also considered to be constant over the field of view of the snapshot. Thus the variation of the Faraday rotation angle for each pixel within a snapshot comes from the variation of the polar coordinates.

We see from Eq. VI.3 that the Faraday rotation depends on three parameters. The first two are the angle between the microwave radiation registered by the sensors and the geomagnetic field of the earth (I, D) and the field intensity. The third one is the state of the ionosphere represented by the VTEC. The ionosphere state is highly variable and it depends on the geographic location, time of day, season and sun activity. To minimize the values of the Faraday rotation at lower latitudes, the SMOS orbit was designed as a polar and sun-synchronous one with the ascending and descending node at 6 am, respectively 6 pm. At 6 am the total electron content of the ionosphere is at a minimum. An example of values for the Faraday rotation can be seen in Figure. VI.1. The highest values (maximum predicted 28°) appear close to the equator and tropics while at high latitudes they are at most 14°.

## VI.2.2. Data sources and error estimates

### VI.2.2.1. Total Electron Content / VTEC Data

The two sources Crapolicchio (2008) for Vertical Total Electron Content data within the SMOS data are:

- a) VTEC data files provided by the International GPS Service (IGS) as a combined product

	Mean (TECU)	Std (TECU)
IGS final	Reference	Reference
CODE final - IGS final	0.59	1.15
CODE rapid - CODE final	0.57	0.76
CODE forecast - CODE final	0.78	1.3
CODE forecast - IGS final	<0.98	<1.74
IRI2001 sim - IGS final	0.37	3.45

**Table VI.1.:** Mean difference and standard deviation computed for 2005 DOY-238 6AM local time for first three rows, 2004 DOY 5 and 2004 DOY 185 6AM local time for the last two

or from the five Ionosphere Associate Analysis Centers (IAACs)

b) VTEC data resulted from computations done with the IRI2001 model available from NASA

The global VTEC maps provided by the IGS use dual-frequency GPS data from stations and satellites. The five IAAC contributing maps are:

- Center for Orbit Determination in Europe (CODE), University of Berne, Switzerland
- Geodetic Survey Division of Natural Resources Canada (NRCan/EMR), Ontario, Canada
- European Space Operation Center (ESOC) at the European Space Agency (ESA), Darmstadt, Germany
- Jet Propulsion Laboratory (JPL), Pasadena, USA
- Group of Astronomy and Geomatics, Universidad Politecnica da Catalunya (gAGE/UPC)

The IAAC maps are computed using different algorithms provided in a standard resolution 2 hours, 2.5 degrees and 5 degrees for UT, latitude and longitude. The individual IAAC products are available with a delay of 4-8 hours after sensing time while the combined 'rapid' product is available after 10-12 hours. The final consolidated product from IGS combines the final individual products using weights provided by two Ionosphere Associate Validation Centers. A 1-day forecast product is also available from CODE.

The IRI2001 model data is used as a backup solution in case there are no files available from IGS or IAACs. Since this is a climatological model the day-to-day variations will not be well reproduced Flourey (2007).

For the period 01.06.2013-30.12.2013 and the 27.02.2014 day all the SMOS L1C data files (215 days) used for Sea Ice Thickness (SIT) retrieval (Huntemann et al., 2014) used auxiliary VTEC map data from forecasts. The extra 2014 day was selected because it has the highest VTEC values for that year and should also represent the 11 year solar cycle peak.

Results from Flourey (2007) are summarized in Table VI.1, take the IGS final consolidated maps as reference, due to the smaller errors contained, and compute the accuracy of the other products. These accuracy results are computed for 6 AM local time interpolated VTEC maps which are valid mainly for equatorial and mid latitudes but not for the high latitudes which are the regions of interest for this report. The maps provided by the IAACs and IGS represent the Total Electron Content below the GPS. These are corrected for the SMOS satellite altitude using:

$$VTEC_{IGS}^{C,800Km}(\phi, \lambda) = VTEC_{IGS}(\phi, \lambda) \cdot [(A \cdot F_S + B) + C \cdot \cos(D \cdot \phi \cdot \frac{\pi}{180})] \quad (VI.4)$$

where A, B, C and D are coefficients derived from NeQuick model simulations (which provide vertical profiles of electron content at high altitudes) and the  $F_S$  is the solar flux and is extracted from auxiliary files from NOAA's Space Weather Prediction Center,  $\phi$  and  $\lambda$  represent the latitude and longitude.

The validation of the correction using the RA-2 sensor on Envisat showed that this correction reduces the bias of the TEC maps for the worst case from 7 TECUs to 2 TECUs while the standard deviation remains 7 TECUs.

#### VI.2.2.2. Geomagnetic Field/IGRF data

The International Geomagnetic Reference Field (IGRF) model Finlay et al. (2010) is used to compute the Earth's magnetic field strength, declination and inclination parameters necessary for obtaining the Faraday rotation angles for the SMOS data. A new generation of the model is released every five years. For the period 2010-2015, the eleventh generation model was used.

The model represents the low frequency, earth core generated, large scale part of the Earth's magnetic field between 1900 AD and present. The geomagnetic field  $B = -\nabla V$  where V is the scalar potential represented as a finite series of Gauss coefficients. These coefficients are provided for the main field at each five years starting from 1900. The model's coefficients are divided in three parts:

- the current epoch coefficients IGRF yyyy
- definite DGRF coefficients which replace the previous main fields in cases in which it is considered that the coefficients cannot be improved anymore
- the secular variation coefficients which are used for forecasting the following five years of the current epoch.

For time points positioned between the main fields the coefficients are computed using a linear interpolation between them. The secular variation values are computed directly from the last main field and the predicted change of the coefficients.

The variability of the geomagnetic field of the earth is high. At the surface the strength of the field can vary from 30 000 nT near the equator to almost 60 000 nT close to the poles. The field also varies internally in time with a global rms of 80 nT/year for the secular variation.

Errors in the geomagnetic field are divided into three groups igr:

- errors of commission: the real field is actually different from the modeled one
- errors of omission: just the low spatial frequency field is represented
- contributions that are not modeled

For the current IGRF epoch where we have satellite data we consider errors of 10 nT, while for the secular variation we consider errors of 20 nT/year. The true variation is not linear thus it does not represent well the instantaneous field. There are numerous other sources for the Earth's magnetic field with stronger influence near the surface, such as surface magnetized rocks which contribute between 200 and 300 nT. Also there are many fixed and/or small scale contributors such as buildings, cars, electric cables, etc. For the ionosphere the variation induced by electric currents can range from 20 nT during 'quiet' conditions until 1000 nT during a magnetic storm. Strong magnetic storms have an occurrence of approximately 4 per solar cycle (11 years), totaling 4 days noa.

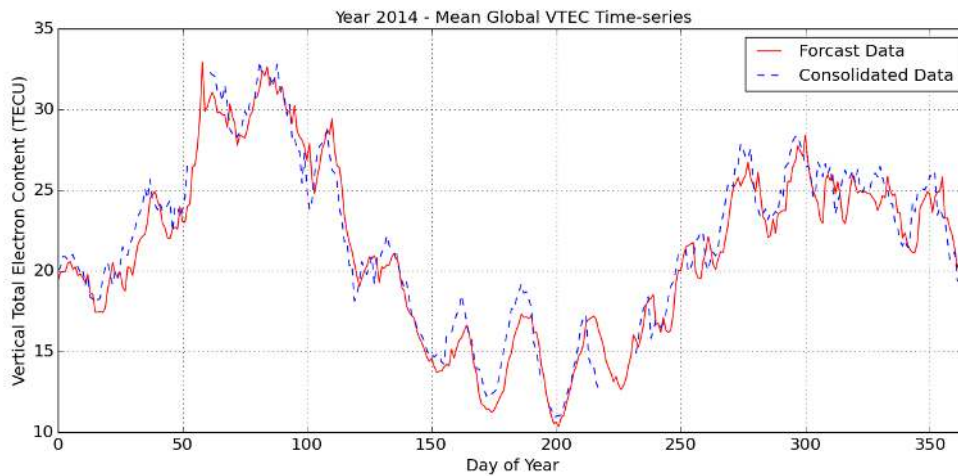


**Figure VI.2.:** Vertical Total Electron Content Global Mean Time-series for 2014

### VI.2.3. Faraday rotation error

We continue by looking at data generated in 2014 with the mention that for the VTEC consolidated auxiliary files, we used just 352 days, the remaining 13 days being either reprocessed files or missing.

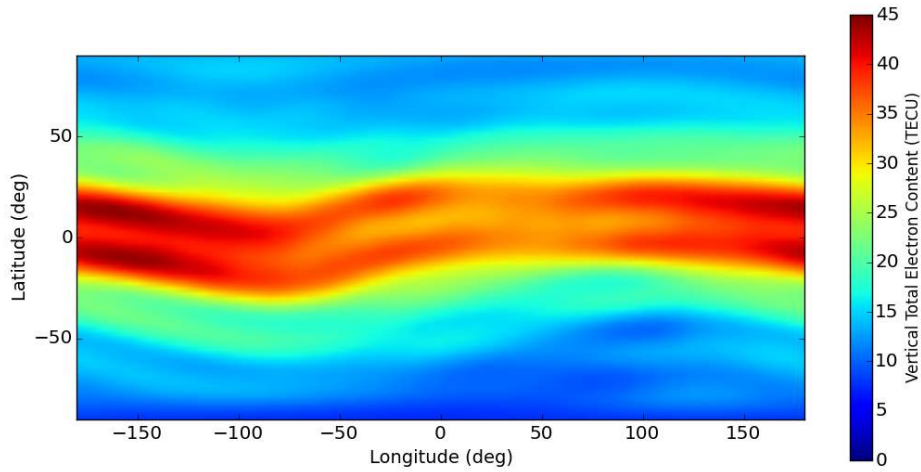
Figure VI.2 illustrates the daily global variation of the mean VTEC values globally in 2014 for both the forecast data provided and the IGS consolidated data. The lowest values (10 TECU) appear in July, while the highest are in February (32 TECU). The mean value for the forecast data is 21.31 TECUs with a standard deviation of 16.7 TECUs. A feature of the VTEC that can be seen in this figure is the seasonal variability. During the autumn and winter the values are higher, while for the summer the values are overall smaller. There is also a smaller variation of approximately 5 TECUs with two peaks per month.

The mean difference between the IGS consolidated data and the CODE forecast data is 0.51 TECUs with the standard deviation being at 1.2 TECUs while the absolute difference is 1 TECU. The forecasts underestimate the TEC values overall, with the bimonthly increase starting earlier in the IGS consolidated date compared to the forecasts.

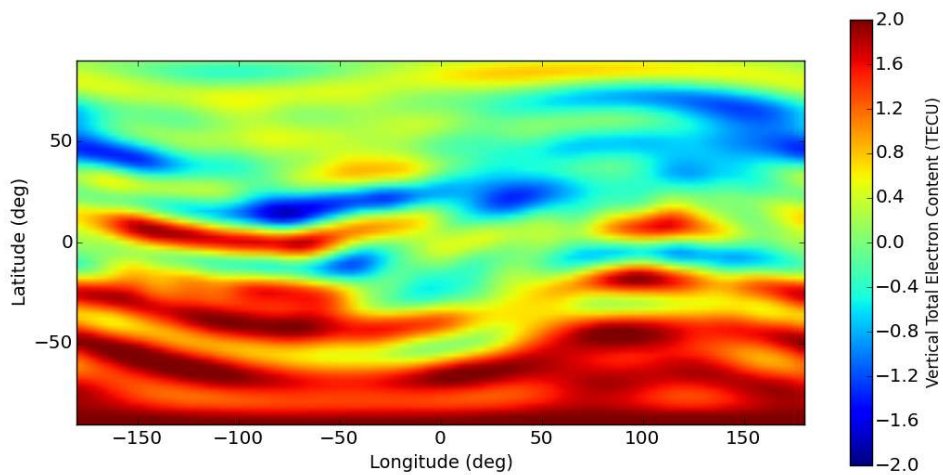
We can see from Figure VI.3 that the mean yearly values at high latitudes are much smaller ( $\leq 20$  TECUs) than at the equator and mid-latitudes. The standard deviation of areas at latitudes higher than  $\pm 50^\circ$  is smaller than 10 TECUs. The lower latitudes show more dependents on the diurnal cycle.

Figure VI.4 shows that the differences between the consolidated and forecast data is much higher in the southern hemisphere with a mean value of 1.5 TECUs, compared with the northern hemisphere where the values reach just 0.5 TECUs. The differences represent less than 20% of mean value in the worst case, while as mention before the asymmetry between the two hemisphere will result in worse accuracy for the Antarctic region.

Figure VI.5 confirms the previous conclusion that although there is a higher variability of the TEC difference at the equator and mid-latitudes, the difference between the two datasets is closer to zero at low latitudes. In the Arctic we have both low difference and low variability, while in the Antarctic we have the highest bias and a higher variability. For further investigation the day with the highest mean value and solar activity was selected (27 February 2014, Day 58) as seen in Figure VI.6. Like in Figure VI.3 the highest mean values and daily variability appear around the equator due to higher impact of the diurnal cycle on the



**Figure VI.3.:** Mean VTEC forecast map for 2014 values are in TECUs



**Figure VI.4.:** Mean VTEC difference between the consolidated and the forecast dataset for 2014.

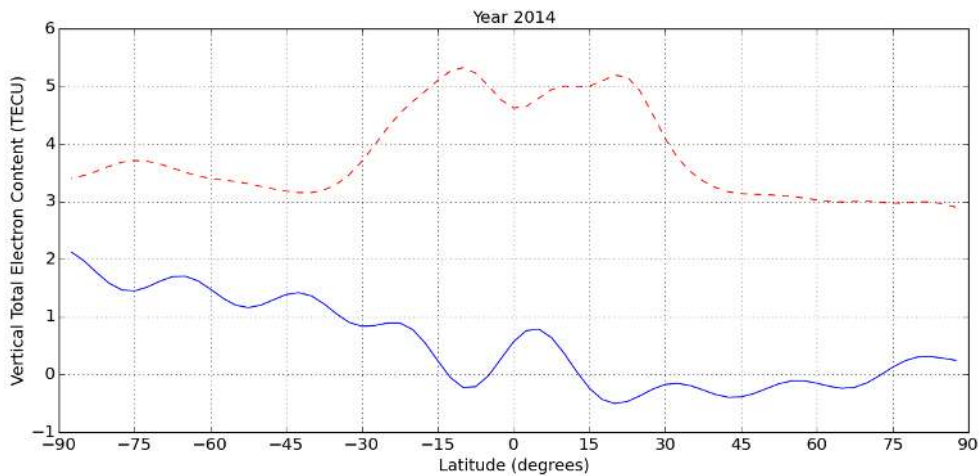


**Figure VI.5.:** Zonal mean (blue) and standard deviation (red) difference between the consolidated data and forecast data in 2014.

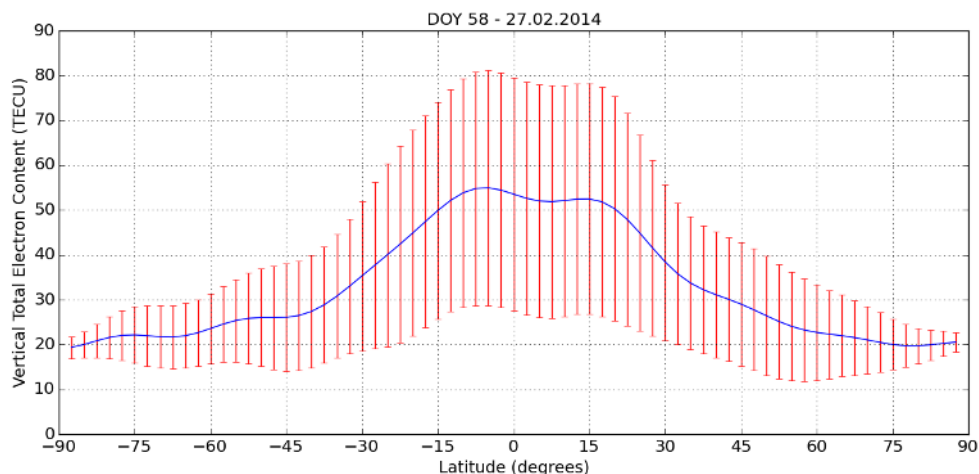


**Figure VI.6.:** Vertical Total Electron Content zonal mean and standard deviation for 27 February 2014.

ionosphere. For both poles the average TEC stays below 25, while the standard deviation is 10 TECUs.

Figure VI.7 shows the mean latitudinal TEC values for 27 February 2014 at four different times of day at six hours differences for longitude 0. The highest values for TEC are during the day, the smallest values for the Northern hemisphere are at 06:00, while for the Southern hemisphere the minimum values appear at midnight.

Due to the polar sun-synchronous SMOS orbit, the satellite sees the latitudes at approximately the same local time at each passing. The ascending and descending nodes are set at 6 am, respectively 6 pm, so for the Arctic the approximate overpass time is 12:00 while for the Antarctic it is 00:00. For the Arctic overpass the maximum TEC values are achieved. For a more accurate analysis an interpolation of the TEC maps at the local time should be done.

For comparison, Figure VI.8 shows the same as Figure VI.7 only for 26 August 2014. It should be noted that the figure y scales are different. While the overall values have decreased, the differences between the two poles stand out. For the Arctic the values vary around 20 TECUs, while in the Antarctic, 2.5 TECUs.

In Figure VI.9 we can see that for both poles there is a seasonal variation of TEC, with high

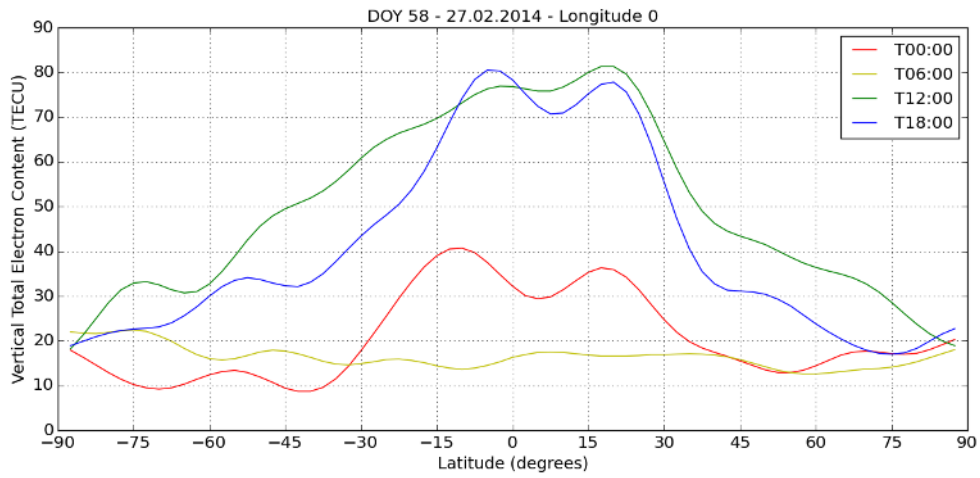


Figure VI.7.: Vertical Total Electron Content for 27 february 2014 at longitude 0 taken from the forecast auxiliary file.

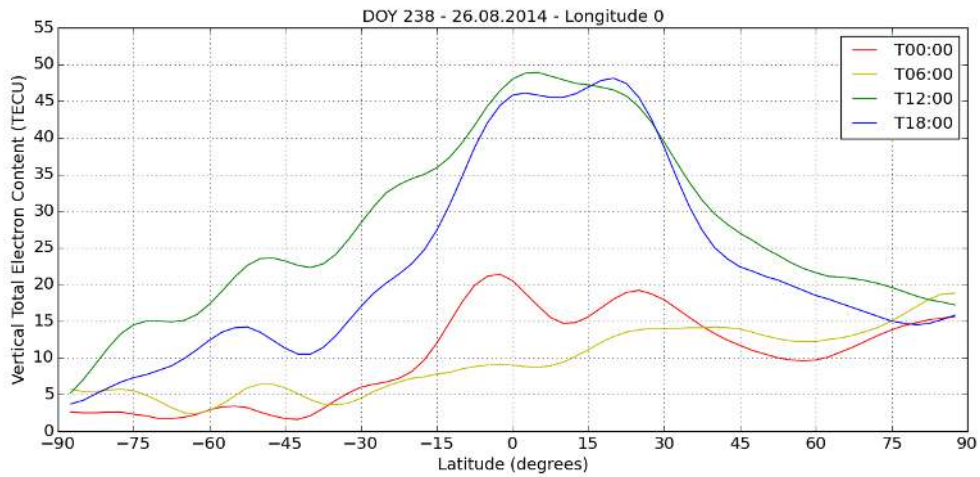


Figure VI.8.: Vertical Total Electron Content for 26 August 2014 at longitude 0.

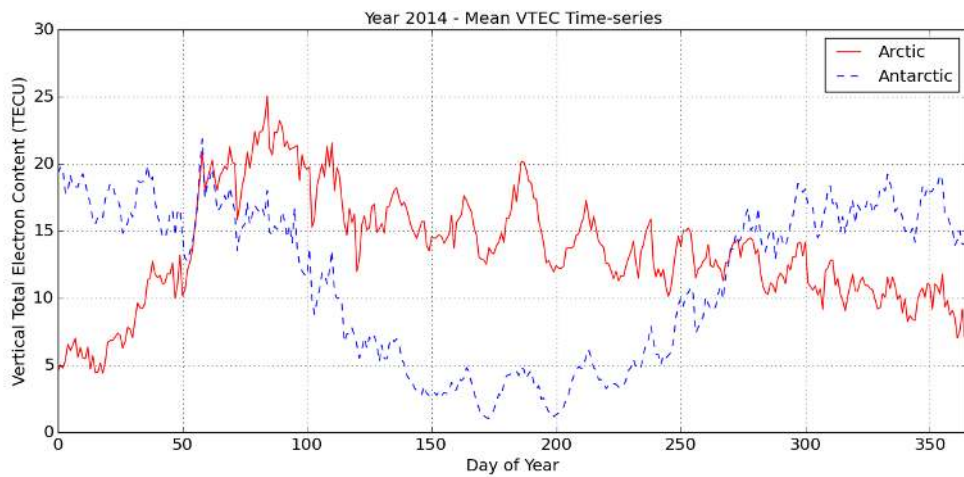


Figure VI.9.: Mean Vertical Total electron Content Time-series for  $> 60^{\circ}\text{N}$  and  $< 55^{\circ}\text{S}$  from the forecast data.

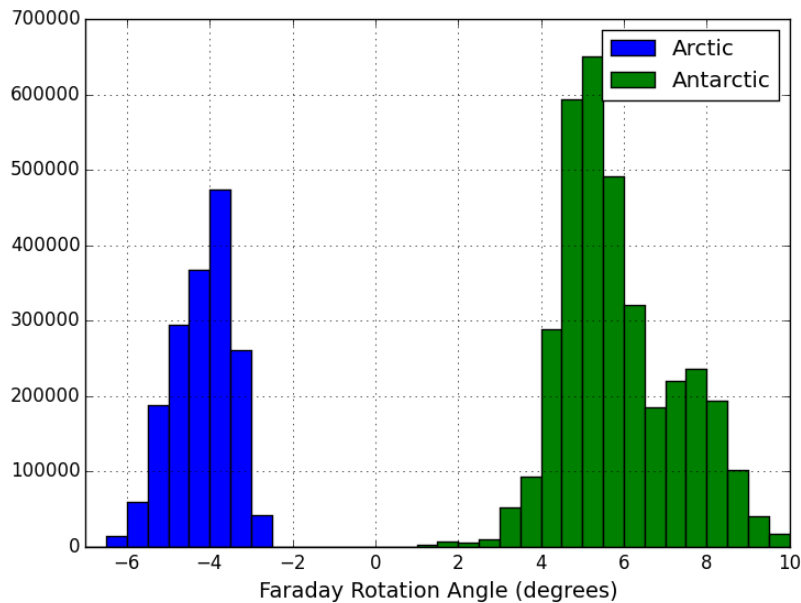


Figure VI.10.: Histogram of Faraday rotation angles from 27 february 2014 taken from LIC SMOS data.

values during February-March in the Northern hemisphere, while in the Southern hemisphere we have high values from november until february.

In conclusion the Arctic has on average higher mean values for the TEC and they are more stable, while in the Antarctic the average TEC mean is smaller but it has larger seasonal variability. Without taking into account the geomagnetic field vector this should mean higher Faraday rotation values on average for the Arctic due to the higher TEC. The overall higher TEC values in the consolidated data for the Antarctic relative to the forecasts used in the LIC dataset will result in a higher Faraday rotation error for this area.

In Figure VI.10 we show the Faraday rotation histogram in bins of  $0.5^\circ$  for 27 February 2014 for all grid points north of  $60^\circ\text{N}$  and south of  $55^\circ\text{S}$ . Data points with incidence angle between  $40^\circ$  and  $50^\circ$  have been selected. For filtering RFI, a maximum threshold of 300 K has been used so that any snapshot containing at least one brightness temperature over the threshold will be completely removed. Most data is under  $10^\circ$  of absolute rotation, with Arctic average of  $-4.2^\circ$  and  $5.9^\circ$

#### VI.2.4. Brightness Temperature error

In Figure VI.11 we show the histogram of  $\Delta Q$  differences between the datasets for 27 February 2014, computed taking in account the Faraday rotation and without it. For the Arctic, 95% of the data points have an error smaller than 2 K, while in the Antarctic we have 62%. This was done just for incidence angles between  $40^\circ$  and  $50^\circ$ . This was computed as an extreme case in which we have completely neglected Faraday rotation and then compared the resulted brightness temperatures with the ones included in the LIC data (forecast TEC maps). The actual errors in brightness temperature as a result of Faraday rotation errors due to inaccuracies in TEC map data or in the IGRF model are in the 1 K range.

As an example for a TEC equal to 20 TECUs, B equal to 40000 nT we obtain  $5^\circ$  of Faraday rotation. Taking  $(T_{Bh}, T_{Bv}) = (206, 234)$  K as sea ice brightness temperature, after the Faraday rotation transformation the  $T_b$  will be  $(T_{Bh}, T_{Bv}) = (206.21, 233.79)$  K. For an

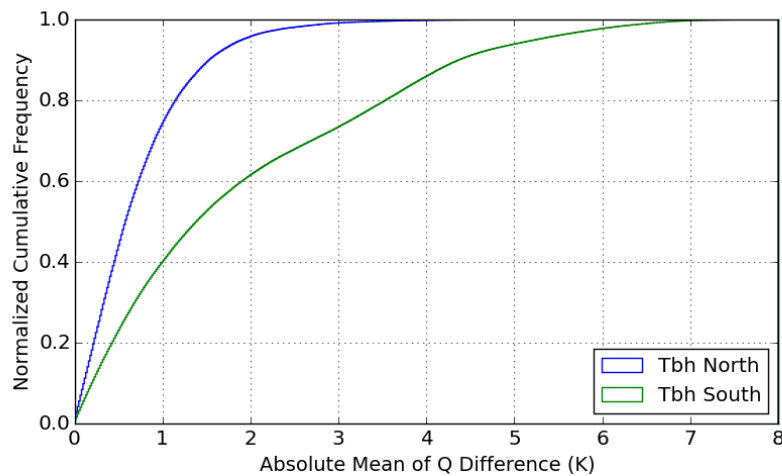


**Figure VI.11.:** Histogram representing the absolute mean  $\Delta Q$  between the dataset with Faraday rotation taken into account and without it.

error of 2 TECUs and 5 nT, the rotation error is  $0.5^\circ$  which will translate into less than 0.5 K of polarization difference relative to the old value.

At low incidence angles ( $0 - 40^\circ$ ) only intensity is used for SIT retrieval. The intensity remains the same regardless of the the Faraday rotation thus the retrieval is not influenced.

### VI.2.5. Sea Ice Thickness error

The difference in SIT in the retrieval algorithm of (Huntemann et al., 2014) with and without the Faraday rotation correction is investigated on 2014-02-27 for the Arctic as an example of a day with high TEC. The average SIT difference is below 1 cm, the RMS difference 1.5 cm. From this example with the highest solar activity day of 2014, and close to the highest for the Arctic we conclude that the Faraday rotation does not change systematically the SIT retrieval and the statistical change is below 1 cm.

In Figures VI.12 and VI.13 we consider just the areas with SIT below 50 cm. The extreme case taken here still gives errors smaller than 3 cm which is within the error estimates for the retrieval (Huntemann et al., 2014).

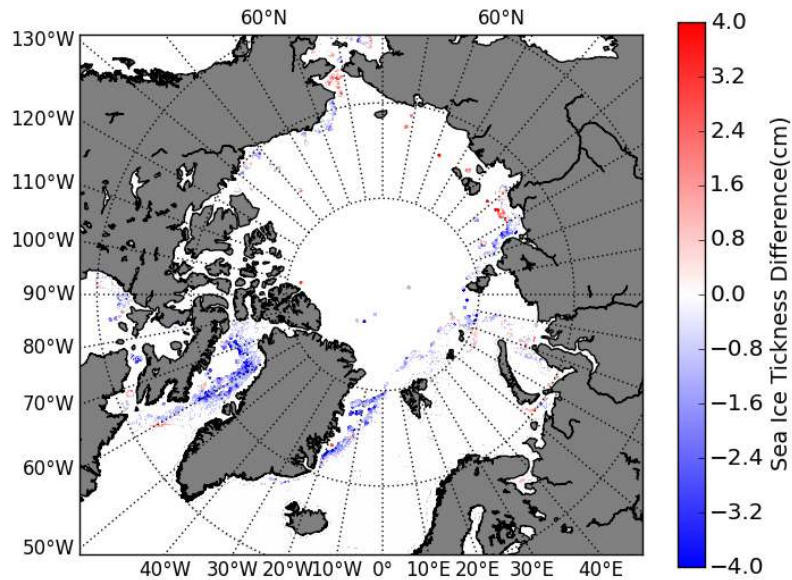


**Figure VI.12.:** Sea Ice Thickness difference computed between the dataset that uses the Faraday rotation and without (2014-02-27).

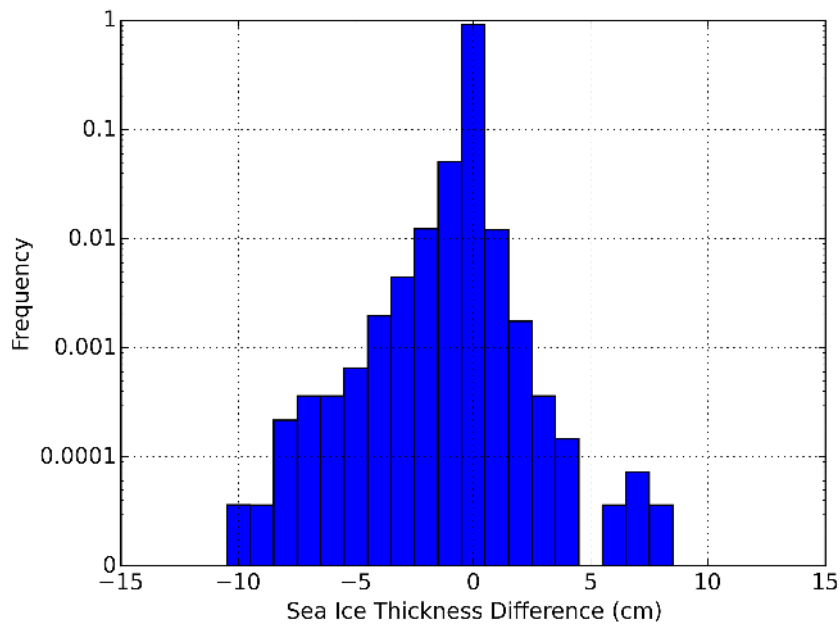


**Figure VI.13.:** Histogram of the Sea Ice Thickness difference in the Arctic computed between the dataset with Faraday rotation included and without for 2014-02-27.

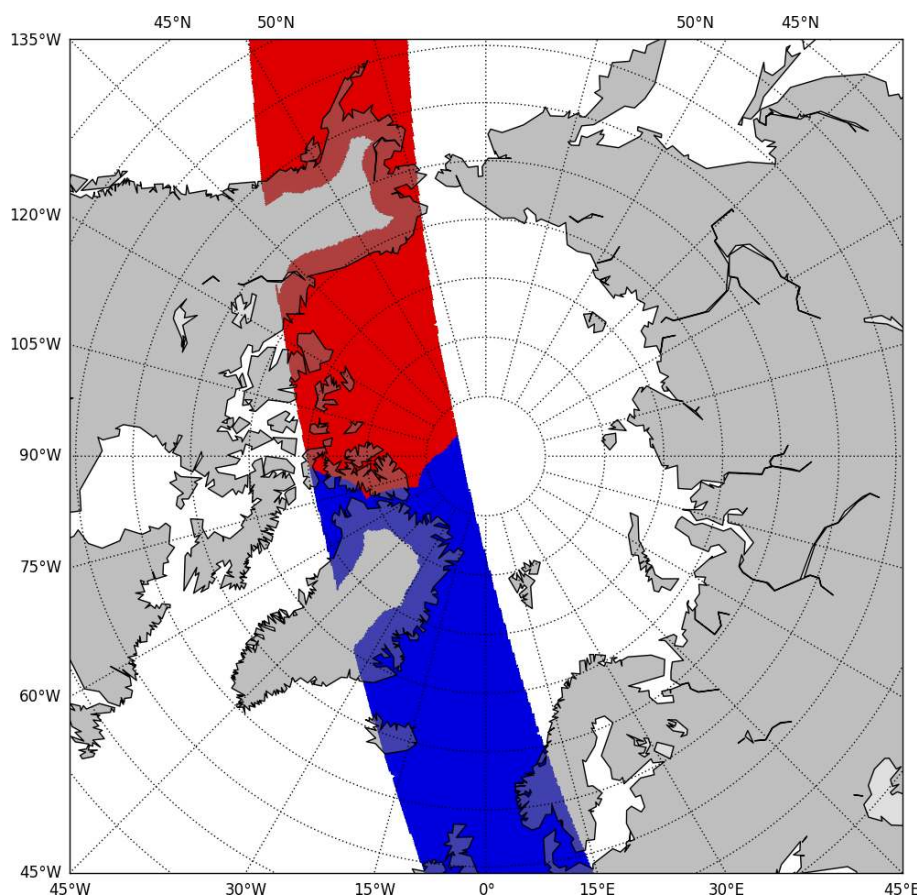


**Figure VI.14.:** Map showing boundary between two consecutive semi-orbits in the Northern Hemisphere taken on 19.12.2014. Blue: ascending semi-orbit, red: descending part.

## VI.3. Ascending/Descending Node Inhomogeneities

### VI.3.1. Problem Background

In this section we check for discrepancies in brightness temperatures between ascending and descending overpasses in polar regions and their influence on the sea ice thickness retrieval.

A SMOS overpass is identified by its orbit number, while the ascending and descending sections of the orbit are organized in separate files (swaths). Ascending swaths (semi-orbits) overpass the equator northward. The semi-orbit boundary is defined as the change in sign of the vertical velocity of the spacecraft in the Earth Fixed Reference Relloso and Zapata (2010). The data cutting/consolidation algorithm for two consecutive swaths is described in Barbosa (2012). The first snapshot of a swath at the boundary is used to decide which grid points are part of the current semi-orbit, while the last snapshot is used to filter out the grid points of the preceding half-orbit. The algorithm uses snapshots from the next semi-orbit to fill in data for the grid points which are part of the current semi-orbit, and snapshot from the previous semi-orbit to do the same for grid points part of the current semi-orbit. This will give close to the border grid points containing the whole range of incidence angles available. Figure VI.14 shows two consecutive swaths taken from the L1C Full Polarization Sea Science product.

The analysis was done on two data sets:

- the first case uses data from the L1C product (version 5.05) from which we selected four separate weeks of data centered on the 2014 equinoxes (spring: 17-23 march; autumn: 19-25 september) and solstices (summer: 18-24 june; winter: 19-25 december). The swath based differentiation between ascending/descending was done using the ascending flag metadata from the L1C files.
- Second, we analyze five years of data (2010.06.01-2015.05.31) for which we use an intermediate data product in which differentiation between ascending and descending swaths flag wise was not possible. The intermediate data product is used at Uni-Bremen for the SIT processing in order to save data volume. A snapshot based restrictions was used to identify ascending and descending overpasses. The snapshot number restrictions were determined after the analysis of one week of L1C data.

The reason for using an intermediate product is due to storage requirements, bandwidth and availability. One day of intermediate data needs as much space as just one swath of L1C data, thus decreasing the space required by almost 30 times and is already available on local storage. The extended timeseries is used to check if the selected four weeks from 2014 are representative for other periods during the year or if they are biased in any significant way. Using L1C data would be optimal due to the ascending/descending flag existence, and because the snapshot based ascending/descending identification introduces some errors. The common periods in both data sets are used for crosschecking.

The algorithm for identifying ascending/descending overpasses in the intermediate data is presented below:

Snapshot IDs are generated from the absolute orbit number  $\times 10000$  + seconds from ANX (Ascending Node Crossing: considered to be equator crossing at local time 06:00 am) Barbosa (2012). We use the absolute orbit number to differentiate between overpasses and the time from ANX to identify ascending and descending semi-orbits. We create two modes (since we know an orbit takes 6003 seconds to complete) which are usable just in the northern hemisphere:

- a restricted mode where the snapshots are only part of one semi-orbit: ascending (4560 to 6003 seconds from ANX) and (0 to 1363 seconds from ANX), descending (1558 to 4364 seconds from ANX)
- a relaxed mode where also the common snapshot of the swaths were included: ascending (4364 to 6003) and (0 to 1558), descending (1363 to 4560)

For the first case the data version used was 5.05, while for the extended timeseries, a total of five years were analyzed (2010.06.01-2015.05.31) with 2010.06.01-2015.05.04 using data version 5.05 and the remaining time using the new 6.20 data version. In the new data version, due to improved calibration, the temporal and latitudinal variations between ascending and descending passes over the ocean for the first Stokes parameter have been reduced; also the average brightness temperature in the field of view is warmer by 1.4 K over ocean, 2.2 K over Antarctica and 2.5 K over land team and 1 (2015).

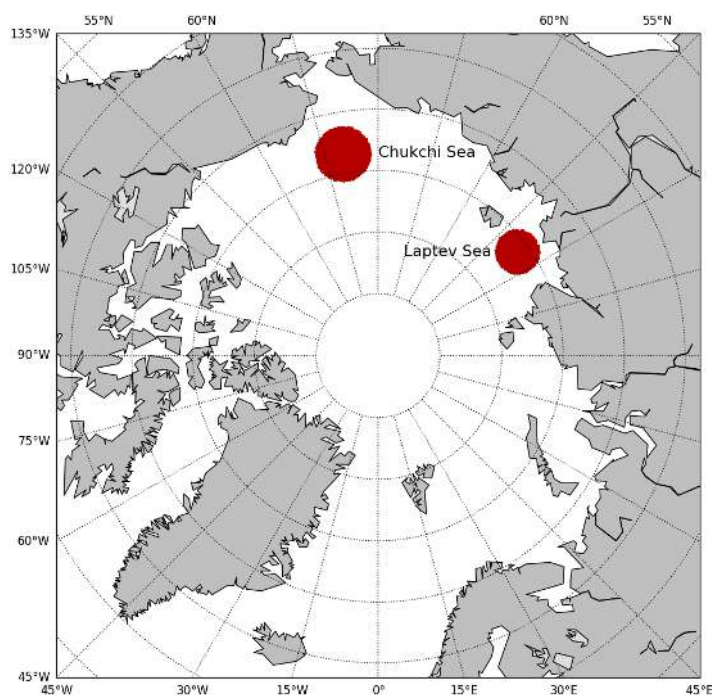


**Figure VI.15.:** The Chukchi Sea and Laptev Sea areas investigated.

The reason for selecting solstices and equinoxes for the initial analysis is that if there is a difference due to geophysical causes (surface temperature, melting, etc) we expect that they will be more pronounced at these time of the year. At the equinoxes grid points on the ascending path were in darkness previously, and on the sun lit part for the descending semi-orbits. During solstices the grid points either were in light or in darkness on both semi-orbits. The four weeks will be used to check if the longer time-series analysis is prone to large errors due to the way ascending/descending snapshots are differentiated.

The two areas investigated are the Chukchi Sea and the Laptev Sea as shown in Figure VI.15.

The Chukchi Sea region is positioned north of the Bering Strait and for the four weeks selected in 2014 the sea ice concentration is either close to 100% or to 0%. The selected area (1006 grid points) is a circle of 250 km radius centered at 73.5°N latitude and 170°E longitude.

The Laptev Sea area was selected as a circle of 200 km radius centered at 76°N, 126.5°E containing 647 grid points. The further north the grid points are located the higher the impact will be from the snapshot based ascending/descending algorithm thus for the Laptev Sea a smaller area is selected.

### VI.3.2. Results

All daily averages are done taking all snapshots from one day for one pixel in the required incidence range. These are divided into ascending and descending snapshots. For the incidence

angle range we separate into two sets: high incidence angle (40-50°), and low incidence angle (0-40°). All the data is filtered for RFI by removing all the snapshots containing at least one pixel with brightness temperature value over 300 K.

### VI.3.2.1. Cross comparison between timeseries

This section presents a comparison between the L1C and the intermediate data sets. This comparison is used to select which of the two snapshot selection modes for the intermediate data set will be used for the investigation of the long time series to minimize the errors generated by the exclusion of snapshots that include grid points in both ascending and descending consecutive swaths.

We investigated the Chukchi Sea, using time periods common to both data sets: the four weeks centered on the 2014 equinoxes and solstices. We compute the daily mean brightness temperature for both ascending and descending swaths at the selected incidence angle range and then compute a weekly mean difference between the L1C data and the intermediate data.

For Tbh Figure VI.16 shows that at high incidence angle the differences are under 0.2 K for the restricted mode in spring and summer. For autumn and winter this gets under 1.5 K. The extended mode has higher differences for all periods. For Tbv we get slightly smaller differences for the restricted mode in all weeks besides winter where the differences reach 0.5 K and are higher than the extended mode. In almost all cases the standard deviation of the brightness temperature differences is smaller for the descending overpass. Also the mean differences are mostly positive for Tbh and mostly negative for Tbv besides winter where the difference is positive.

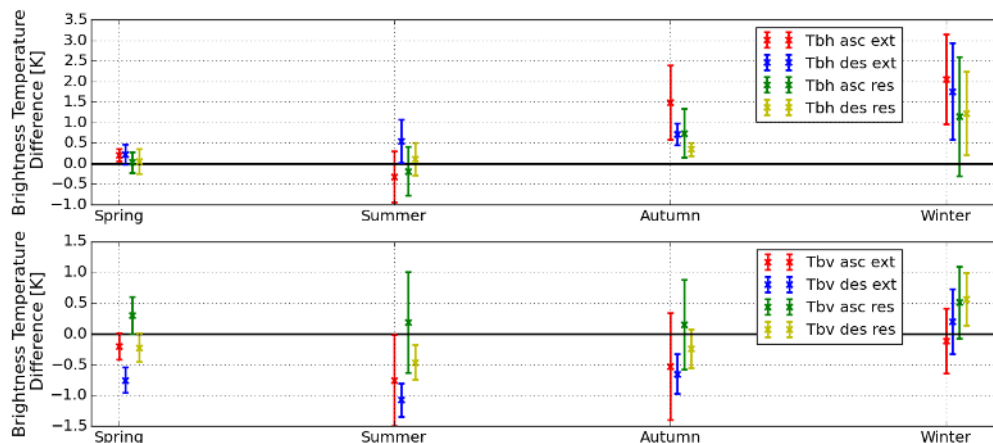
In cases of low incidence angles (0-40°) the differences between the restricted and extended mode are within one standard deviation of the two respective data sets (Figure VI.17) for Tbh. In both cases the biases are almost the same for Tbh and Tbv. Spring again has a small bias and variability with all values under 0.2 K.

As a result of this analysis we decided using the restricted mode only for the long time series where a processing based on the L1C data would take five times more of computation time and would require much more disk space. The errors introduced by using the restricted mode data is in all examined within the standard deviation of the two involved data sets (compare red vs green and blue vs yellow in Figures VI.16 and VI.17)

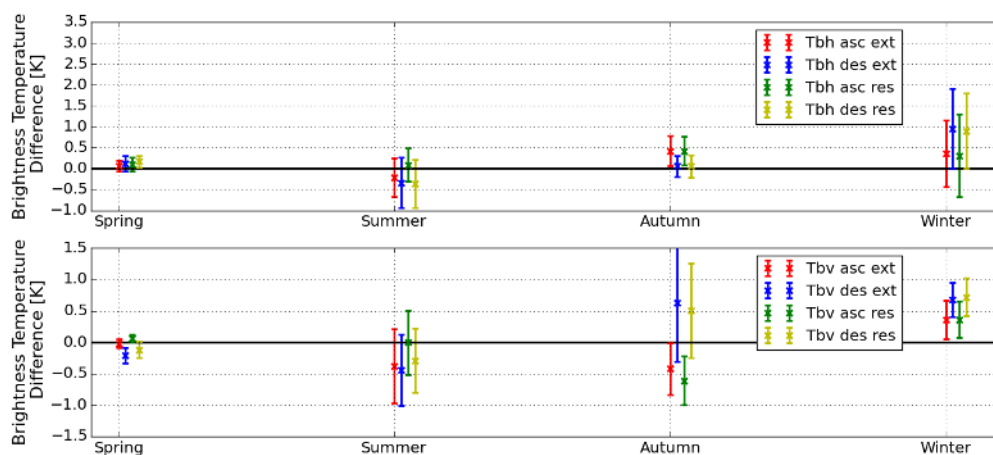
### VI.3.2.2. Data Analysis

Figure VI.18 shows the daily mean ascending and descending brightness temperatures time series together with their differences for the Chukchi Sea at high incidence angle (40-50°).

For the whole time series the mean difference between the ascending and descending overpasses is 1.78 K with a standard deviation of 4.74 K for Tbh and a mean difference of 0.79 K and standard deviation of 3.63 K for Tbv (not shown). The highest variability is seen during the freeze-up and melting periods with slightly positive mean values for both Tbh and Tbv during freeze-ups. In 2014 due to the stability of the sea ice in the area during the spring equinox the difference is small with 0.19 K and 0.28 K for Tbh and Tbv respectively, and standard deviations over 3 K. During periods with almost complete ice cover, mainly



**Figure VI.16.:** Brightness temperature difference of ascending and descending half-orbits between intermediate and LIC dataset in the Chukchi Sea for the selected four weeks of 2014 for Tbh (top) and Tbv (bottom) at high incidence angle (40-50°).



**Figure VI.17.:** Brightness temperature difference of ascending and descending half-orbits between intermediate and LIC dataset in the Chukchi Sea for the selected four weeks of 2014 for Tbh (top) and Tbv (bottom) at low incidence angle (0-40°).

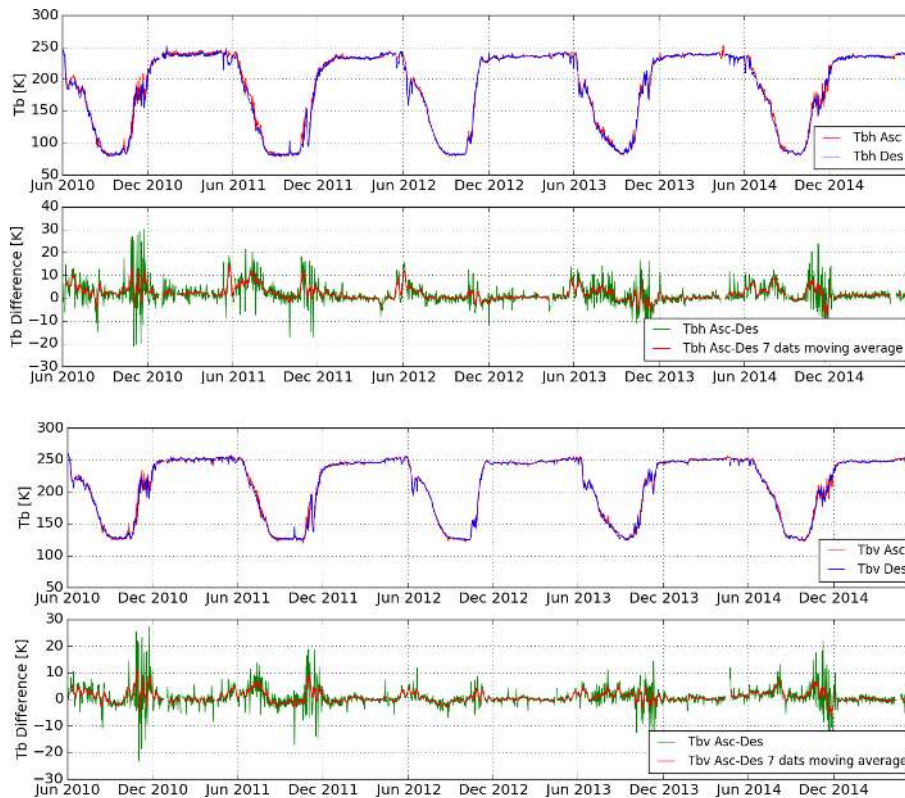
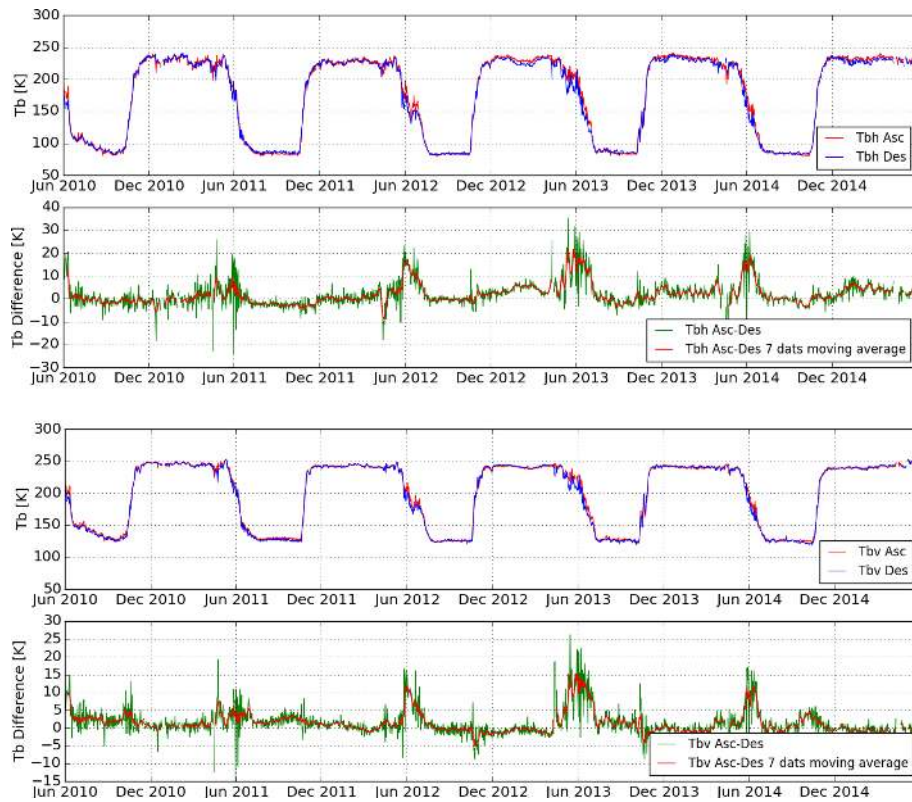


**Figure VI.18.:** Chukchi Sea Ascending/Descending Tbh (first), Tbh Ascending/Descending Difference (second), Ascending/Descending Tbv (third) and Tbv Ascending/Descending Difference (fourth) at high incidence angle for June 2010-May 2015.

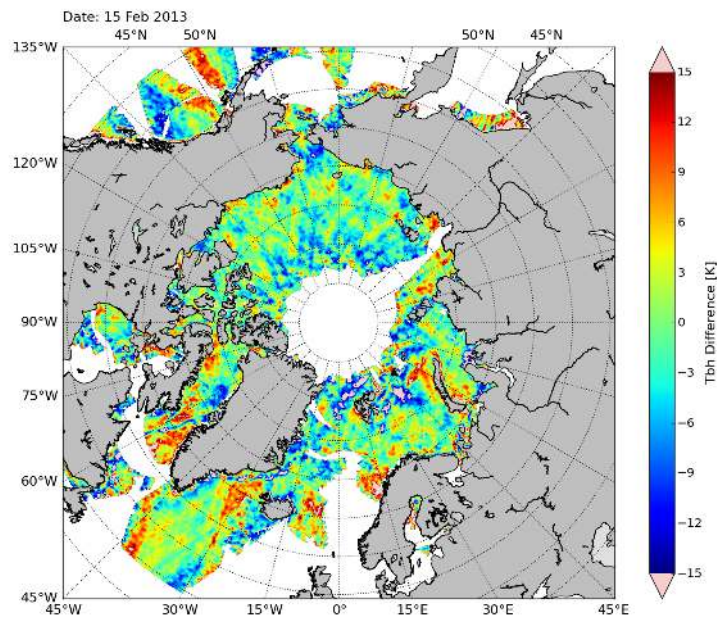
between January and June, the brightness temperature values remain stable for both Tbh and Tbv and the ascending/descending differences remain small.

Figure VI.19 (as in Figure VI.18) shows the corresponding results for the Laptev Sea region. The mean Tbh difference is 1.98 K for the complete time series and 1.40 K for Tbv (not shown). A particular feature of the Laptev Sea is that during January to April of the last three years of the time series the mean difference can get over 5 K. This is the result of a high number of RFI contaminated snapshots being eliminated, mostly for the ascending overpasses, dragging the incidence angle mean towards higher values, resulting in higher brightness temperatures for the ascending overpasses and thus higher brightness temperature differences.

Figure VI.20 shows a mean brightness temperature difference map between the ascending and descending overpasses for 15 February 2013. This date was chosen due to the high bias detected in the Laptev Sea on this day in the previous analysis. Many grid points are not covered by data since the difference can only be determined on grid points that contain data for both ascending and descending overpasses. Moreover it generates a bias in the mean incidence angle towards higher values in the grid points bordering these areas. The resulting mean brightness temperatures are changed according to the dependence on incidence angle: for Tbv it typically increases, and for Tbh it decreases. In the Laptev Sea, on many days RFI contamination is high, especially for ascending overpasses thus removing contaminated snapshots. The remaining snapshots are always the same part of the overpass, creating a bias towards higher incidence angles and in the resulting brightness temperature. Another difference observed for Tbh and less for Tbv (Figure VI.21), is found at the ice edge east of



**Figure VI.19.:** Laptov Sea Ascending/Descending Tbh (first), Tbh Ascending/Descending Difference (second), Ascending/Descending Tbv (third) and Tbv Ascending/Descending Difference (fourth) at high incidence angle for June 2010-May 2015.



**Figure VI.20.:** Tbh Asc - Des daily mean difference for 15 Feb. 2013.

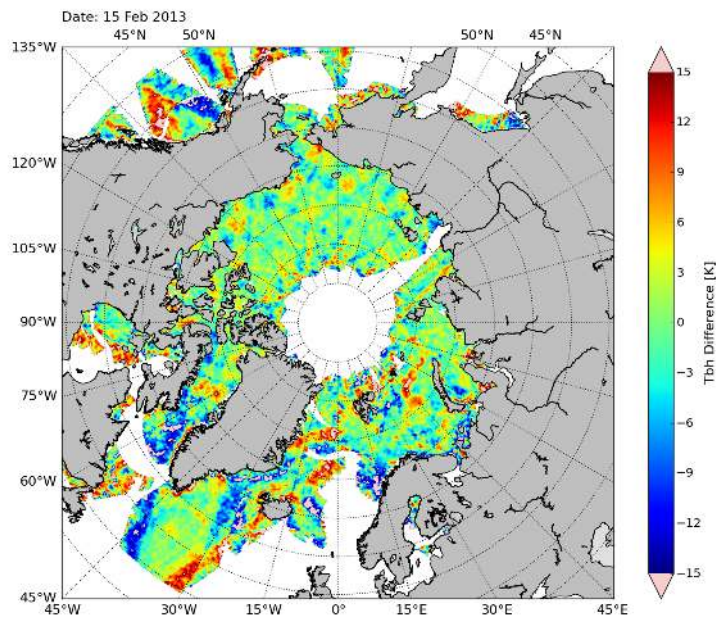


**Figure VI.21.:** Tbv Asc - Des daily mean difference for 15 Feb. 2013.

Greenland, with negative values dominating. This is best visible in the monthly averages in Figure VI.26. This effect is mainly seen in areas with high contrast like the ice edge, where the differences between the ice and ocean brightness temperatures are around 100 K. A similar effect can be seen close to the west Greenland coast and at the northern border area of the Sea of Okhotsk. Here the we have land and ocean and the brightness temperature differences are all positive and over 20 K, while in the East Siberian Sea where we have sea ice close to the coast this effect does not exist.

For intensity at low incidence angles ( $0-40^\circ$ ) we observed the same pattern (Figure VI.22), with differences appearing at the ice edges. The negative values vary from 12 and 18 K with some areas going past 30 K. For comparison in areas mention that in areas away from the ice edges the values vary between -3 and 3 K.

### VI.3.2.3. L1C data version 620 comparison

A comparison between the old 505 L1C data version that is used in the operational processing chain and the new 620 version is conducted. The new data version was introduced during the course of the project. Due to space and processing requirements just one week of data is compared. Figures VI.23 and VI.24 show the horizontal brightness temperature difference for incidence angles between  $40^\circ$  and  $50^\circ$  using the two data versions.

The high difference values that appear around the ice edges are reduced by around 10 K in most areas. In the area around Iceland we can observe that the distribution of positive and negative differences is directional (Fig. VI.23) with most positive values being recorded in the south and south-western area of the island while the negative differences are on the north and north-east for the 505 version. In the 620 version (Fig. VI.24), the differences are reduced but also the pattern is less clear. The same results are seen for vertical brightness

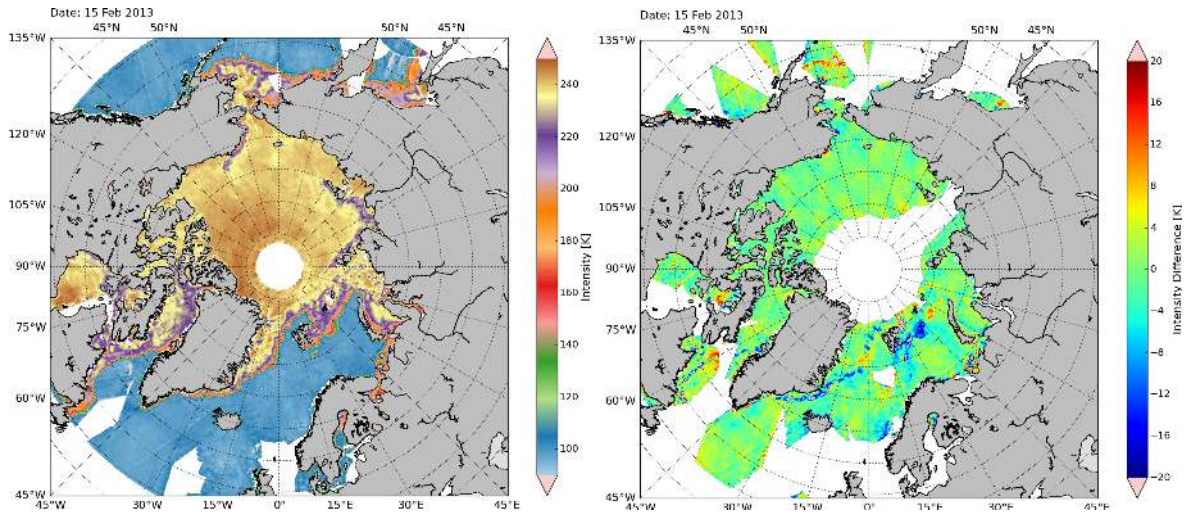


**Figure VI.22.:** Intensity computed using all overpasses (left) and intensity difference between ascending and descending (right) for 0-40° incidence angles for 15 Feb. 2013 .

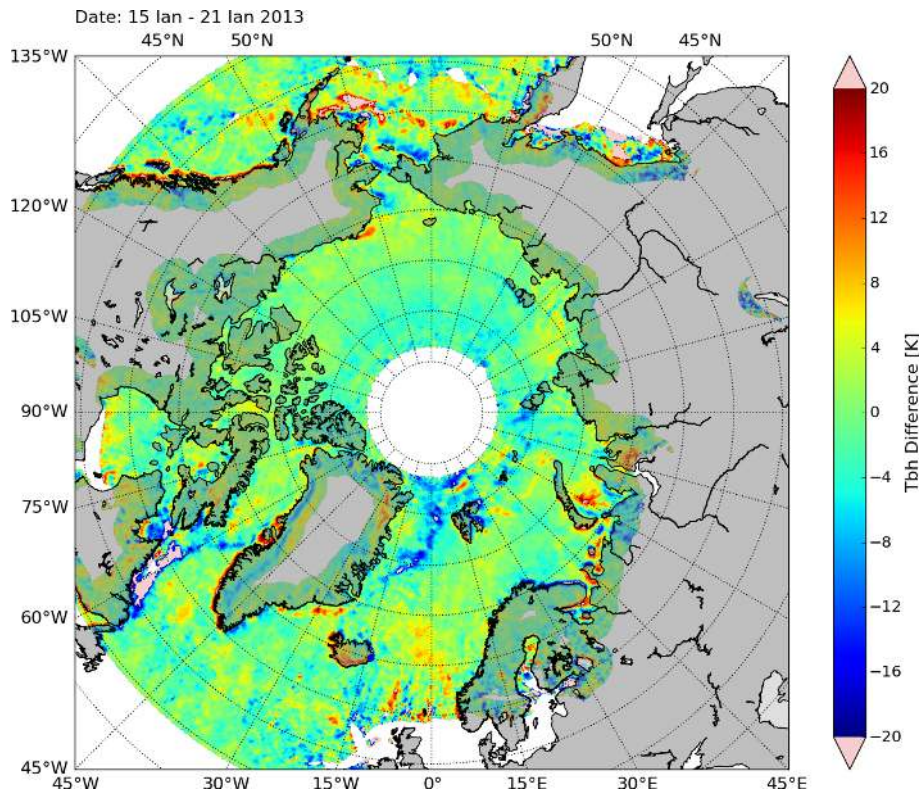


**Figure VI.23.:** Tbh difference between ascending and descending overpasses for 40-50° incidence angles for 15-21 Jan. 2013 using 505 data version.

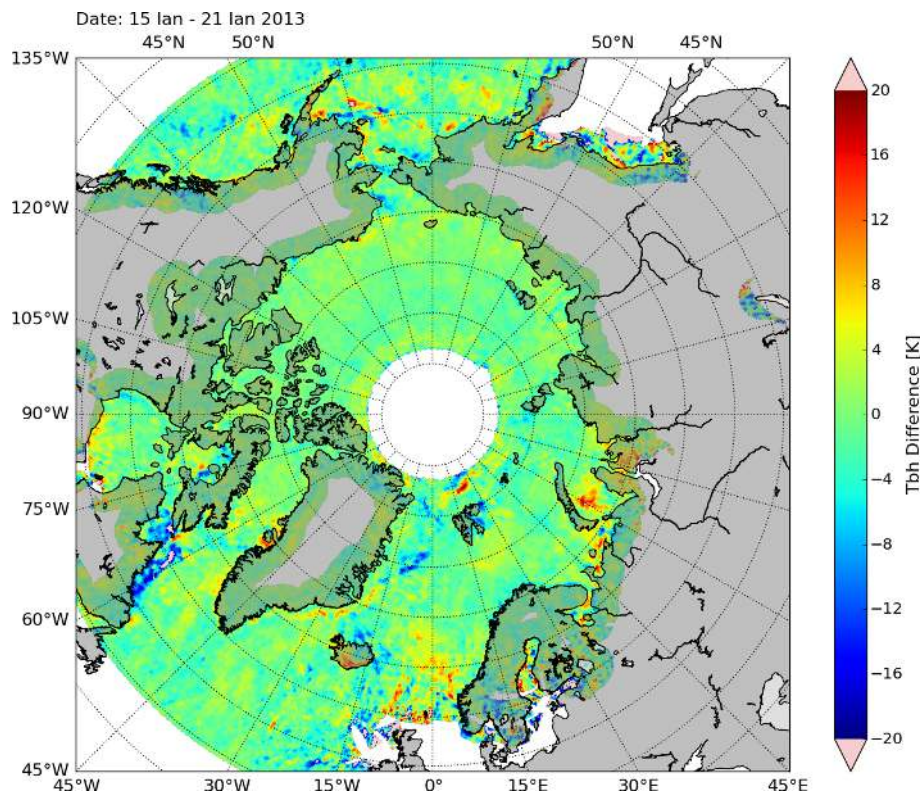


**Figure VI.24.:** Tbh difference between ascending and descending overpasses for 40-50° incidence angles for 15-21 Jan. 2013 using 620 data version.

temperature and for lower incidence angles.

#### VI.3.2.4. Sea Ice Thickness

For the sea ice thickness computation we use the algorithm based on Huntemann et al. (2014). The sea ice thickness is computed in increments of one cm. From Figure VI.25 we observe that the biggest differences appear along the ice edges, and are mostly visible on both sides of Greenland, with values between -4 and -12 cm, with areas below -20 cm. Just like the brightness temperatures, the mean differences may vary locally from day to day but for ice edges the mean bias is negative.

In areas with high RFI contamination (Laptev Sea in Figure VI.25) the change in incidence angle mean can influence the sea ice thickness retrieval result, while this influence at the ice edge relative to the bias generated by either geophysical reasons or satellite geometry/image reconstruction process is small.

#### VI.3.2.5. Discussion and Conclusions

The differences between ascending and descending half orbits (A/D differences) were investigated based on two data sets. For single days, SMOS Level 1C data was used. Due to storage reasons for the full time series of the SMOS lifetime until mid-2015 an intermediate data format produced at the University of Bremen was used. Both data sets show similar results during four weeks located around the equinoxes and solstices of 2014 (Fig. VI.16 and VI.17). The time series of the ascending and descending brightness temperatures averaged

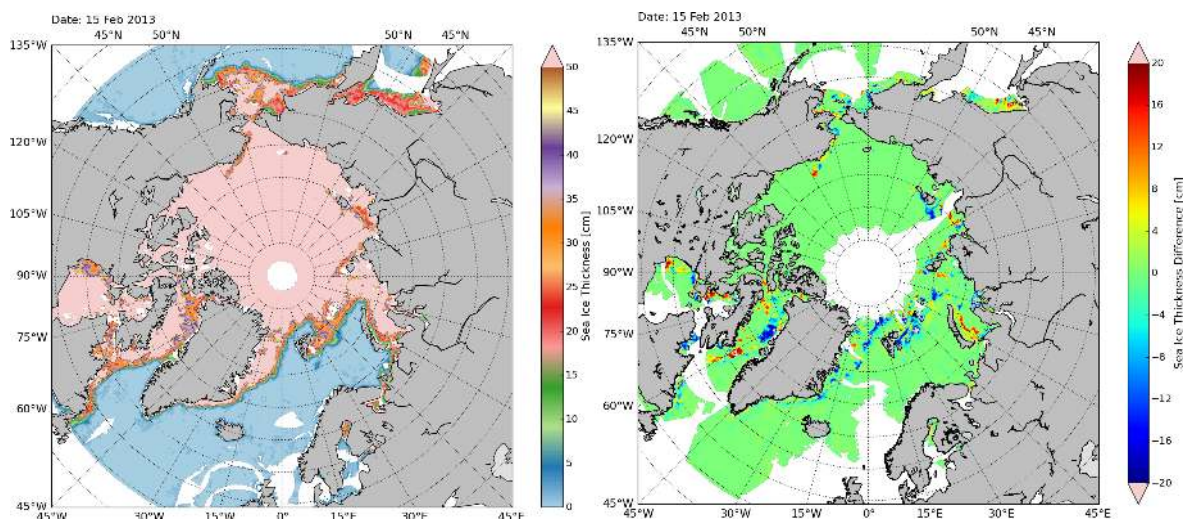


**Figure VI.25.:** Sea ice thickness computed using all available overpasses (left) and sea ice thickness difference between ascending and descending overpasses (right) for 15 Feb. 2013.

over two test regions in the Laptev and Chukchi seas show in spring and autumn irregularities. During the transition from full ice cover to open water the A/D differences varying typically by 10 to 20 K with maximum values up to 30 K (autumn 2010). They can be explained by geophysical effects like temperature differences between morning and evening (ascending and descending) overflights, melt and refreeze processes changing the emissivity and sea ice drift.

During summer and winter when the test regions are completely ice covered or ice free, the A/D differences are small with average values in the order of 0.5 K (Fig. VI.18 and VI.19).

An exception period around 15 Feb. 2013 was investigated (Fig. VI.20 and VI.21). The A/D average differences are on the order of 5 K in the Laptev sea over several consecutive days. The A/D difference maps of the complete Arctic has an overall noisy appearance in the range of  $\pm 5$  K. In many cases the noisier areas are aligned linearly suggesting that they stem from the swath borders.

High A/D differences are found in the vicinity of RFI-contaminated snapshots. Such snapshots are completely excluded from the analysis, so that the locations can be recognized in the A/D difference maps from the vicinity of missing data (white regions). In these cases, values used for the A/D differences stem from DGGs near the snapshot border. The incidence angles of the used observations are not equally distributed over the allowed incidence angle range from  $40^\circ$  to  $50^\circ$ , but biased towards higher values. This leads on average to higher brightness temperatures in vertical polarization and to lower ones in horizontal polarization. This mechanism would also explain the linearly arranged noise near the swath borders in the overall impression of the map.

Also the ice edge appears with high A/D contrast on the maps. This effect is most clearly seen in monthly averages (Fig. VI.26). Also the coastlines appear in this manner, with positive differences at the south and west coasts and negative values near the north and east coasts. The average ice edge in the Greenland Sea appears with negative values, similar as an east coast. Although due to its directionality this effect appeared to be a geolocation

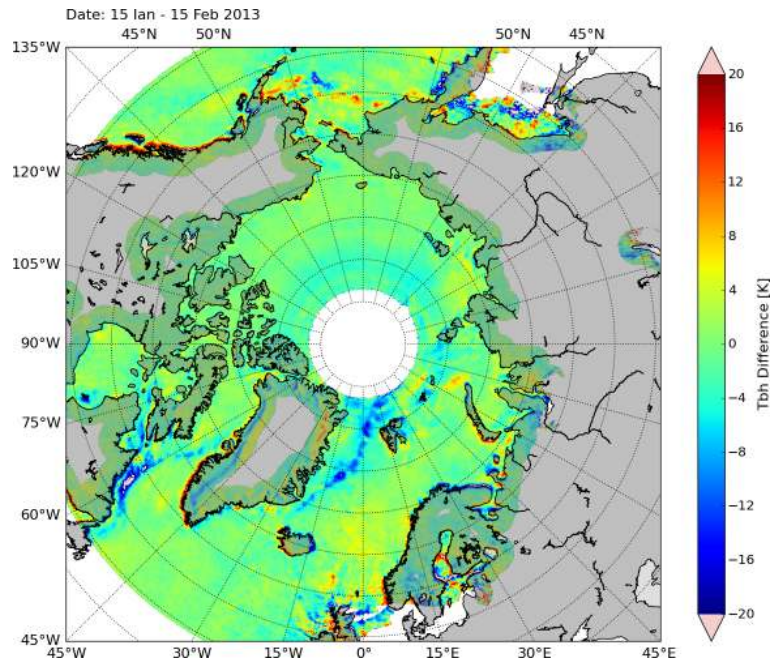


**Figure VI.26:** Tbh difference between ascending and descending overpasses for 40-50° incidence angles for 15 Jan-15 Feb 2013.

issue, this is most likely a result of the image reconstruction process because the extent was in some cases of 5 grid points which means approximately 150 km, a value far too large for geolocation error. The differences are reduced in the 620 data version.

### VI.3.3. Recommendations

The systematic biases in the A/D differences can be mitigated using a fit function for the incidence angle dependence of the brightness temperatures within each grid point. In the context of such a fit procedure, also RFI contaminated cases can be eliminated, avoiding the rejection of complete snapshots if only few pixels are affected Huntemann and Heygster (2015). Also reprocessing with the new data version is recommended due to reduction of brightness temperature difference at the ice edge.

## VI.4. Galactic noise

### VI.4.1. Problem Background

At L-band the extraterrestrial radiation sources are strong enough, and depending on the surface properties, might contaminate the upwelling radiation. This chapter investigates the influence of this extraterrestrial sources on the brightness temperature and sea ice thickness retrieval.

#### VI.4.1.1. Sources of radiation

There are three components of extraterrestrial radiation sky map:

- the cosmic microwave background which is a residue of the Big Bang, is constant in time and space with a value of approximately 2.725 K Mather et al. (1990) Fixsen (2009) with sub milliKelvin variation
- continuum radiation sources which have diverse mechanisms of production
- neutral hydrogen line emissions, which is centered at 1420.4058 MHz and spread by the Doppler effect due to the movement of the sources.

Both the continuum and neutral hydrogen emissions are mainly concentrated around the galactic center with a small amount of discrete sources outside it.

### VI.4.2. Construction of map

A main L-band sky map is constructed from two parts: 1) a continuum map which includes also the cosmic microwave background 2) a neutral hydrogen map

The continuum map data set was downloaded from the Max Plank Institute for Radio Astronomy<sup>2</sup> and is based on two surveys, one of the Northern Hemisphere done with the Stockert telescope Reich (1982) Reich and Reich (1986) and the Southern Hemisphere survey Testori et al. (2001) done using the telescope of Instituto Argentino de Radioastronomia (IAR). This surveys used a stopband filter of 2 MHz centered over the HI (neutral hydrogen) line. The map (Figure VI.27) has a resolution of  $0.25^\circ$  in the equatorial coordinates system for the J2000 epoch. The precision of this data is 0.05 K.

The hydrogen line map was downloaded from the Strasbourg astronomical Data Center<sup>3</sup> and is based of the Leiden-Argentina-Bonn (LAB) survey which is actually based on two previous surveys, the Leiden-Dwingeloo survey for the sky north of  $-30^\circ$  and the IAR survey south of the  $-25^\circ$  and then merged by Kalberla et al. (2005). The data is for radiation sources with speed relative to the earth between  $-450$  and  $+400$  km/s with a resolution of 1.3 km/s. The angular resolution of the map is  $0.5^\circ$  (in galactic coordinates) with a brightness temperature error of 0.07-0.09 K.

The continuum sources are broadband with almost constant value over the SMOS bandwidth (19 MHz), while the HI emission is considered a narrow source which must be integrated into the continuum map. This is done by first computing the velocity range using the frequency shift. Taking  $f_0 = 1420.4058$  MHz as the central frequency, the velocity relative to the earth is computed using:

<sup>2</sup><http://www3.mpifr-bonn.mpg.de/survey.html>

<sup>3</sup><http://cdsarc.u-strasbg.fr/ftp/cats/VIII/76>

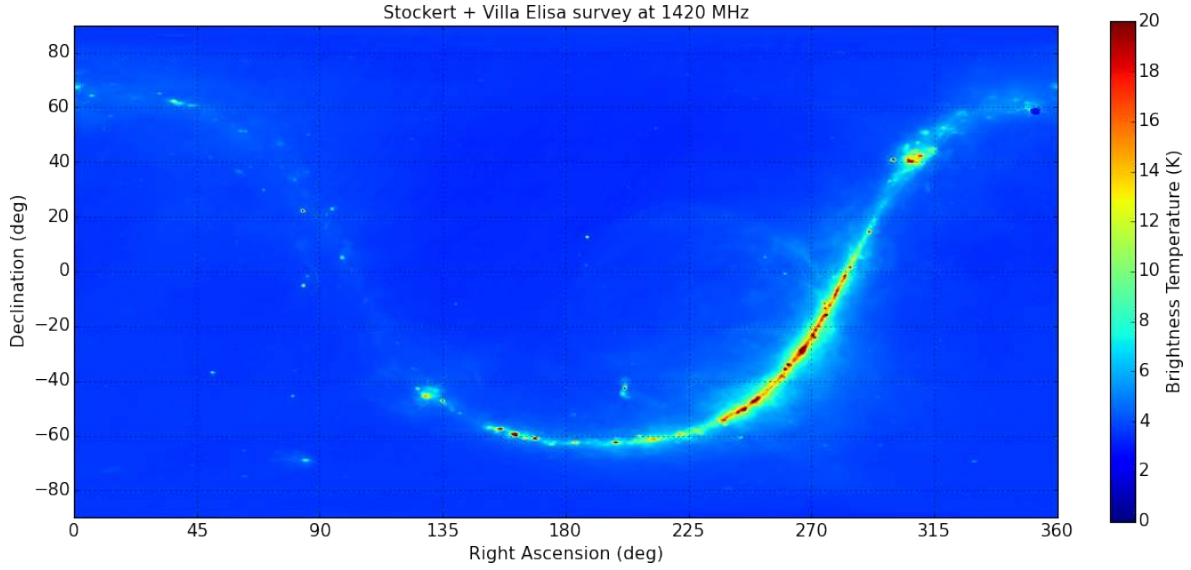


Figure VI.27.: Continuum map brightness temperatures derived from the Stockert and Villa Elisa surveys at 1420 MHz.

$$v = \frac{f_0 c}{f} - c \quad (\text{VI.5})$$

where  $c$  is the speed of light and  $f$  represents the frequency given by the Doppler shift of  $\pm 1$  MHz (2 MHz HI bandwidth -  $B_{HI}$ ) relative to  $f_0$ . This corresponds to a velocity range between -211.05 and +211.35 km/s.

For the 2 MHz bandwidth the integrated brightness temperature  $T_{HI}^*$  for the neutral hydrogen is:

$$T_{HI}^* = \frac{1}{422.4 \text{ km/s}} \int_{-221.05 \text{ km/s}}^{221.35 \text{ km/s}} T_{HI}(\nu) d\nu \quad (\text{VI.6})$$

Then we consider how this signal is seen by SMOS over the complete bandwidth. The integrated neutral hydrogen brightness temperature over the SMOS bandwidth ( $\tilde{T}_{HI}$ ) is:

$$\tilde{T}_{HI} = T_{HI}^* \cdot \frac{B_{HI}}{B_{SMOS}} \quad (\text{VI.7})$$

Now the HI map needs to be transformed from the galactic coordinates system (Figure VI.28) to the equatorial coordinates for the J2000 epoch. This is done by transforming the coordinates of an equatorial map with the same  $0.5^\circ$  resolution to galactic coordinates and then picking the nearest neighbour point from the HI map:

$$b = \sin^{-1}(\sin \delta_G \cdot \sin \delta + \cos \delta_G \cdot \cos \delta \cdot \cos(\alpha - \alpha_G)),$$

$$l = l_0 - \tan^{-1}\left(\frac{\cos \delta \cdot \sin(\alpha - \alpha_G)}{\cos \delta_G \cdot \sin \delta - \sin \delta_G \cdot \cos \delta \cdot \cos(\alpha - \alpha_G)}\right) \quad (\text{VI.8})$$

where  $l_0 = 122.9^\circ$  is the galactic longitude of the ascending node of the galactic plane,  $\alpha_G = 192.85^\circ$  and  $\delta_G = +27.13^\circ$  are the galactic pole equatorial coordinates,  $\alpha$  and  $\delta$  are the equatorial coordinates that need to be transformed, while  $b$  and  $l$  are the resulting galactic coordinates.

The final step is to resample the HI map to a resolution of  $0.25^\circ$  so it can be merged with the continuum map.

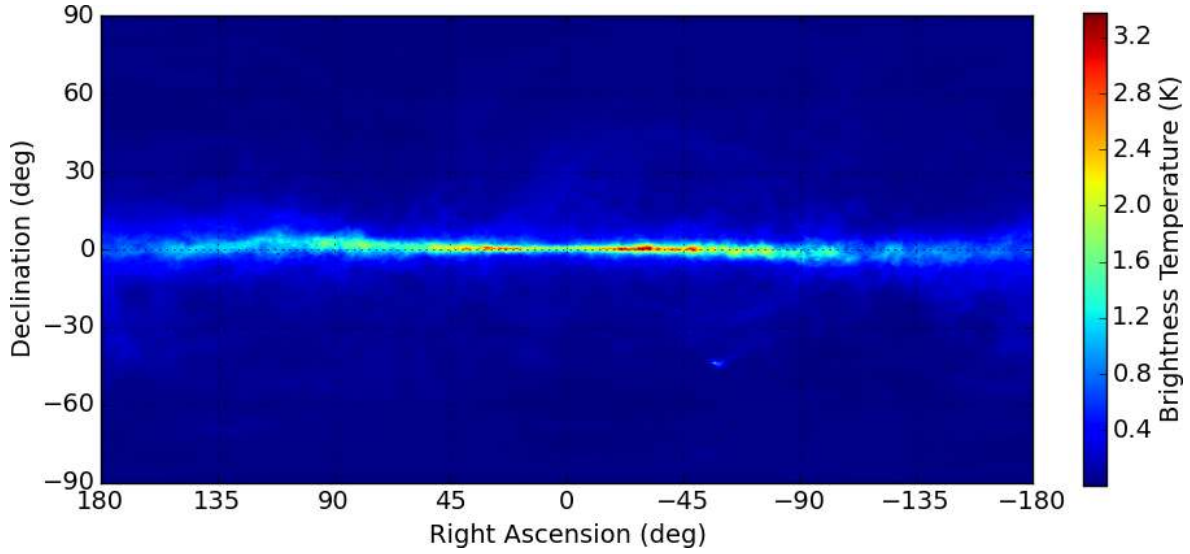


Figure VI.28.: HI map brightness temperatures in galactic coordinates derived from the LAB surveys.

It has to be noted that some strong localized sources are not taken into account by the Reich and Testori continuum survey. As shown in Reul et al. (2008) most of these sources, when compared with the continuum and HI map show brightness temperatures equal or lower in value due to their location in high emission areas on the galactic plane. The only undervalued differences appear in areas close to Cygnus A and Cassiopeia A.

Cassiopeia A is considered for inclusion in the sky map although it is problematic due to its large and variable flux density. It's location is  $(\alpha, \delta) = (350.86^\circ, 58.81^\circ)$  for the J2000 epoch. As in Dinnat et al. we took a flux density  $S_C$  of 1600 Jy (1 Jansky is  $10^{-26} \text{W/m}^2/\text{Hz}$ ) at frequency 1414 MHz for the period 2010-2013. The brightness temperature was derived using the assumption that it is constant over one pixel:

$$T_{CasA} = \frac{\lambda^2 S_C}{2k \Omega_p} \quad (\text{VI.9})$$

where  $\lambda$  is the wavelength at which the flux density was considered,  $k$  is Boltzmann's constant,  $S_C$  is the flux density and  $\Omega_p$  is the solid angle for a pixel of  $0.25^\circ \times 0.25^\circ$  at declination  $\delta$ . This results in a brightness temperature of 2645.9 K that was added to the pixel in the continuum map, while the surrounding pixel were filled just with CMB (2.725 K) values.

The final map (Figure VI.29) is composed by summing up all the contributions:

$$T_{sky} = T_{Cont} + T_{CasA}^* + \tilde{T}_{HI} \quad (\text{VI.10})$$

where  $T_{CMB}$  being already included in the continuum map.

The final step involves in transforming the map into one which already has taken into account the effect of the radiometer antenna. Thus, once the sky location of the radiation is known we can extract directly the brightness temperature. This means integrating over the antenna beam as done in Le Vine and Abraham (2004).

We are assuming an axially symmetric power pattern for the antenna with a Gaussian shape

$$P_n(\theta, \varphi) = \exp[-\beta(\theta/\theta_b)^2] \quad (\text{VI.11})$$

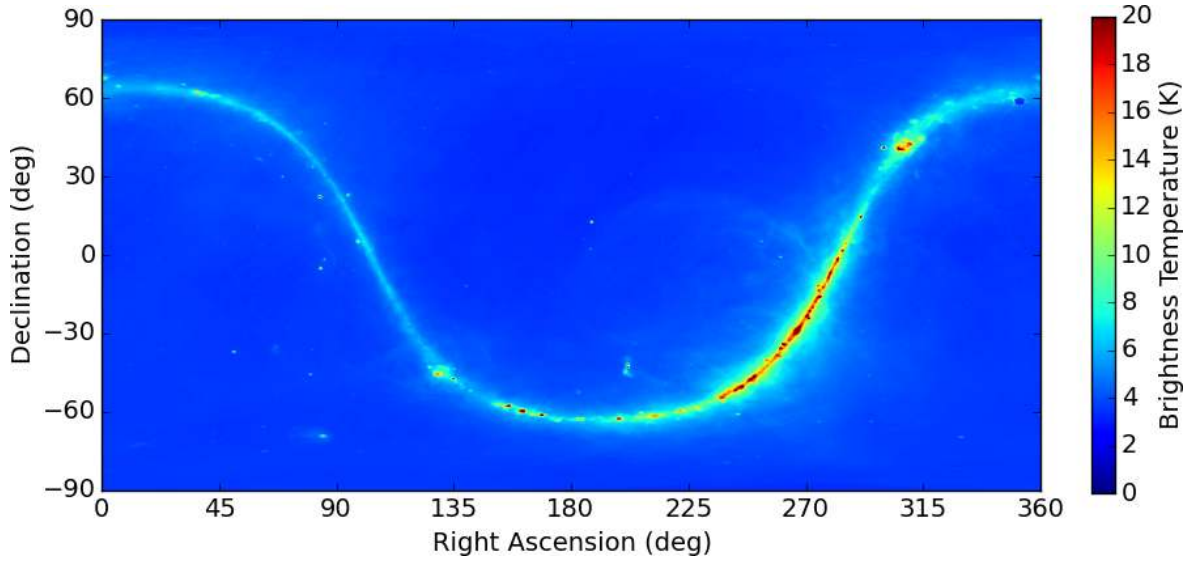


Figure VI.29.: Brightness temperature map in equatorial coordinates which includes all three radiation sources at L-band.

where  $\theta, \varphi$  are the celestial coordinates in right of ascension and declination,  $\beta = \ln(2)$ , and  $\theta_b$  is the full width at half-maximum (FWHM).

This power pattern is then convolved over the whole sky map using a FWHM of  $\theta_b = 2.25^\circ$ .

### VI.4.3. Locating the extraterrestrial radiation source

This section is based on Le Vine and Abraham (2004). We want to compute the sky location of the radiation that is reflected from the surface and seen by a downward looking radiometer. There are three assumptions made: earth is spherical, orbit is circular, and we consider a specular reflection with the reflectivity of the surface being 0.3 (an approximation for sea ice at L-band).

To compute the sky radiation location in equatorial coordinates we need to determine the right ascension  $\alpha$  and the declination  $\delta$ :

$$\theta_s = \sin^{-1}\left(\frac{R_e + h}{R_e} \cdot \sin \theta\right) \quad (\text{VI.12})$$

where  $R_e = 6371$  km and is the earth's radius,  $h = 758$  km and it represents the altitude of the satellite, and  $\theta$  is the incidence angle. From this we derive the elevation angle  $\theta_{el} = 90^\circ - \theta_s$ . The elevation angle together with the azimuth  $\phi$  and latitude of surface point is used to compute the sidereal angle  $H$ :

$$H = \tan^{-1}\left(\frac{\sin \phi}{\tan(\theta_{el}) \cdot \cos(lat) + \cos \phi \cdot \sin(lat)}\right) \quad (\text{VI.13})$$

The last parameter needed is the local sidereal time Le Vine and Abraham (2004)  $\Theta_L$ :

$$\Theta_L = \Theta_{G0} + \omega_E U_T + \lambda \quad (\text{VI.14})$$

where  $\Theta_{G0}$  is sidereal time at Greenwich at midnight for that day,  $\omega_E$  is the rate of rotation of Earth,  $U_T$  is the Greenwich time, and  $\lambda$  is the longitude.

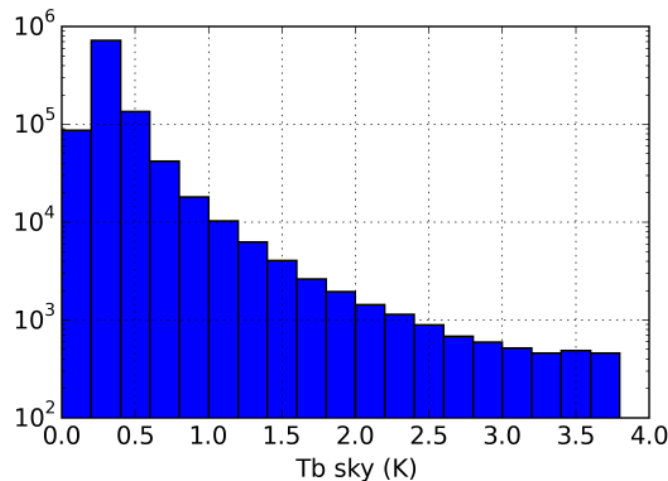
The right ascension is equal to the difference between the local sidereal time and the sidereal angle modulo 360. The declination  $\delta$  is computed using;

$$\delta = \sin^{-1}(\sin \lambda \cdot \sin \theta_{el} - \cos \lambda \cdot \cos \phi) \quad (\text{VI.15})$$

The nearest neighbour method is used to selected the coresponding sky map pixel.

#### VI.4.4. Results

For this investigation we considered just the specular reflection case. The cosmic microwave background is considered to be constant in space and time thus will be removed from the sky brightness temperatures computed for each measurement. The reflectivity of the surface is considered to be 0.3, an approximate value for the sea ice reflectivity at L-band.



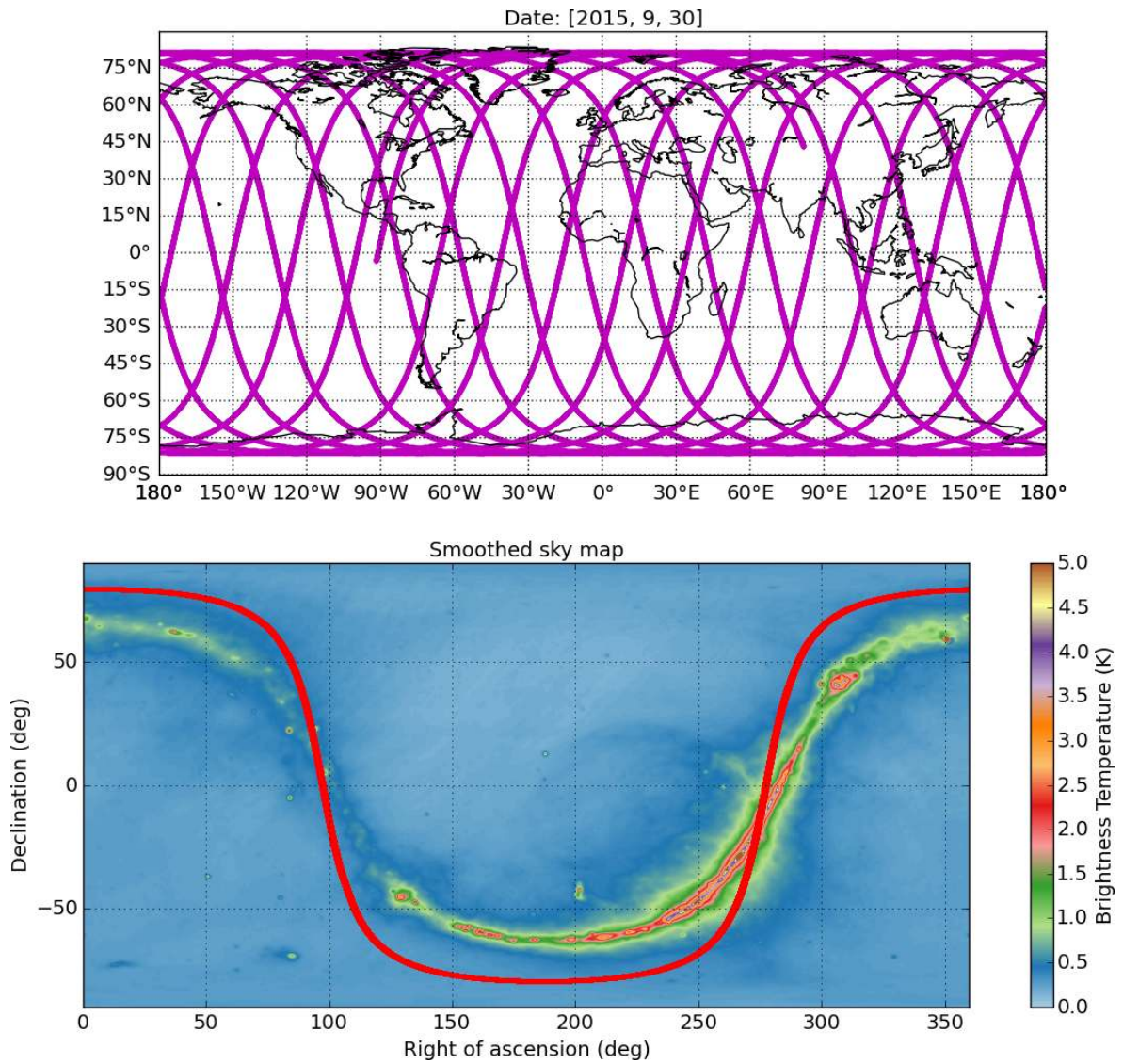
**Figure VI.30.:** Histogram of the sky brightness temperature map after removal of the cosmic microwave background and with 0.3 considered surface reflectivity

Figure VI.30 shows the histogram of the sky brightness temperature map after removal of the CMB and considering it was reflected from sea ice with a reflectivity of 0.3. More than 95% of the pixels are under 1 K.

Figure VI.31 shows an example of the SMOS ground track and the sky track computed for a fixed incidence angle of  $40^\circ$  and the azimuth in the direction of movement. The ground track was computed with the python package SPG4 which is a simple perturbation model used to calculate orbital state vectors using the two-line element set (TLE)<sup>4</sup>. This shows that for a fixed azimuth and incidence angle the latitude on earth will reflect close to the same point on the sky. This point will slowly move towards higher right of ascension together with the rotation of the Earth around the Sun. The end of September was chosen because more contamination is expected during this period in the Northern hemisphere than in the rest of the year Reul et al. (2008).

For the next step we use SMOS L1C data from 23 September 2014. We consider incidence angles between  $0^\circ$  and  $40^\circ$  and computed the sky point specularly reflected for each ground pixel and snapshot. The intensity was computed using consecutive XX and YY snapshots with a smaller time difference than 2.5 seconds. The sky brightness was recomputed for each intensity calculated as the mean between the two values. To be noted that at small

<sup>4</sup>TLE values for SMOS extracted from <http://celestrak.com> on 30 September 2015



**Figure VI.31.:** SMOS simulated ground track (upper) using SGP4 for 30 September 2015; (lower) Sky track computed for a fixed incidence angle of  $40^\circ$  and azimuth in the direction of movement

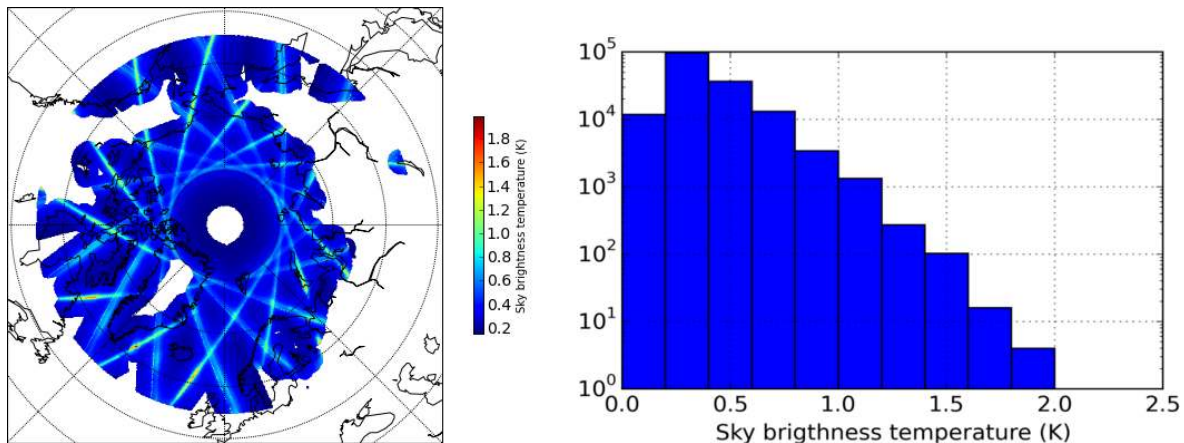


**Figure VI.32.:** Mean sky brightness temperature (left) computed for each pixel for 23 September 2014 for incidence angles between  $0^\circ$  and  $40^\circ$ , with the CMB removed and a surface reflectivity of 0.3; (right) Histogram of the mean sky brightness temperature map (left)

incidence angles the change in azimuth for a ground point is big enough to see completely different areas of the sky. For pixels that are positioned near the ground track line and at small incidence angles, the two consecutive snapshots used to compute the intensity can point to both areas with small brightness temperature and to the galactic center with high brightness temperature.

The final step involved making the daily mean sky brightness temperature for each grid point. This is seen in Figure VI.32. Almost 99% of all grid points have an average sky brightness temperature smaller than 1 K. Also for these low incidence angles all the grid points north of  $80^\circ$  are almost unaffected.

Individual swaths can contribute higher sky brightness temperatures than the maximum 2 K seen here. The smaller values come from taking the daily mean since the high values come just from a thin strip closer to the center of the swath while over one day the same point will be covered also by the sides decreasing the overall value.

For selected pixels both over sea ice and water, using a threshold of 1 K for the sky brightness temperature, the average intensity for this data per pixel is higher than the average for data points below the threshold. One example is seen in Figure VI.33 where the difference between the two means is more than 2 K. Intensity can vary with incidence angle thus a better approach should consider this variation.

#### VI.4.5. Conclusions

The influence of galactic noise has been investigated using SMOS L1C data and a generated L-band sky map which includes all three main sources of radiation at this wavelength. Due to the nature of the orbit (polar and sun-synchronous) the peak in possible contamination for the interested latitudes will be seasonally. High latitudes will mainly see the reflected sky brightness temperature from high declinations especially for low incidence angles. Because sea ice has higher emissivity than the ocean, the reflectivity must be lower thus the impact of galactic noise should be much smaller. We considered specular reflection for our case which should give the highest sky brightness temperature values for measurements that see the galactic center but much lower for the ones which are outside. In the case of non specular reflection the galactic map should be smoother with lower peaks at the galactic center a bigger spread of higher values around it. Because the Cosmic Microwave Background is

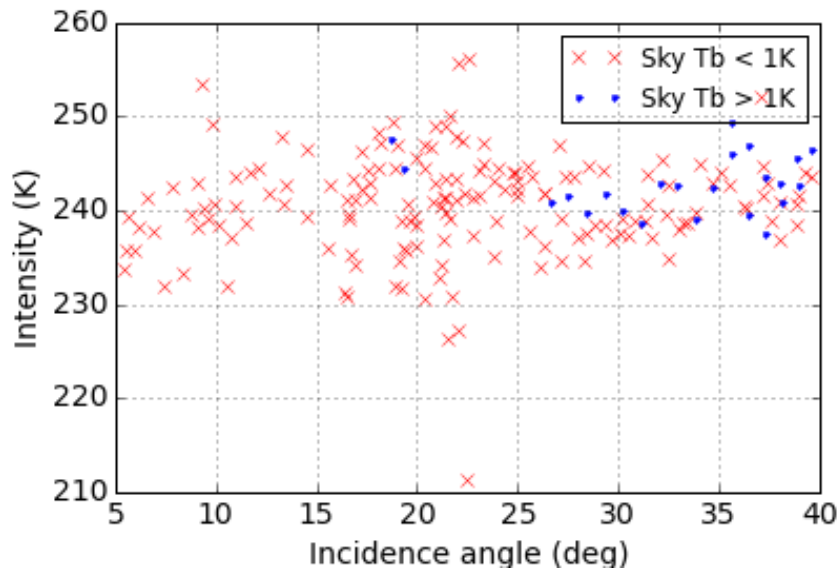


**Figure VI.33.:** Intensity dependence of incidence angle for a grid point located over sea ice at 79°N and 154°W, with red we marked the data points which contain sky brightness temperature below a threshold of 1 K, blue marks data points with sky brightness temperature over the threshold

constant in both space and time it has been removed from the final computations. From both this and the low reflectivity we see in Figure VI.30 that the sky map brightness temperatures are all below 4 K. The day 23 September 2014 which was selected because it should have a high amount of contamination in the northern hemisphere, shows that a daily mean sky brightness temperature computed using SMOS L1C data results in most grid points having less than 2 K in sky brightness temperature. Checking individual pixels both over water and sea ice showed that in many cases the average intensity at low incidence angles is higher for the data points that should be contaminated by galactic noise which passes a 1 K threshold. A better approach is to consider the incidence angle dependence and also considering a better value for the reflectivity of each pixel depending on the surface.

## VI.5. Sun glint

### VI.5.1. Problem background

The Sun is a strong radiation source at L-band. The black body temperature is approximately 100 000 K during the quiet solar cycle period, and can get as high as  $10^6$  K for the solar maximum Yueh et al. (2001). The last quiet period was in 2008-2009, while the maximum was reached in early 2014. A solar cycle lasts for approximately 11 years.

The Sun affects the measurements in both direct and indirect ways. The direct sun should appear in 96% of the images recorded by SMOS in the areas that see the sky Reul et al. (2007). The reflected sun should not enter the useful part of the Field of View (FOV) for smooth earth surface, but due to wind roughening the sea surface. For the investigation of how the sea ice thickness retrieval is affected by the sun glint over sea ice we will use the sun glint flags from the L1C dataset.

#### VI.5.1.1. Sun Emission

The brightness temperature emission of the sun can be split into three components Reul et al. (2007):

- a rapidly varying component, with a duration of seconds and minutes, usually generated by sun spots and flares
- a slowly varying component which includes all the slow variation of hours to decades
- the base level, considered to be the extrapolated zero activity

The base component is approximately 100 000 K, while the others can sum up to 2 million K. Different areas of the solar disk can emit with different degrees of polarization. An integration over the entire disk will result in averaging out the polarization. At the central frequency of SMOS (1.4 GHz) the angular radius of the sun is approximately  $0.293^\circ$ , considerably smaller than the synthesized angular resolution of SMOS of  $2.25^\circ$  thus it is seen as a point source.

### VI.5.2. Analysis

The investigation of the effect of sun glint on the sea ice thickness retrieval is being done by using the L1C dataset. The swath files contain the following relevant flags pixel wise Barbosa (2012):

- Sun FOV - direct sun correction has been applied during image reconstruction of the pixel
- Sun Glint FOV - reflected sun correction has been applied during image reconstruction of the pixel
- Sun Glint Area - pixel is located in a zone where sun reflection has been detected
- Sun Tails - pixel is located in the hexagonal alias directions centered on a sun alias
- Sun Point - pixel located in zone where sun alias was reconstructed

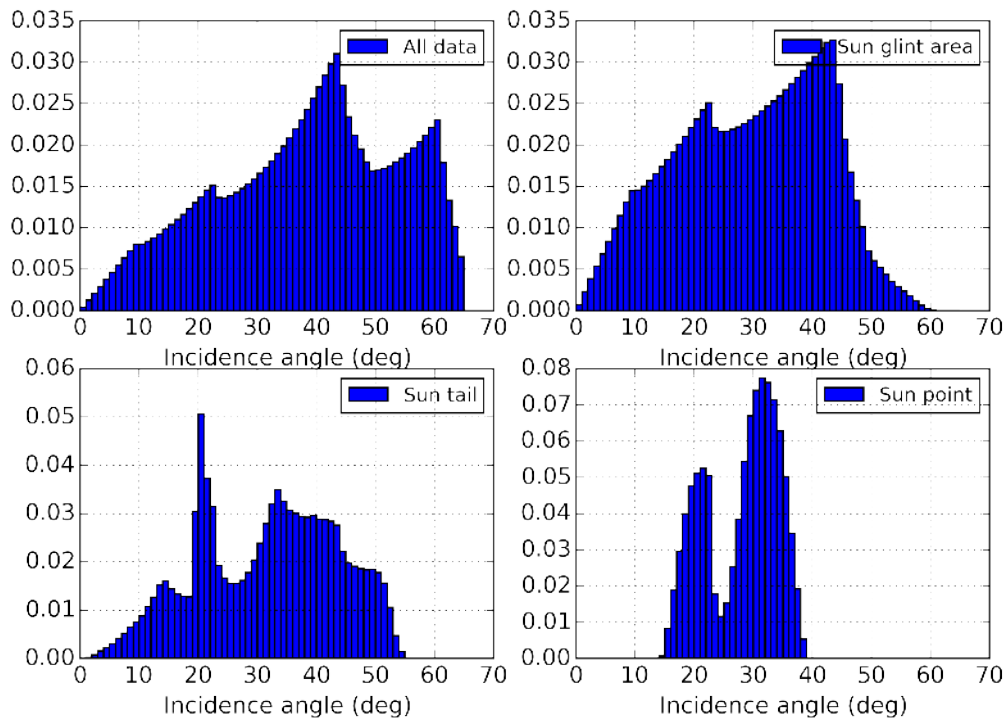


**Figure VI.34.:** Normalized histograms of data points in 1° bins with: (top left) all data points available, (top right) only sun tail flagged data, (bottom left) only sun glint area flagged, (bottom right) only sun point flagged data

The Sun Glint FOV corrections and the Sun Glint Area affected pixel identification are based on the bi-static scattering coefficients defined for the sea at a fixed wind speed of 7 m/s. It is assumed that sea ice displays less scattering than a roughened ocean.

According to Reul et al. (2007) the smallest distance between the specular sun glint points and the useful part of the SMOS FOV appears around the winter solstice (22 December) in the Southern Hemisphere. For the ocean, during this day at a solar maximum the potential contamination might reach 500 K, while the smallest contamination should be achieved during the spring equinox, with values smaller than 1.5 K.

### VI.5.3. Results

The 22nd of December 2014 was chosen in order to perform the analysis for a worst case scenario. For the Southern Hemisphere we restricted the investigated area to all the gridpoints at higher latitude than 55° S. The data is been filter for RFI by using an upper threshold of 300 K. The full incidence angle range of 0° to 65° is used.

The selected area includes approximately 163000 pixels. All SMOS pixels have been corrected for direct sun. There are no pixels corrected for sun reflection (Sun Glint FOV). Sun point, sun tails and sun glint area contaminated pixels represent 20%, 88.1% and 91.4%.

For this investigation the data is processed to brightness temperature intensities. This is done by making the mean between two consecutive XX and YY snapshots that differ by less than 2.5 seconds in time. The flag data is kept from the first snapshot used in the computation of one mean.

Figure VI.34 shows the distribution of the computed intensities incidence angle wise. The

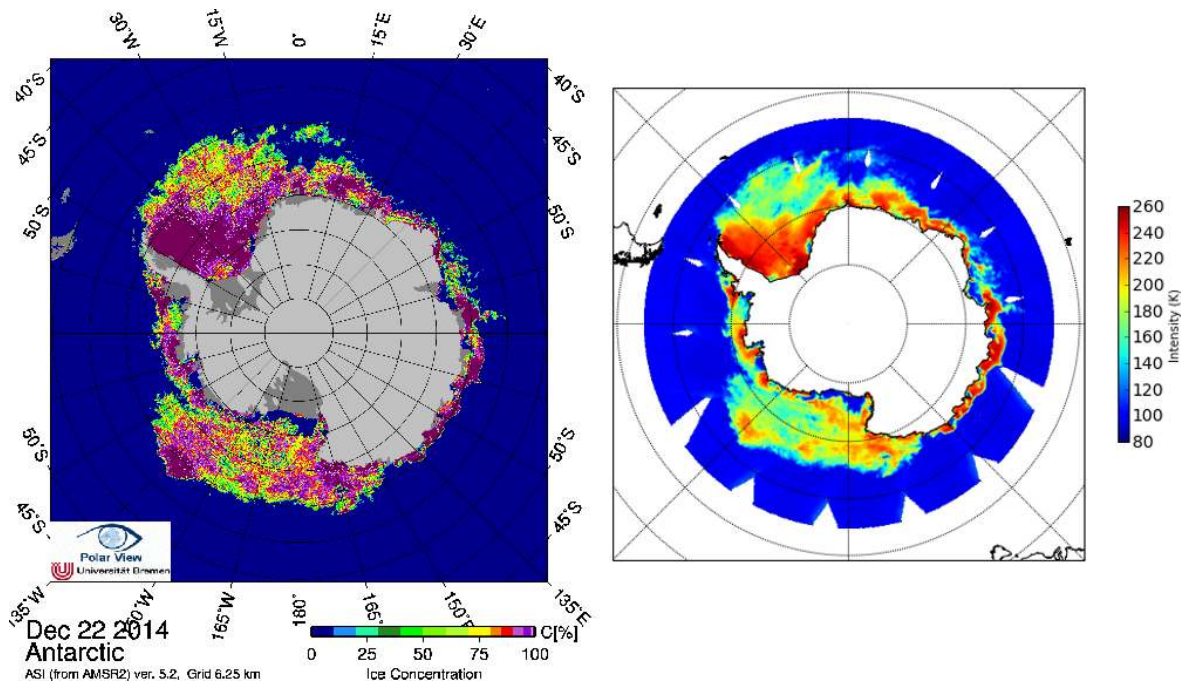


**Figure VI.35.:** Sea Ice Concentration map (left) for 2014.12.22 generated using the ASI algorithm from AMSR2 data; Mean daily brightness temperature intensity (right) for 2014.12.22 at incidence angle range 0° to 40°

first (top left) histogram shows the all the data points available, most data is found between 20° and 60°. The other three histograms show the data that contain the specific flags in question. There are no affected data points for incidence angles higher than 60° while the sun point is also bounded at the lower end, with no occurrences below 14°. The Sun Glint Area flag occurs for most pixels and incidence angles thus it has the same pattern as the all data points histogram, with the only difference being after 50° where the number of affected data is reduced to zero before 60°.

The total percentage of intensity data compromised is as follows:

- 27.8% sun glint area
- 4.5% sun tail
- 1% sun point

The last step involves selecting the data just for incidence angles under 40° and making the daily mean for each grid point. The result is shown in Figure VI.35 (right). The intensity map is in pretty good agreement with the Sea Ice Concentration map (left) generated by the ASI algorithm from Uni-Bremen for the same day.

Figure VI.36 shows how much of the data of each pixel is flagged with one of the three flags investigated. The sun glint area flag affects a large amount of pixels and for certain areas it appears in all snapshots for the incidence angle range investigated. The other two flags appear just in narrow strips along the swaths with a maximum contamination of approximately 40% of the values which contribute to each pixel.

Figure VI.37 shows the histograms of the difference in intensity for each pixel between the mean value of the intensity and the mean value with the respective flagged data removed. The Sun Point and Sun Tail flagged data affecting a smaller number of pixels and a small amount of the data per pixel have a minimal impact on the mean value. The Sun Glint Area

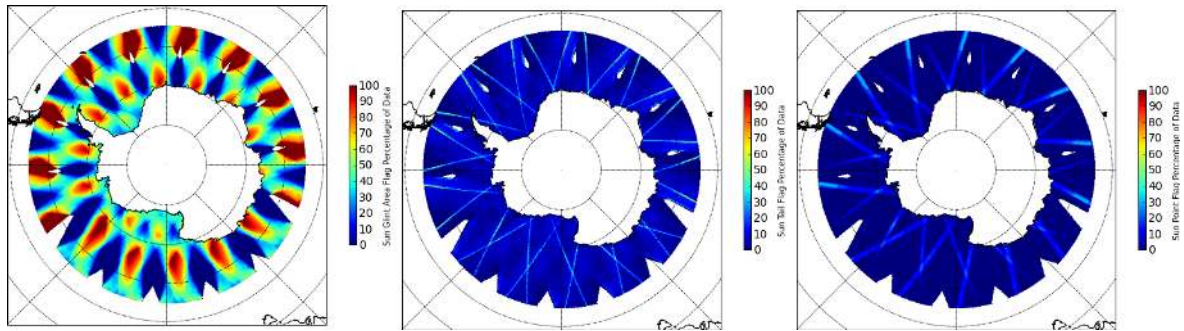


Figure VI.36.: Maps representing the percentage of data of each pixel flagged with: (left) sun glint area, (center) sun tail, (right) sun point

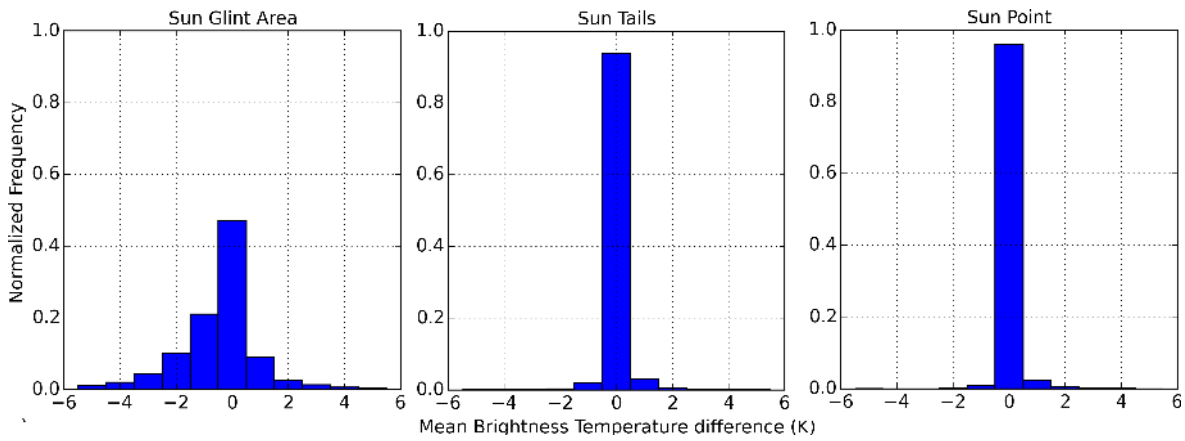


Figure VI.37.: Histograms representing the difference between the intensity computed for each pixel with all the data and with sun glint area (left), sun tail (center) and sun point (right) flagged data removed

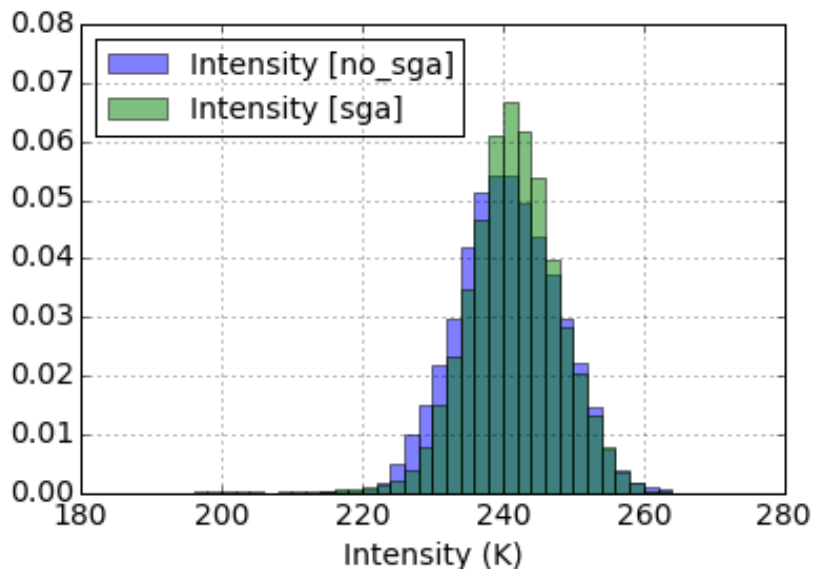


Figure VI.38.: Histogram of the intensity of a selected area east of the Antarctic Peninsula centered on 70°S and 54°W with a radius of 150 km, with (blue) only non Sun Glint Area flagged data and (green) only Sun Glint Area flagged data.

pixel due to its large spread and high percentage of affected data per pixel has a more visible impact.

The biggest differences appear at the borders of the 100% affect areas with mainly negative values as seen also in the histogram. Therefore the change in mean intensity appears more due to change in the mean incidence angle than a direct effect of the sun glint. We looked at the eastern side of the Antarctic Peninsula, an area centered on 70°S and 54°W with a radius of 150 km, completely covered by sea ice. Here we see that the difference between the peaks of the data flagged with Sun Glint Area and the data without this flag (Figure VI.38) is around 2 K, with the flagged data having the higher values.

#### **VI.5.4. Conclusion**

The pixels with a high percentage of flagged data points the difference in the mean intensity can be explained by the change in the mean incidence angle after the removal of the affected data due to the dependence of the intensity on the incidence angle. This is seen also when checking individual pixels. For SIT algorithms that use the SMOS L1C data for retrieval we recommend a detailed study of the sun glint area flag because the average influence can be up to 2 K as shown for the selected day of the year, region and solar cycle phase(Fig. VI.37 and VI.38). For this investigation we have not seen any clear bias between flagged data and unflagged data except for the sun glint area flag.



## VII SCIENTIFIC ROADMAP

The present SMOS+ Sea Ice study has clearly demonstrated the positive impact and benefit of the SMOS sea ice thickness in ocean-ice forecast system as well as the added-value of a synergy of CryoSat2 and SMOS data, but also revealed major uncertainties and knowledge gaps, namely the thickness of snow on sea ice, and the lack of in-situ vertical profiles. The insufficient knowledge about the snow caused the largest uncertainties for the validation with airborne measurements. The lack of in-situ sea ice measurements, in particular the vertical salinity profiles, together with the corresponding brightness temperatures prevents the validation of parameterizations which are necessary to further improve the retrieval models. Further there is still large potential to improve the multi-sensor synergy, and to advance the application of remote sensing data in forecast models.

- Snow thickness:

Snow has a large influence on the sea ice growth and decay. The presence of snow complicates the remote sensing of sea ice thickness with the freeboard-method and has also a substantial impact on the microwave emissivity. The snow thickness is difficult to retrieve from remote sensing measurements. Airborne radars are the most promising tools to obtain large scale snow information. However, there are considerable differences between the various snow thickness retrieval algorithms and there is currently no agreement about the best selection. In addition to the uncertainty about the best retrieval approach there was a technical problem with the snow radar used during the dedicated SMOSIce 2014 airborne field study. Thus, there are currently no reliable airborne snow thickness validation data available together with L-band brightness temperatures. New field campaigns with an improved snow radar and microwave radiometers are required to reduce this major uncertainty.

- Vertical in-situ profiles :

The large penetration depth of electromagnetic waves at 1.4 GHz provides the sensitivity to sea ice physical parameters like the ice thickness. The sea ice media can be described by a macroscopic electromagnetic permittivity mainly depending on the relative brine volume which itself depends on ice temperature and bulk salinity. The overall emission further depends on the snow thickness, the vertical ice and snow density, temperature and salinity profiles. A strong limitation for the development and improvement of sea ice radiative transfer and retrieval models stems from the lack of coincident measurements of the 1.4 GHz microwave emission and in-situ sea ice profiles. In particular the sea ice salinity is difficult to measure with autonomous sensors and the salinity evolution of first year ice is poorly understood. The availability of more co-located in-situ validation data is a prerequisite for the selection and validation of parameterizations suitable for microwave emissivity models to improve the retrieval. The Multidisciplinary drifting Observatory for the Study of Arctic Climate (MOSAIC)

with R/V Polarstern as a year-round drifting platform in the Arctic Ocean will be a unique opportunity to obtain a suitable data set.

- **Multi-sensor synergy and application:**

CryoSat-2 (CS2) and SMOS sea-ice thickness products are complementary with respect to the data coverage and the sea-ice thickness uncertainties. This complementarity allows to generate added-value synergy products from the combination of both sensors. The newly developed weekly combined sea ice thickness data set forms an important milestone and the interest of users indicate that the CS2SMOS product will have substantial impact. However, there is still room for improvement by using advanced data assimilation techniques and a better characterization of the error covariances and correlation lengths. The application of this novel observation data in ocean-ice forecast systems is only at the beginning and a thorough analysis of its impact has to be performed. The potential impact of the sea ice thickness observation used as initial condition in weather prediction systems is an untouched topic. Working towards direct assimilation of SMOS brightness temperatures in the sea ice component of a forecast model systems is a long way but promising (Richter et al., 2016). This application requires well validated sea ice emissivity models to be used as forward operators for the assimilation. Such an approach could also be feasible to solve the problem of the ice concentration effect on the SMOS sea ice thickness retrieval. In combination with higher-frequency microwave sensors like AMSR2 this method might result in enhanced resolution forecast products with a huge potential for operational applications.

## BIBLIOGRAPHY

- International Geomagnetic Reference Field - A health Warning Revised 2010, available at: <http://www.ngdc.noaa.gov/IAGA/vmod/igrfhw.html>.
- NOAA Space Weather Scales, available at: <http://www.swpc.noaa.gov/noaa-scales-explanation>.
- Alexandrov, V., Sandven, S., Wahlin, J., and Johannessen, O. M.: The relation between sea ice thickness and freeboard in the Arctic, *The Cryosphere*, 4, 373–380, doi:10.5194/tc-4-373-2010, <http://www.the-cryosphere.net/4/373/2010/>, 2010.
- Andersen, O., Knudsen, P., and Stenseng, L.: The DTU13 MSS (Mean Sea Surface) and MDT (Mean Dynamic Topography) from 20 years of satellite altimetry, 2015.
- Barbosa, J.: SMOS DPGS - SMOS Level 1 and Auxiliary Data Products Specifications, Technical Note SO-TN-IDR-GS-0005, Indra, 2012.
- Boehme, L., Meredith, M. P., Thorpe, S. E., Biuw, M., and Fedak, M.: Antarctic Circumpolar Current frontal system in the South Atlantic: Monitoring using merged Argo and animal-borne sensor data, *Journal of Geophysical Research: Oceans*, 113, doi:10.1029/2007JC004647, <http://dx.doi.org/10.1029/2007JC004647>, c09012, 2008.
- Böhme, L. and Send, U.: Objective analyses of hydrographic data for referencing profiling float salinities in highly variable environments, *Deep Sea Research Part II: Topical Studies in Oceanography*, 52, 651–664, 2005.
- Brodzik, M. J., Billingsley, B., Haran, T., Raup, B., and Savoie, M. H.: EASE-Grid 2.0: Incremental but Significant Improvements for Earth-Gridded Data Sets, *ISPRS International Journal of Geo-Information*, 1, 32–45, doi:10.3390/ijgi1010032, <http://www.mdpi.com/2220-9964/1/1/32>, 2012.
- Cardinali, C., Pezzulli, S., and Andersson, E.: Influence-matrix diagnostic of a data assimilation system, *Quarterly Journal of the Royal Meteorological Society*, 130, 2767–2786, 2004.
- Cox, G. and Weeks, W.: Equations for determining the gas and brine volumes in sea-ice samples, *Journal of Glaciology*, 29, 306–316, 1983.
- Crapolicchio, R.: VTEC usage for the SMOS Level 1 Operational Processor (L1-OP), Technical Note XSMS-GSEG-EOPG-TN-06-0019, ESA/ESRIN, 2008.
- Dee, D. P., Uppala, S. M., Simmons, A. J., Berrisford, P., Poli, P., Kobayashi, S., Andrae, U., Balmaseda, M. A., Balsamo, G., Bauer, P., Bechtold, P., Beljaars, A. C. M., van de Berg, L., Bidlot, J., Bormann, N., Delsol, C., Dragani, R., Fuentes, M., Geer, A. J., Haimberger,

- L., Healy, S. B., Hersbach, H., Hólm, E. V., Isaksen, L., Kållberg, P., Köhler, M., Matricardi, M., McNally, A. P., Monge-Sanz, B. M., Morcrette, J.-J., Park, B.-K., Peubey, C., de Rosnay, P., Tavolato, C., Thépaut, J.-N., and Vitart, F.: The ERA-Interim reanalysis: configuration and performance of the data assimilation system, *Quarterly Journal of the Royal Meteorological Society*, 137, 553–597, doi:10.1002/qj.828, 2011.
- Dinnat, E. P., Le Vine, D. M., Abraham, S., and Floury, N.: Map of Sky background brightness temperature at L-Band, available at: <http://oceancolor.gsfc.nasa.gov/AQUARIUS/DinnatEtAl2010/>.
- Dobrynin, M. and Pohlmann, T.: Anomalous hydrographic conditions in the western Barents Sea observed in March 2014, *Continental Shelf Research*, 111, Part A, 69 – 82, doi:<http://dx.doi.org/10.1016/j.csr.2015.10.020>, <http://www.sciencedirect.com/science/article/pii/S0278434315300959>, 2015.
- Eastwood, S.: OSI SAF Sea Ice Product Manual, v3.8 edn., <http://osisaf.met.no>, 2012.
- Finlay, C. C., Maus, S., Beggan, C. D., Bondar, T. N., Chambodut, A., Chernova, T. A., Chulliat, A., Golovkov, V. P., Hamilton, B., Hamoudi, M., Holme, R., Hulot, G., Kuang, W., Langlais, B., Lesur, V., Lowes, F. J., Luehr, H., Macmillan, S., Manda, M., McLean, S., Manoj, C., Menvielle, M., Michaelis, I., Olsen, N., Rauberg, J., Rother, M., Sabaka, T. J., Tangborn, A., Toffner-Clausen, L., Thebault, E., Thomson, A. W. P., Wardinski, I., Wei, Z., and Zvereva, T. I.: International Geomagnetic Reference Field: the eleventh generation, *Geophysical Journal International*, 183, 1216–1230, 2010.
- Fixsen, D.: The temperature of the cosmic microwave background, *The Astrophysical Journal*, 7077, 916–920, 2009.
- Floury, N.: Estimation of Faraday Rotation from Auxiliary Data, Technical Note TN-v2r4, ESA/ESTEC, 2007.
- Frey, R. A., Ackerman, S. A., Liu, Y., Strabala, K. I., Zhang, H., Key, J. R., and Wang, X.: Cloud detection with MODIS. Part I: Improvements in the MODIS cloud mask for collection 5, *Journal of Atmospheric and Oceanic Technology*, 25, 1057–1072, 2008.
- Griewank, P. J. and Notz, D.: A 1-D model study of Arctic sea-ice salinity, *The Cryosphere Discussions*, 8, 1723–1793, 2014.
- Haas, C.: Evaluation of ship-based electromagnetic-inductive thickness measurements of summer sea-ice in the Bellingshausen and Amundsen Seas, Antarctica, *Cold Regions Science and Technology*, 27, 1 – 16, doi:[http://dx.doi.org/10.1016/S0165-232X\(97\)00019-0](http://dx.doi.org/10.1016/S0165-232X(97)00019-0), <http://www.sciencedirect.com/science/article/pii/S0165232X97000190>, 1998.
- Haas, C., Lobach, J., Hendricks, S., Rabenstein, L., and Pfaffling, A.: Helicopter-borne measurements of sea ice thickness, using a small and lightweight, digital EM system, *Journal of Applied Geophysics*, 67, 234 – 241, doi:<http://dx.doi.org/10.1016/j.jappgeo.2008.05.005>, <http://www.sciencedirect.com/science/article/pii/S0926985108000682>, *airborne Geophysics*, 2009.

- Hall, D., Key, J., Casey, K., Riggs, G., and Cavalieri, D.: Sea ice surface temperature product from MODIS, *IEEE TRANSACTIONS ON GEOSCIENCE AND REMOTE SENSING*, 42, 1076–1087, doi:{10.1109/TGRS.2004.825587}, 2004.
- Helm, V., Hendricks, S., Göbell, S., Rack, W., Haas, C., Nixdorf, U., and Boebel, T.: CryoVEx 2004 and 2005 (BoB) data acquisition and final report, Alfred Wegener Institute, Bremerhaven, Germany., 2006.
- Helm, V., Humbert, A., and Miller, H.: Elevation and elevation change of Greenland and Antarctica derived from CryoSat-2, *The Cryosphere*, 8, 1539–1559, 2014.
- Hendricks, S.: Validierung von altimetrischen Meereisdickenmessungen mit einem helikopter-basierten elektronischen Induktionsverfahren, Ph.D. thesis, Universität Bremen, 2009.
- Hendricks, S., Steinhage, D., Helm, V., Birnbaum, G., Skou, N., Kristensen, S. S., Søbjaerg, S. S., Gerland, S., Spreen, G., Bratrein, M., King, J., and Kaleschke, L.: SMOSice 2014: Data Acquisition Report, <https://earth.esa.int/web/guest/campaigns>, Project: Technical Support for the 2014 SMOSice Campaign in SE Svalbard ESA Contract Number: 4000110477/14/NL/FF/lf Technical Report No. 1, 2014, 2014.
- Hendricks, S., Ricker, R., and Helm, V.: User Guide - AWI CryoSat-2 Sea Ice Thickness Data Product (v1.2), 2016.
- Heygster, G., Hendricks, S., Kaleschke, L., Maass, N., Mills, P., Stammer, D., Tonboe, R., and Haas, C.: L-Band Radiometry for Sea-Ice Applications. Final Report for ESA ESTEC Contract 21130, 2009.
- Huntemann, M. and Heygster, G.: A new method to filter out radio frequency interference (RFI) from SMOS Level 1C data for sea ice applications, in: *Towards an Interdisciplinary Approach in Earth System Science. Advances of a Helmholtz Graduate Research School*, edited by Lohmann, G., Megers, H., Unnithan, V., Wolf-Gladrow, D., and Notholt, J., pp. 91–98, Springer Earth System Science, 2015.
- Huntemann, M., Heygster, G., Kaleschke, L., Krumpen, T., Mäkynen, M., and Drusch, M.: Empirical sea ice thickness retrieval during the freeze up period from SMOS high incident angle observations, *The Cryosphere*, 8, 439–451, 2014.
- Johannessen, J., Raj, R., Nilsen, J. Ø., Pripp, T., Knudsen, P., Counillon, F., Stammer, D., Bertino, L., Andersen, O. B., Serra, N., et al.: Toward improved estimation of the dynamic topography and ocean circulation in the high latitude and Arctic ocean: The importance of GOCE, *Surveys in Geophysics*, 35, 661–679, 2014.
- Johnson, M., Proshutinsky, A., Aksenov, Y., Nguyen, A. T., Lindsay, R., Haas, C., Zhang, J., Diansky, N., Kwok, R., Maslowski, W., et al.: Evaluation of Arctic sea ice thickness simulated by Arctic Ocean Model Intercomparison Project models, *Journal of Geophysical Research: Oceans*, 117, 2012.
- Kalberla, P. M. W., Burton, W. B., Hartmann, D., Arnal, E. M., Bajaja, E., Morras, R., and Poppel, W. G. L.: The Leiden/Argentine/Bonn (LAB) Survey of Galactic HI, *Astron. Astrophys.*, 440, 775–782, 2005.

- Kaleschke, L., Maaß, N., Haas, C., Hendricks, S., Heygster, G., and Tonboe, R.: A sea-ice thickness retrieval model for 1.4 GHz radiometry and application to airborne measurements over low salinity sea-ice, *The Cryosphere*, 4, 583 – 592, 2010.
- Kaleschke, L., Tian-Kunze, X., Maaß, N., Heygster, G., Huntemann, M., Wang, H., Hendricks, S., Krumpen, T., Tonboe, R., Mäkynen, M., and Haas, C.: SMOS Sea Ice Retrieval Study (SMOSIce), ESA Support To Science Element (STSE), Final Report ESA ESTEC Contract No.: 4000101476/10/NL/CT, 380 pages, Univ. Hamburg, Institute of Oceanography, 2013.
- Kaleschke, L., Tian-Kunze, X., Maas, N., Ricker, R., Hendricks, S., and Drusch, M.: Improved retrieval of sea ice thickness from SMOS and CryoSat-2, in: *Geoscience and Remote Sensing Symposium (IGARSS)*, 2015 IEEE International, pp. 5232–5235, doi: 10.1109/IGARSS.2015.7327014, 2015.
- Kaleschke, L., Tian-Kunze, X., Maaß, N., Beitsch, A., Wernecke, A., Miernecki, M., Müller, G., Fock, B. H., Gierisch, A. M., Schlünzen, K. H., et al.: SMOS sea ice product: Operational application and validation in the Barents Sea marginal ice zone, *Remote Sensing of Environment*, 180, 264–273, 2016.
- Kaleschke, L., Maass, N., Haas, C., Heygster, S., and Tonboe, R.: A sea ice thickness retrieval model for 1.4 GHz radiometry and application to airborne measurements over low salinity sea ice, *The Cryosphere*, 4, 583–592, doi:{10.5194/tc-4-583-2010}, 2010.
- Kaleschke, L., Tian-Kunze, X., Maaß, N., Mäkynen, M., and Drusch, M.: Sea ice thickness retrieval from SMOS brightness temperatures during the Arctic freeze-up period, *Geophys. Res. Lett.*, doi:{10.1029/2012GL050916}, 2012.
- Kerr, Y., Waldteufel, P., Wigneron, J., Martinuzzi, J., Font, J., and Berger, M.: Soil moisture retrieval from space: The Soil Moisture and Ocean Salinity (SMOS) mission, *IEEE Transactions on Geoscience and Remote Sensing*, 39, 1729 – 1735, 2001.
- Krishfield, R., Toole, J., Proshutinsky, A., and Timmermans, M.-L.: Automated ice-tethered profilers for seawater observations under pack ice in all seasons, *Journal of Atmospheric and Oceanic Technology*, 25, 2091–2105, 2008.
- Kurtz, N. and Farrell, S.: Large-scale surveys of snow depth on Arctic sea ice from operation IceBridge, *Geophysical Research Letters*, 38, L20 505, 2011.
- Kwok, R. and Cunningham, G.: Contributions of growth and deformation to monthly variability in sea ice thickness north of the coasts of Greenland and the Canadian Arctic Archipelago, *Geophysical Research Letters*, 43, 8097–8105, 2016.
- Kwok, R., Cunningham, G. F., Wensnahan, M., Rigor, I., Zwally, H. J., and Yi, D.: Thinning and volume loss of the Arctic Ocean sea ice cover: 2003-2008, *JOURNAL OF GEOPHYSICAL RESEARCH-OCEANS*, 114, doi:{10.1029/2009JC005312}, 2009.
- Laxon, S., Peacock, N., and Smith, D.: High interannual variability of sea ice thickness in the Arctic region, *Nature*, 425, 947 – 950, 2003.
- Laxon, S. W., Giles, K. A., Ridout, A. L., Wingham, D. J., Willatt, R., Cullen, R., Kwok, R., Schweiger, A., Zhang, J., Haas, C., Hendricks, S., Krishfield, R., Kurtz, N., Farrell, S.,

- and Davidson, M.: CryoSat-2 estimates of Arctic sea ice thickness and volume, *Geophysical Research Letters*, 40, 732–737, doi:10.1002/grl.50193, <http://dx.doi.org/10.1002/grl.50193>, 2013.
- Le Vine, D. M. and Abraham, S.: Faraday rotation and passive microwave remote sensing of soil moisture from space, in: *Microwave Radiometry and Remote Sensing of the Earth's Surface and Atmosphere*, edited by Pampaloni P., P. S., pp. 89–96, VSP, 2000.
- Le Vine, D. M. and Abraham, S.: Galactic noise and passive microwave remote sensing from space at L-band, *Geoscience and Remote Sensing, IEEE Transactions on*, 42, 119–129, 2004.
- Lien, V. S., Hjøllø, S. S., Skogen, M. D., Svendsen, E., Wehde, H., Bertino, L., Counillon, F., Chevallier, M., and Garric, G.: An assessment of the added value from data assimilation on modelled Nordic Seas hydrography and ocean transports, *Ocean Modelling*, 99, 43–59, 2016.
- Lisæter, K., Evensen, G., and Laxon, S.: Assimilating synthetic CryoSat sea ice thickness in a coupled ice-ocean model, *Journal of Geophysical Research: Oceans*, 112, 2007.
- Maaß, N.: Remote sensing of sea ice thickness using SMOS data, Ph.D. thesis, Dissertation, Universität Hamburg, Max-Planck-Institute of Meteorology, Reports on Earth System Science, Report 131, 2013.
- Maaß, N., Kaleschke, L., Tian-Kunze, X., and Drusch, M.: Snow thickness retrieval over thick Arctic sea ice using SMOS satellite data, *The Cryosphere*, 7, 1971–1989, 2013.
- Maaß, N., Kaleschke, L., Tian-Kunze, X., Mäkynen, M., Drusch, M., Krumpen, T., Hendricks, S., Lensu, M., Haapala, J., and Haas, C.: Validation of SMOS sea ice thickness retrieval in the northern Baltic Sea, *Tellus A*, 67, <http://dx.doi.org/10.3402/tellusa.v67.24617>, 2015.
- Maekynen, M., Cheng, B., and Similae, M.: On the accuracy of thin-ice thickness retrieval using MODIS thermal imagery over Arctic first-year ice, *Annals of Glaciology*, 62, doi:10.3189/2013AoG62A166, 2013.
- Markus, T. and Cavalieri, D. J.: Snow Depth Distribution Over Sea Ice in the Southern Ocean from Satellite Passive Microwave Data, pp. 19–39, American Geophysical Union, doi:10.1029/AR074p0019, <http://dx.doi.org/10.1029/AR074p0019>, 2013.
- Mather, J. C., Cheng, E. S., Eplee, R. E., Isaacman, R. B., Meyer, S. S., Shafer, R. A., Weiss, R., Wright, E. L., Bennett, C. L., Boggess, N. W., Dwek, E., Gulkis, S., Hauser, M. G., Janssen, M., Kelsall, T., Lubin, P. M., Moseley, S. H., Murdock, T. L., Silverberg, R. F., Smoot, G. F., and Wilkinson, D. T.: A preliminary measurement of the cosmic microwave background spectrum by the COsmic Background Explorer (COBE) Satellite, *The Astrophysical Journal*, 354, L37–L40, 1990.
- MAYKUT, G.: ENERGY EXCHANGE OVER YOUNG SEA ICE IN CENTRAL ARCTIC, *JOURNAL OF GEOPHYSICAL RESEARCH-OCEANS AND ATMOSPHERES*, 83, 3646–3658, 1978.
- McIntosh, P. C.: Oceanographic data interpolation: Objective analysis and splines, *Journal of Geophysical Research: Oceans (1978–2012)*, 95, 13 529–13 541, 1990.

- Mecklenburg, S., Drusch, M., Kaleschke, L., Rodriguez-Fernandez, N., Reul, N., Kerr, Y., Font, J., Martin-Neira, M., Oliva, R., Daganzo-Eusebio, E., Grant, J., Sabia, R., Macelloni, G., Rautiainen, K., Fauste, J., de Rosnay, P., Munoz-Sabater, J., Verhoest, N., Lievens, H., Delwart, S., Crapolicchio, R., de la Fuente, A., and Kornberg, M.: ESA's Soil Moisture and Ocean Salinity mission: From science to operational applications, *Remote Sensing of Environment*, pp. –, doi:<http://dx.doi.org/10.1016/j.rse.2015.12.025>, <http://www.sciencedirect.com/science/article/pii/S0034425715302467>, 2016.
- Nakawo, M. and Sinha, N. K.: Growth rate and salinity profile of first-year sea ice in the high Arctic, *Journal of Glaciology*, 27, 315–330, 1981.
- Nerger, L., Hiller, W., and Schröter, J.: A comparison of error subspace Kalman filters, *Tellus A*, 57, 715–735, 2005.
- Pavlova, O., Pavlov, V., and Gerland, S.: The impact of winds and sea surface temperatures on the Barents Sea ice extent, a statistical approach, *Journal of Marine Systems*, 130, 248 – 255, doi:<http://dx.doi.org/10.1016/j.jmarsys.2013.02.011>, <http://www.sciencedirect.com/science/article/pii/S0924796313000456>, 2014.
- Pfaffing, A., Haas, C., and Reid, J. E.: Direct helicopter EM — Sea-ice thickness inversion assessed with synthetic and field data, *Geophysics*, 72, F127–F137, doi: 10.1190/1.2732551, <http://geophysics.geoscienceworld.org/content/72/4/F127.abstract>, 2007.
- Reich, P. and Reich, W.: A radio continuum survey of the northern sky at 1420 MHz - Part II, *Astron. Astrophys. Suppl. Series*, 63, 205–292, 1986.
- Reich, W.: A radio continuum survey of the northern sky at 1420 MHz â Part I, *Astron. Astrophys. Suppl. Series*, 48, 219–297, 1982.
- Relloso, F. G. and Zapata, M.: SMOS DPGS - L0 Product Specifications, Technical Note SO-TN-IDR-GS-0003, Indra, 2010.
- Reul, N., Tenerelli, J., Chapron, B., and Waldteufel, P.: Modeling sun glitter at L-band for sea surface salinity remote sensing with SMOS, *Geoscience and Remote Sensing, IEEE Transactions on*, 45, 2073–2087, 2007.
- Reul, N., Tenerelli, J., Floury, N., and Bertrand, C.: Earth-Viewing L-Band Radiometer Sensing of Sea Surface Scattered Celestial Sky Radiation - Part II: Application to SMOS, *IEEE Transactions on Geoscience and Remote Sensing*, 46, 675–688, 2008.
- Richter, F., Drusch, M., Kaleschke, L., Maaß, N., Tian-Kunze, X., and Mecklenburg, S.: Arctic sea ice signatures: L-Band brightness temperature sensitivity comparison using two radiation transfer models, *The Cryosphere Discussions*, 2016, 1–22, doi:10.5194/tc-2016-273, <https://www.the-cryosphere-discuss.net/tc-2016-273/>, 2016.
- Ricker, R., Hendricks, S., Helm, V., Skourup, H., and Davidson, M.: Sensitivity of CryoSat-2 Arctic sea-ice freeboard and thickness on radar-waveform interpretation, *The Cryosphere*, 8, 1607–1622, doi:10.5194/tc-8-1607-2014, <http://www.the-cryosphere.net/8/1607/2014/>, 2014.

- Ricker, R., Hendricks, S., Perovich, D. K., Helm, V., and Gerdes, R.: Impact of snow accumulation on CryoSat-2 range retrievals over Arctic sea ice: An observational approach with buoy data, *Geophysical Research Letters*, 42, 4447–4455, 2015.
- Ricker, R., Hendricks, S., and Beckers, J. F.: The Impact of Geophysical Corrections on Sea-Ice Freeboard Retrieved from Satellite Altimetry, *Remote Sensing*, 8, 317, 2016.
- Ricker, R., Hendricks, S., Girard-Ardhuin, F., Kaleschke, L., Lique, C., Tian-Kunze, X., Nicolaus, M., and Krumpfen, T.: Satellite-observed drop of Arctic sea ice growth in winter 2015-2016, *Geophysical Research Letters*, 44, 3236–3245, doi:10.1002/2016GL072244, <http://dx.doi.org/10.1002/2016GL072244>, 2016GL072244, 2017a.
- Ricker, R., Hendricks, S., Kaleschke, L., Tian-Kunze, X., King, J., and Haas, C.: A weekly Arctic sea-ice thickness data record from merged CryoSat-2 and SMOS satellite data, *The Cryosphere*, 11, 1607–1623, doi:10.5194/tc-11-1607-2017, <https://www.the-cryosphere.net/11/1607/2017/>, 2017b.
- Rodgers, C.: *Inverse methods for atmospheres: Theory and practice*, World Science: Hackensack, NJ, 2000.
- Rued, S.: Influence of the vertical salinity distribution on the 1.4 GHz brightness temperature of Arctic sea ice simulated using a 1-D thermo-halo-dynamic model, Master thesis, 2015.
- Sakov, P., Evensen, G., and Bertino, L.: Asynchronous data assimilation with the EnKF, *Tellus A*, 62, 24–29, 2010.
- Sakov, P., Counillon, F., Bertino, L., Lisæter, K., Oke, P., and Korabely, A.: TOPAZ4: an ocean-sea ice data assimilation system for the North Atlantic and Arctic, *Ocean Science*, 8, 633, 2012.
- Sandven, S., Johannessen, O. M., Miles, M. W., Pettersson, L. H., and Kloster, K.: Barents Sea seasonal ice zone features and processes from ERS 1 synthetic aperture radar: Seasonal Ice Zone Experiment 1992, *Journal of Geophysical Research: Oceans*, 104, 15 843–15 857, doi:10.1029/1998JC900050, <http://dx.doi.org/10.1029/1998JC900050>, 1999.
- Schweiger, A., Lindsay, R., Zhang, J., Steele, M., Stern, H., and Kwok, R.: Uncertainty in modeled Arctic sea ice volume, *Journal of Geophysical Research: Oceans*, 116, 2011.
- Smedsrud, L. H., Esau, I., Ingvaldsen, R. B., Eldevik, T., Haugan, P. M., Li, C., Lien, V. S., Olsen, A., Omar, A. M., Otterå, O. H., Risebrobakken, B., Sandø, A. B., Semenov, V. A., and Sorokina, S. A.: THE ROLE OF THE BARENTS SEA IN THE ARCTIC CLIMATE SYSTEM, *Reviews of Geophysics*, 51, 415–449, doi:10.1002/rog.20017, <http://dx.doi.org/10.1002/rog.20017>, 2013.
- Sobjaerg, S., Kristensen, S., Balling, J., and Skou, N.: The airborne EMIRAD L-band radiometer system, in: *Geoscience and Remote Sensing Symposium (IGARSS)*, 2013 IEEE International, pp. 1900–1903, doi:10.1109/IGARSS.2013.6723175, 2013.
- Strübing, K. and Schwarz, J.: Die Eisverhältnisse in der Barentssee während der IRO-2-Testfahrt mit R/V Lance 17.-27.03.2014, Abschlussbericht vorgelegt von JS Consulting, Großhansdorf, im Auftrag des AWI; Bestellnummer 12/45086354 zum Werkvertrag Vor-/Nachbereitung und Durchführung der IRO-2-Testfahrt im Rahmen des Vorhabens

- Entwicklung und Optimierung eines Ozean-Meereis Vorhersagemodells für das Nordpolarmeer, BMWi-Förderkennzeichen: 03SX328H, 2014.
- Svedhem, H.: Ionospheric Delay and Faraday Rotation at Microwave Frequencies, Report TRI/075/HS/mt, ESA/ESTEC, 1986.
- team, S. C. and 1, E. S. L. L.: SMOS L1OPv620 release note, Release note, ESA, 2015.
- Testori, J. C., Reich, P., Bava, J. A., Colomb, F. R., Hurrell, E. E., Larrarte, J. J., Reich, W., and Sanz, A. J.: A radio continuum survey of the southern sky at 1420 MHz - Observations and data reduction, *Astron. Astrophys.*, 368, 1123–1132, 2001.
- Tian-Kunze, X., Kaleschke, L., Maaß, N., Mäkynen, M., Serra, N., Drusch, M., and Krumpen, T.: SMOS-derived thin sea ice thickness: algorithm baseline, product specifications and initial verification, *The Cryosphere*, 8, 997–1018, 2014.
- Tiemann, L.: Sea ice parameters simulated with 1D-thermodynamic models compared to ice mass balance buoy observations, Master thesis, 2016.
- Tonboe, R. T., Dybkjaer, G., and Hoeyer, J.: Simulation of the snow covered sea ice surface and microwave effective temperature, *Tellus A*, 2011.
- TOOle, J. M., Krishfield, R. A., Timmermans, M.-L., and Proshutinsky, A.: The ice-tethered profiler: Argo of the Arctic, 2011.
- Ulaby, F., Moore, R., and Fung, A.: Microwave remote sensing: Active and passive. Volume 1-Microwave remote sensing fundamentals and radiometry, 1981.
- Wang, X., Key, J., Kwok, R., and Zhang, J.: Comparison of Arctic Sea Ice Thickness from Satellites, Aircraft, and PIOMAS Data, *Remote Sensing*, 8, 713, 2016.
- Warren, S., Rigor, I., Untersteiner, N., Radionov, V., Bryazgin, N., Aleksandrov, Y., and Colony, R.: Snow depth on Arctic sea ice, *Journal of Climate*, 12, 1814 – 1829, 1999.
- Wingham, D. J., Francis, C. R., Baker, S., Bouzinac, C., Brockley, D., Cullen, R., de Chateau-Thierry, P., Laxon, S. W., Mallow, U., Mavrocordatos, C., Phalippou, L., Ratier, G., Rey, L., Rostan, F., Viau, P., and Wallis, D. W.: CryoSat: A mission to determine the fluctuations in Earth's land and marine ice fields, in: *NATURAL HAZARDS AND OCEANOGRAPHIC PROCESSES FROM SATELLITE DATA*, edited by Singh, RP and Shea, MA, vol. 37 of *ADVANCES IN SPACE RESEARCH*, pp. 841–871, doi: {10.1016/j.asr.2005.07.027}, 35th COSPAR Scientific Assembly, Paris, FRANCE, JUL 18-25, 2004, 2006.
- Xie, J., Bertino, L., Counillon, F., Lisæter, K. A., and Sakov, P.: Quality assessment of the TOPAZ4 reanalysis in the Arctic over the period 1991–2013, *Ocean Science Discussions*, 2016, 1–53, doi:10.5194/os-2016-38, <http://www.ocean-sci-discuss.net/os-2016-38/>, 2016a.
- Xie, J., Counillon, F., Bertino, L., Tian-Kunze, X., and Kaleschke, L.: Benefits of assimilating thin sea ice thickness from SMOS into the TOPAZ system, *The Cryosphere*, 10, 2745–2761, 2016b.

- Yang, Q., Losa, S. N., Losch, M., Tian-Kunze, X., Nerger, L., Liu, J., Kaleschke, L., and Zhang, Z.: Assimilating SMOS sea ice thickness into a coupled ice-ocean model using a local SEIK filter, *Journal of Geophysical Research: Oceans*, 119, 6680–6692, doi:10.1002/2014JC009963, <http://dx.doi.org/10.1002/2014JC009963>, 2014.
- Yang, Q., Losch, M., Losa, S. N., Jung, T., and Nerger, L.: Taking into Account Atmospheric Uncertainty Improves Sequential Assimilation of SMOS Sea Ice Thickness Data in an Ice–Ocean Model, *Journal of Atmospheric and Oceanic Technology*, 33, 397–407, 2016.
- Yu, Y. and Rothrock, D.: Thin ice thickness from satellite thermal imagery, *JOURNAL OF GEOPHYSICAL RESEARCH-OCEANS*, 101, 25 753–25 766, 1996.
- Yueh, S. H., West, R., Wilson, W. J., Li, F. K., Njoku, E. G., and Rahmat-Samii, Y.: Error Sources and Feasibility for Microwave Remote Sensing of Ocean Surface Salinity, *IEEE Transactions on Geoscience and Remote Sensing*, 39, 1049–1060, 2001.
- Zhang, J., Rothrock, D., and Steele, M.: Recent changes in Arctic sea ice: The interplay between ice dynamics and thermodynamics, *Journal of Climate*, 13, 3099–3114, 2000.
- Zundo, M., Duesman, B., and Sole, M. P.: SMOS Ground Segment - On-ground BT Frame of Reference TN, Technical Note SO-TN-ESA-GS-5873, ESA, 2010.